

RHODES UNIVERSITY
Where leaders learn

Exploring Intensity Mapping Techniques Via Simulations

Author:

Theophilus ANSAH-NARH

Supervisors:

Prof. Oleg M. SMIRNOV

Dr. Filipe B. ABDALLA

Dr. Khan M. B. ASAD

*A thesis submitted in fulfillment of the requirements
for the degree of Doctor of Philosophy*

in the

Centre for Radio Astronomy Techniques & Technologies
Department of Physics and Electronics

February 20, 2018

Declaration of Authorship

I, Theophilus ANSAH-NARH, disclose that this thesis titled, “Exploring Intensity Mapping Techniques Via Simulations” and the studies reported in it are my own. I confirm that:

- This work was done wholly or mainly while in candidature for a research degree at this University.
- Where any part of this thesis has previously been submitted for a degree or any other qualification at this University or any other institution, this has been precisely stated.
- Where I have discussed the published work of others, this is always clearly credited.
- Where I have quoted from the work of others, the source is always given. With the exception of such quotations, this thesis is completely my own work.
- I have acknowledged all main sources of assistance.
- Where the thesis is based on work done by myself jointly with others, I have made known exactly what was done by others and what I have contributed myself.

Signed:

Date:

“The three great essentials to achieve anything worthwhile are, first, hard work; second, stick-to-itiveness; third, common sense.”

Thomas A. Edison

Abstract

Intensity mapping experiment treats CO and 21-cm radio emissions as diffuse sources and allow smaller and relatively cheaper radio antennas with short baselines to be used in such experiments. However, the technique is restricted by the precise subtraction of the foreground continuum signal from Galactic and extra-galactic radio sources. Furthermore, the signal is subjected to direction-dependent effects (DDEs), particularly, the primary beam, as it modulates the intensity as a function of the sky position. Also, due to the imperfections in the antenna feeds, a portion of the polarised foreground tends to find its way into total intensity, making it a major obstacle to detect the HI signal. In the case of upcoming aperture arrays, these will be dominated by the instrument mis-pointings and polarisation leakage. To overcome these challenges, we simulate realistic “dish-like” primary beams and then perturb these primary beams by errors in these beams. We then simulate the foregrounds with these modelled beams to correct the errors in Stokes I and also, observe the amount of $|Q + iU|$ that corrupts I . Our simulation shows that, both the CO and HI signal power can be measured at a multipole moment of $l = 100$ if we do not correct for any polarisation leakage of the beam and at a multiple moment of $l \lesssim 50$ if we correct for the beam from I , assuming the beam is not known to the extent of which we have considered in this research.

Acknowledgements

This thesis is the culmination of the efforts of many individuals to whom I owe my most sincere appreciation. First of all I would like to thank my supervisors: Prof. Oleg M. Smirnov who doubles as the SKA Chair in Radio Astronomy Techniques and Technologies (RATT), which is hosted by Rhodes University and my main supervisor, especially for the passion he brings to everything he does and for his great knowledge in Mathematics and Radio Interferometry, Dr. Filipe B. Abdalla for his expertise in Cosmology and Intensity Mapping Experiments and for the patience he had in supporting me especially during the first year of the research and also, Dr. Khan M. B. Asad for his understanding in Intensity Mapping Experiments. Sincere gratitude is also extended to Prof. Mario Santos who is a member of the supervisory committee. I would like to thank everybody who was directly involved in the realization of this project, particularly to Dr. Richard Shaw for helping me out with the foreground simulations and Dr. Jamie Leech for teaching me how to use the GRASP software. I acknowledge many individuals who even if in a less technical way, have been and are of vital importance for me throughout this research experience. My entire course mates deserve the best recognition. Sphe, Marcel, Ridhima, Liju, Kela, Alex and the others have been wonderful companions throughout the study period. I would like to thank my family, Mr. Francis D. Narh (father), Mrs. Salome Nortey (mother), Samuel Annor Narh (brother), Esther Amatsu Narh, Christiana Koryoonmaatso Narh (sisters), Patricia Opoku (wife) and Adelaide Tsako Doku (daughter) for their love and trust. Lastly, I am very grateful to the SKA and NRF for supporting this research. Without them this accomplishment would have been unachievable.

Contents

Declaration of Authorship	i
Abstract	iii
Acknowledgements	iv
Contents	v
List of Figures	viii
List of Tables	xiv
List of Abbreviations	xv
Physical Constants	xvii
List of Symbols	xviii
1 Introduction	1
1.1 The Origin of the Hydrogen 21 cm Line	1
1.2 HI Intensity Mapping	3
1.3 Significance of Intensity Mapping Techniques	5
1.4 Problem Identification	6
1.5 Research Objective	6
1.6 Delimitation	7
1.7 Rationale and Motivation	7
1.8 Thesis Outline	8
2 Radio Antennas and Aperture Synthesis Technique	10
2.1 Introduction	10
2.2 Antenna Parameters	11
2.2.1 Field Regions	12
2.2.2 Radiation Patterns	13
2.2.3 Beamwidth	14
2.2.4 Radiation Intensity	15
2.2.5 Radiation Patterns Types	15
2.2.6 Gain	15

2.3	EM Wave Polarisation	16
2.3.1	Derivation of the Stokes Polarisation Parameters	17
2.4	Antenna Arrays	20
2.4.1	Mathematical Formulation of Antenna Array	20
2.4.2	Beamforming	21
2.4.3	Types of Radio Arrays	22
2.4.3.1	Phased-Array Feeds	22
2.4.3.2	Transiting Arrays	22
2.4.3.3	Aperture Arrays	23
2.5	Power received from radio sources in the sky	25
2.6	Aperture Synthesis Technique	26
2.6.1	Construction of Radio Images	26
2.6.2	Correlator Super-synthesis Arrays	28
2.6.3	The Van Cittert-Zernike Equation	28
2.6.4	Filling the u,v Plane with Visibilities	31
3	Radio Foregrounds and Rotation Measure Synthesis	33
3.1	Introduction	33
3.2	Galactic Foreground	33
3.2.1	Diffuse Galactic Synchrotron Emission	34
3.3	Faraday Rotation Measure Synthesis	39
4	Simulations of Direction-dependent Instrumental Systematic Effects in Intensity Mapping Experiments	41
4.1	Primary Beam Modelling	41
4.2	OSKAR Beam Model	42
4.2.1	Jones and Mueller matrices	47
4.2.1.1	Derivation of Mueller Matrix	49
4.2.2	Primary Beam Perturbation	52
4.3	Simulation	56
4.3.1	Full-sky Convolution	56
4.3.2	Angular Power Spectrum	60
4.4	Results and Analysis	61
4.5	Conclusions	65
5	MeerKAT L-Band Primary Beams: Effects of HI Intensity Mapping	67
5.1	Introduction	67
5.2	Methodology	68
5.2.1	Mathematical Basis of Zernike Polynomials	68
5.2.2	Orthonormality	71
5.2.3	Numerical Computation of Zernike Coefficients	72
5.2.4	Spatial Representation	74
5.3	Results and Discussion	77

5.4 Conclusion	80
6 SKA1-mid Multiband Primary Beams: Effects of HI and CO Intensity Mapping	81
6.1 Introduction	81
6.1.1 SKA1-mid	81
6.1.2 Line Intensity Mapping	82
6.2 GRASP Beam Measurement	82
6.2.1 Model Specification	83
6.2.1.1 Reflector Antenna Models	83
6.2.1.2 Feed Models	84
6.2.1.3 Format of Input/Output Field Data	84
6.2.2 Numerical Analysis of Reflector Antennas	89
6.2.2.1 Physical Optics (PO)	89
6.2.2.2 Physical Theory of Diffraction (PTD)	90
6.3 Modelling EM Beams	90
6.3.1 Fitting 2D Zernike Polynomials on EM Beams	90
6.3.1.1 Spatial Representation	90
6.3.1.2 Spectral Representation	93
6.3.2 Model Beam Perturbation	95
6.3.3 Intrinsic Cross Polarisation (IXR)	98
6.4 MODELLING CO EMISSION	100
6.4.1 The CO Power Spectrum	100
6.5 Results and Analysis	101
6.6 Conclusion	107
7 Conclusions	108
Bibliography	109
A OSKAR BEAMPATTERN AND FOREGROUND SIMULATIONS	121
A.1 Ray Tracing Technique	121
A.2 Modelled and measured beams	122
A.3 Measured Full-sky maps	125
A.4 Error Estimation in the Power Spectrum	127

List of Figures

1.1	<i>When the electron flips its spin, the atom emits a photon with a wavelength of 21 cm</i>	2
1.2	<i>The Properties of Electromagnetic Radiation</i>	3
1.3	<i>Simulated fluctuations in the brightness temperature of 21 cm emission from galaxies. Red indicates over-density and blue under-density. The circles show how to perform IM experiment with the radio telescope in order to measure the 21 cm emission.</i>	4
1.4	<i>Structure of the thesis</i>	8
2.1	<i>The different field regions of an antenna.</i>	12
2.2	<i>The different field regions of an antenna.</i>	13
2.3	<i>(a) Antenna pattern lobes in polar coordinates. (b) Antenna pattern lobes in linear power scale.</i>	14
2.4	<i>Graphical representation of antenna radiation properties. From left: shows the Isotropic patterns, middle: presents the Omni Directional Radiation Pattern and right: Directional pattern.</i>	15
2.5	<i>Relation of instantaneous electric-field vector \mathbf{E} to polarisation ellipse</i>	16
2.6	<i>Wide gain in FoV enabled by PAFs. Right-centre: APERTIF installed at the focus of a WSRT telescope. Extreme right: PAFs installed on ASKAP (courtesy CSIRO).</i>	22
2.7	<i>Transiting Arrays:- PAPER (top-left), LWA (bottom-left), Medicina Northern Cross (top-right) and MWA (bottom-right).</i>	23
2.8	<i>Aperture Array:- LOFAR.</i>	24
2.9	<i>SKA-2 Dense Aperture Arrays precursor telescope.</i>	24
2.10	<i>(a) A distant radio astronomical source illuminates a dish antenna with parallel rays. (b) Electric field distributions of a source on the great sphere and antenna aperture on the aperture plane</i>	26
2.11	<i>The principle of super synthesis. (a) An interferometer rotates with the Earth rotation (b) Observing a radio source towards celestial North Pole. (c) Observing a radio source along the celestial equator. (d) Observing a radio source along a celestial latitude in between.</i>	27
2.12	<i>Geometry of a radio source and a simple interferometer. (a) An observed radio source with intensity distribution $I(l, m)$ using a simple two element radio interferometer. (b) Lower the elevation angle of the radio source the larger the value of w.</i>	29

2.13	<i>Locus on the u, v plane.. (a) Locus of the ellipse on u, v plane for a baseline with $Z_\lambda \neq 0$ observing a radio source at declination δ_0. (b) Different declinations for different cases.</i>	31
2.14	<i>Filling the $u\text{-}v$ plane with visibilities. (a) The KAT-7 configuration. (b) The $u\text{-}v$ plane coverage of a 4h period of observation obtained from a source at the phase centre.</i>	32
3.1	<i>A model of radio galaxy spectrum (see Murphy 2011). The individual contributions from non-thermal synchrotron, free-free, and thermal dust emission are indicated by dot-dashed, triple dot-dashed, and dashed lines, respectively.</i>	34
3.2	<i>408 MHz Full-Sky Map.</i>	36
3.3	<i>1000 MHz full-sky synchrotron maps simulated by using m-mode formalism. These synchrotron maps characterize the full-sky polarisation maps for our low resolution simulated observations and are presented here in the mollweide projection form defined by equatorial coordinates in terms of Stokes parameters I, Q, U and V.</i>	37
3.4	<i>950 MHz full-sky synchrotron maps simulated by using m-mode formalism.</i>	37
3.5	<i>450 MHz full-sky synchrotron maps simulated by using m-mode formalism.</i>	38
3.6	<i>990.5 MHz full-sky synchrotron maps simulated by using m-mode formalism.</i>	38
3.7	<i>4.6 GHz full-sky synchrotron maps simulated by using m-mode formalism.</i>	39
4.1	<i>(a) The “flat-top Gaussian” radial distribution of dipole positions, mimicking a realistic aperture illumination where the dipoles get less dense towards the edge of the dish and (b) the resulting 2D dipole distribution with a mask applied to mimic aperture blockage ensures effective illumination and avoids tapering off.</i>	45
4.2	<i>Jones matrix representation of the KAT-7-like beams produced by OSKAR and shown at 1 GHz: (a) real part (b) imaginary part. The intensity of the imaginary parts increases with fewer dipoles and becomes very less when more dipoles are used.</i>	46
4.3	<i>Histogram plots of the imaginary components in Fig. 4.2 showing the distribution of inaccuracies on the KAT-7 dish-like surface.</i>	47
4.4	<i>Mueller matrix representations of full polarisation beams produced at 1 GHz</i>	55
4.5	<i>Convolved full-sky polarisation maps using the non-distorted OSKAR beams. For example, we used the m_{II} beam in Fig. 4.4a to convolve Stokes I in Fig. 3.3 and produce the convolved map $I \rightarrow I$, then we used m_{QI} beam to convolve Stokes Q to obtain the convolved map $Q \rightarrow I$, also, using the m_{UI} beam to convolve Stokes U we produced the convolved map $U \rightarrow I$. The other convolved maps are produced in the same manner using their respective beams.</i>	58
4.6	<i>Systematic errors of full-sky maps produced by computing the relative error between the absolute of the convolved true sky maps and the corrupted sky maps due to gain and phase error beams.</i>	58

4.7	<i>Systematic errors of full-sky maps produced by computing the relative error between the absolute of the convolved true sky maps and the corrupted sky maps due to dipole orientation error beams.</i>	59
4.8	<i>Systematic errors of full-sky maps produced by computing the relative error between the absolute of the convolved true sky maps and the JVLA holography beams for antennas 5 and 6.</i>	59
4.9	<i>The top and middle maps depict the measured foregrounds of Stokes I, Q and U for using the non-distorted and the gain and phase error full polarisation beams respectively. The bottom maps are the corresponding errors in I, Q and U.</i>	62
4.10	<i>Convolved angular power spectra estimation of foreground maps. First row: Shows Stokes I spectra plots for using simulated beams and holography measured beams. Second row: Displays Stokes Q spectra plots for using simulated beams and holography measured beams. Third row: Displays Stokes U spectra plots for using simulated beams and holography measured beams.</i>	63
4.11	<i>Comparing polarisation leakages when there is no beam correction with correcting the beam errors in Stokes I: (a) Quantifies the amount of leakages into Stokes I which is caused by both measured (holography) and modelled (OSKAR) beams. The solid circular spectrum is the simulated 21-cm brightness temperature described by Alonso, Ferreira, and Santos (2014) at a $z \approx 0.67$. The solid thin spectrum ($Q + iU _T$), is the leakage in I when the true modelled beams in Fig. 4.4a are used. The dashed spectra plots ($Q + iU _{GP}$, $Q + iU _{XY}$, $Q + iU _{JVLA}$) are the leakages in I when we use modelled beams with gain, phase and dipole displacement and holography measured beams respectively. (b) These spectra plots show the estimate of the 21-cm signal when we correct for the errors in Stokes I beam.</i>	64
4.12	<i>These are the spectra plots of the systematic errors in Fig. 4.6. The notations GP and XY in the legends denote the residuals for gain-phase and dipole orientation errors in the OSKAR beams, that of HB depicts the errors in the holography beams. These errors are then used to estimate the imperfections in the simulation by computing the expected value of the standard deviations of the sampling distributions of the residual maps to produce Table A.1.</i>	65
5.1	<i>Expansion of eight orthogonal radial polynomial $R_n^{ m }(\rho)$ plots. Here, the value of unity can be obtained at the outer edge, since $R_n^{ m }(1) = 1$.</i>	69
5.2	<i>Representation of basis patterns of Zernike moments $Z_n^m(\rho, \theta)$ of order 10, plotted on a unit circle.</i>	70

5.3	<i>Spectral representation of the amplitude of MeerKAT primary beams for L band. The dotted lines are the Zernike plots with missing frequency channels due to high RFI whilst the solid lines are the DCT plots used to correct the bad channels for the respective Jones terms [XX (top-left), XY (top-right), YX (bottom-left), YY (bottom-right)].</i>	73
5.4	<i>Spectral representation of the phase of MeerKAT primary beams for L band. The dotted lines are the Zernike plots with missing frequency channels due to high RFI whilst the solid lines are the Sine (top) and Cosine (bottom) plots used to correct the bad channels for the respective Jones terms [XX (top-left), XY (top-right), YX (bottom-left), YY (bottom-right)].</i>	74
5.5	<i>Zernike reconstructed MeerKAT beam model at 990 MHz, using 20 and 5 strongest coefficients to model the gain and cross components respectively.</i>	75
5.6	<i>Radial profile of Fig. 5.5. (a) Using 5 strongest zernike coefficients for the Jones components. (b) Using 10 strongest zernike coefficients for the Jones components. (c) Using 20 strongest zernike coefficients for the gain components and 5 strongest zernike coefficients for the cross components.</i>	76
5.7	<i>Histogram plots showing the residual distribution. (a) Plots obtained from using 5 strongest zernike coefficients for the Jones components. (b) Plots obtained from using 10 strongest zernike coefficients for the Jones components. (c) Plots obtained from using 20 strongest zernike coefficients for the gain components and 5 strongest zernike coefficients for the cross components.</i>	77
5.8	<i>The expected value of the squared error loss between the holography beam and the predicted beam model with increase in the number of Zernike coefficients.</i>	78
5.9	<i>Measured Stokes I, Q and U convolved with reconstructed MeerKAT beam models with corresponding error maps.</i>	79
5.10	<i>The distribution of angular power plots displaying the errors due to perturbed Zernike fits in Stokes I map (left plots) and the intrinsic leakage in I (right plots) affect the 21 cm signal (solid circular spectrum plot).</i>	80
6.1	<i>A geometrical dual reflector model of SKA1-mid oriented in the xz – direction and generating highly contoured beam.</i>	83
6.2	<i>Far-field pattern cuts ($0^\circ \leq \phi \leq 315^\circ$) of the SKA1-mid showing the regions of the main, side lobes and cross polarisation levels for Band 1: Figs. 6.2a, 6.2c and 6.2e are the selected frequencies for the co-polar and that of the cross terms are Figs. 6.2b, 6.2d and 6.2f.</i>	86
6.3	<i>Far-field pattern cuts ($0^\circ \leq \phi \leq 315^\circ$) of the SKA1-mid showing the regions of the main, side lobes and cross polarisation levels for Band 2: Figs. 6.3a, 6.3c and 6.3e are the selected frequencies for the co-polar and that of the cross terms are Figs. 6.3b, 6.3d and 6.3f.</i>	87

6.4	<i>Far-field pattern cuts ($0^\circ \leq \phi \leq 315^\circ$) of the SKA1-mid showing the regions of the main, side lobes and cross polarisation levels for Band 5: Figs. 6.4a, 6.4c and 6.4e are the selected frequencies for the co-polar and that of the cross terms are Figs. 6.4b, 6.4d and 6.4f.</i>	88
6.5	<i>Zernike fit of band 1 EM beams at 450 MHz.</i>	91
6.6	<i>Zernike fit of band 2 EM beams at 990.5 MHz.</i>	92
6.7	<i>Zernike fit of band 5 EM beams at 4.6 GHz.</i>	93
6.8	<i>Spectral profile showing the various energy levels of Zernike coefficients for band 1 (350 – 1050 MHz).</i>	94
6.9	<i>Spectral profile showing the various energy levels of Zernike coefficients for band 2 (950 – 1760 MHz).</i>	94
6.10	<i>Spectral profile showing the various energy levels of Zernike coefficients for band 5 (8.4 – 13.6 GHz).</i>	95
6.11	<i>Perturbed beams for band 1 at 450 MHz.</i>	96
6.12	<i>Perturbed beams for band 2 at 990.5 MHz.</i>	97
6.13	<i>Perturbed beams for band 5 at 4.6 GHz.</i>	98
6.14	<i>Representation of IXR and the corresponding Stokes I beams. Figs. 6.14a, 6.14b, 6.14c show the plots for bands 1, 2 and 5 respectively.</i>	99
6.15	<i>Systematic errors of measured maps due to feed displacement at 450 MHz.</i>	102
6.16	<i>Systematic errors of measured maps using Zernike model beams at 450 MHz.</i>	102
6.17	<i>Systematic errors of measured maps due to feed displacement at 990.5 MHz.</i>	103
6.18	<i>Systematic errors of measured maps using Zernike model beams at 990.5 MHz.</i>	103
6.19	<i>Systematic errors of measured maps due to feed displacement at 4.6 GHz.</i>	104
6.20	<i>Systematic errors of measured maps using Zernike model beams at 4.6 GHz.</i>	104
6.21	<i>Convolved full-sky maps at 4.6 GHz with respective error in Stokes I, Q and U.</i>	105
6.22	<i>Comparing the distribution of angular power plots between corrected beam errors due to Zernike fits or feed displacement in Stokes I map (left plots) and intrinsic polarisation leakage in I (right plots) and how these affect both the 21 cm and CO signal (solid circular spectrum plot). (a) For band 1 at 450 MHz (b) For band 2 at 990.5 MHz (c) For band 5 at 4.6 GHz</i>	106
A.1	<i>Fully polarised distorted primary beams of KAT-7. (a) Due to gain and phase errors. (b) Due to dipole orientation errors.</i>	123
A.2	<i>1 GHz holography measured Mueller beams of JVLA. (a) Antenna 5. (b) Antenna 6.</i>	125

A.3 Convolved full-sky polarisation maps using the corrupted primary beams in Fig. A.1a. Here also, we used the m_{II} beam in Fig. A.1a to convolve Stokes I in Fig. 3.3 and produce the convolved map $I \rightarrow I$, then we used m_{QI} beam to convolve Stokes Q to obtain the convolved map $Q \rightarrow I$, also, using the m_{UI} beam to convolve Stokes U we produce the convolved map $U \rightarrow I$. The same approach is repeated to obtain (in row 2) $I \rightarrow Q, Q \rightarrow Q, Q \rightarrow U$ and (in row 3) $I \rightarrow U, Q \rightarrow U, U \rightarrow U$ by using the corresponding beams m_{IQ}, m_{QQ}, m_{UQ} and m_{IU}, m_{QU}, m_{UU}	126
A.4 Convolved full-sky polarisation maps using the corrupted primary beams in Fig. A.1b.	126
A.5 Measured Stokes I, Q and U for holography measured beams of JVLA with corresponding errors terms.	127

List of Tables

2.1	Radio Frequency Bands	11
3.1	Measured Spectral Indices at Different Frequency Bands	35
5.1	Relationship between single and double index schemes to third order.	71
A.1	Error introduced in the power spectrum estimation	127

List of Abbreviations

2dF	2-degree-Field
6dF	6-degree-Field
AF	Array Factor
APERTIF	APERture Tile In Focus
ASKAP	Australian Square Kilometre Array Pathfinder
BINGO	Baryon acoustic oscillations In Neutral Gas Observations
BOSS	Baryon Oscillation Spectroscopic Survey
BSS	Blind Source Separation
CDF	Cumulative Distribution Function
CHIME	Canadian Hydrogen Intensity Mapping Experiment
CMB	Cosmic Microwave Background
COBE	COsmic Background Explorer
CSIRO	Commonwealth Scientific and Industrial Research Organization
DDA	Dense Aperture Array
DD	Direction Dependent
DI	Direction Indeependent
DGSE	Diffuse Galactic Synchrotron Emission
EM	ElectroMagnetic
EVLA	Expanded Very Large Array
FFT	Fast Fourier Transform
FAST	Five-hundred-meter Aperture Spherical Radio Telescope
FNBW	First Null Beam Width
FoM	Figure of Merit
FoV	Field-of-View
GBT	Green Bank Telescope
GMRT	Giant Metre wave Radio Telescope
GRASP	General Reflector Antenna Software Package
HBA	High-Band Antennas
HEALPix	Hierarchical Equal Area iso Latitude Pixelation
HIRAX	Hydrogen Intensity and Real-time Analysis eXperiment
HPBW	Half Power Beam Width
ICA	Independent Component Analysis
ILC	Internal Linear Combination
IEEE	Institute of Electrical and Electronics Engineers
IGM	InterGalactic Medium

IM	Intensity Mapping
ISM	InterStellar Medium
IXR	Intrinsic Cross Polarisation
KAT	Karoo Array Telescope
LOFAR	LOw-Frequency ARray
NRAO	National Radio Astronomy Observatory
PAF	Phased-Array Feed
PAH	Polycyclic Aromatic Hydrocarbon
RF	Radio Frequency
RFI	Radio Frequency Interference
SDSS	Sloan Digital Sky Survey
SKA	Square Kilometre Array
SNR	Signal-to-Noise Ratio
TICRA	electromagneTIC RAdiation
VLA	Very Large Array
WMAP	Wilkinson Microwave Anisotropy Probe
WSRT	Westerbork Synthesis Radio Telescope

Physical Constants

Constant Name	<i>Symbol = Constant Value with units</i>
Speed of Light	$c = 2.997\,924\,58 \times 10^8 \text{ m s}^{-1}$ (exact)
Boltzmann constant	$k_B = 1.380\,648\,8 \times 10^{-23} \text{ J K}^{-1}$
Planck's constant	$h = 6.626\,069\,57 \times 10^{-34} \text{ J s}$

List of Symbols

Symbol	Name	Unit
d	distance	m
P	power	$\text{W} (\text{J s}^{-1})$
ν	frequency	Hz
T	thermodynamic temperature	K
t	time	s
ε	electric field	V m^{-1}
H	magnetic field	A m^{-1}
D	electric induction	C m^{-2}
B	magnetic induction	Wb m^{-2}
\mathcal{J}	electric current density	A m^{-2}
\mathcal{M}	magnetic current density	V m^{-2}

Chapter 1

Introduction

Overview

This Chapter introduces us to the general background of the research by briefly discussing the “spin-flip” line of neutral hydrogen, with a rest wavelength of 21 cm and then moves on to discuss the significance of intensity mapping experiments. The research problems, key objectives, justification and the entire structure of the thesis are also outlined.

1.1 The Origin of the Hydrogen 21 cm Line

Despite the fact that space is very empty and there is a great distance between the stars in the Milky Way, the gap between these stars consists of dust and a very diffuse medium of gas of which astronomers refer to this matter and radiation in space as *interstellar medium* (ISM). This ISM is made up of neutral hydrogen gas (HI), molecular gas (also known as H₂), ionised gas (H_{II}) and dust grains (Duffy et al. 2012). A large portion of the mass of the ISM in the Milky Way is in the form of warm ($10^3 - 10^4$)K and cool (50 – 100)K atomic HI gas (Bolonkin 2017; Knee and Brunt 2001). The cold atomic HI gas can emit a particular wavelength of radio energy from a slight energy change in the hydrogen atoms (Landeck et al. 2017), that is, the electron and proton spins of a hydrogen atom in the ground state may point either in the same or opposite directions such that, the same spin state has slightly more energy than the oppose spin state. The energy difference (“ hyperfine splitting”) is 60 millionths of the energy between the ground state and the first excited state, making the state with the same spins unstable. When the hydrogen atom flips between the same-spin state to the anti-parallel state as shown in Fig. 1.1, it emits electromagnetic (EM) radiation with a frequency of approximately 1420.406 MHz corresponding to a wavelength of 21 cm. This wavelength or frequency falls within the microwave radio region of the EM spectrum as displayed in Fig. 1.2 by (Miller 1998) and therefore, using large radio telescopes, radio astronomers can observe

the 21 cm line even in a very distant spiral galaxies. Most often, when the observation is done, it's line is not sharp. This is because, a spiral galaxy rotates in such a way that, if it is marginally edge-on to our line of sight, a portion of the HI regions move away from us whilst others move towards us. This *Doppler effect* broadens the 21 cm line into a double peak. It redshifts the radiation from the regions that move away from us and blueshifts the vice versa. Therefore, the faster the rotation of the galaxy, the greater the line broadening. Radio observations of the 21 cm line can measure the value of the rotational velocity of a spiral galaxy. In addition, the 21 cm emission line from HI is an extremely useful tool for studying gas in the ISM of external galaxies and tracing the large scale distribution of galaxies in the universe (López et al. 2017) since HI is detectable in most spiral galaxies and in some elliptical galaxies. An in-depth explanation to this section can be obtained from Burke and Graham-Smith (2009), Ciardi and Madau (2003), Madau, Meiksin, and Rees (1997), and Webb (1999).

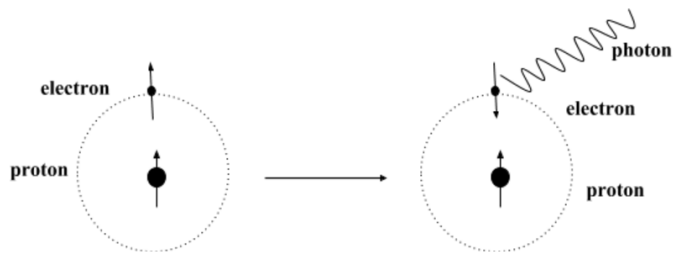


Figure 1.1: When the electron flips its spin, the atom emits a photon with a wavelength of 21 cm

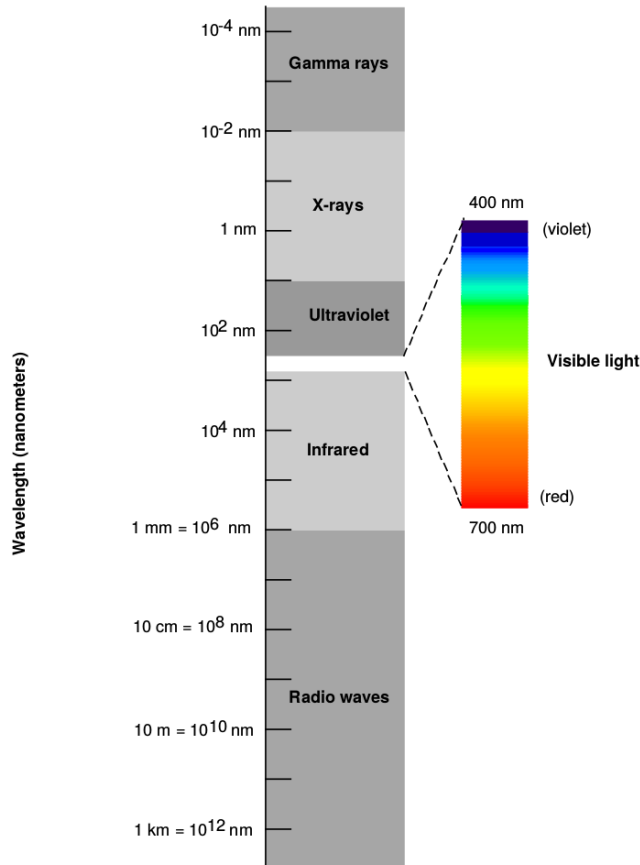


Figure 1.2: The Properties of Electromagnetic Radiation

1.2 HI Intensity Mapping

Over the past two decades, the galaxy redshift surveys such as 2-degree-Field (2dF¹) (Cole et al. 2005; Colless et al. 2003), 6-degree-Field (6dF²) (Beutler et al. 2011), WiggleZ³ (Blake et al. 2011), Baryon Oscillation Spectroscopic Survey (BOSS⁴) (Anderson et al. 2012) and Sloan Digital Sky Survey (SDSS⁵) (Percival et al. 2010; Sadeh, Feng, and Lahav 2015) have used optical spectroscopy to specifically observe millions of individual galaxies, determine each redshift and use these to estimate the power spectrum for each (Peterson et al. 2009; Santiago et al. 1996; Santiago et al. 1995). An inference can therefore be made about the acoustic scale, by considering a simple biasing between the galaxy density field and that of the underlying matter density. As discussed extensively by Peterson et al. (2009) and Smoot and Debono (2017), using the 21 cm line of neutral hydrogen, a massive-scale structure of the Universe can be mapped in 3D to observe the full-sky across the redshift range from 0 to 5. This is achievable by studying specific intensity with resolution ~ 10 Mpc instead of the usual galaxy redshift survey. At high redshift, it normally requires very large collecting areas like the design of the Square Kilometre Array (SKA), even though, the SKA is not

¹<http://www.2dfgrs.net/>

²<http://www-wfau.roe.ac.uk/6dFGS/>

³<http://wigglez.swin.edu.au/site/>

⁴<http://www.sdss3.org/surveys/boss.php>

⁵<http://www.sdss.org/>

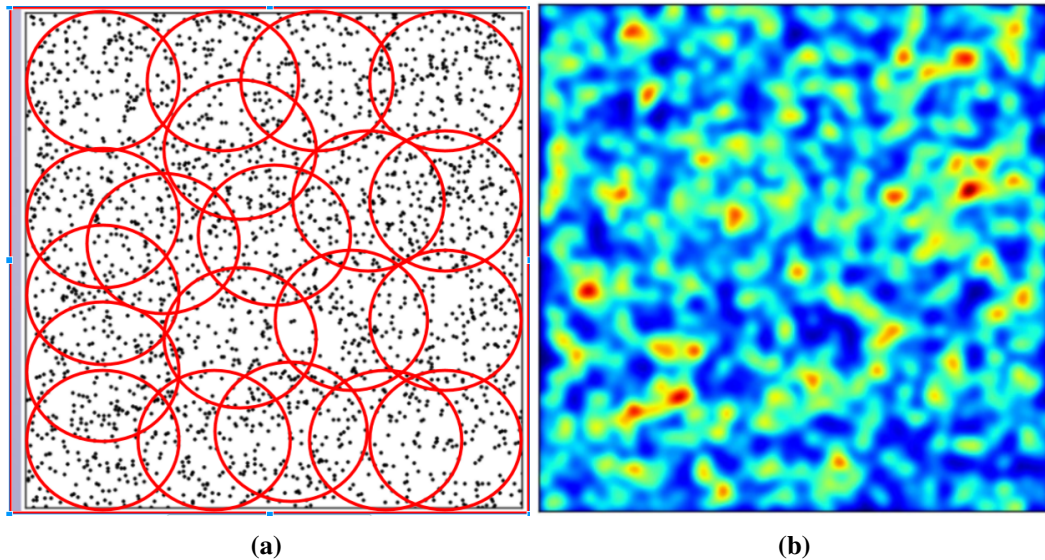


Figure 1.3: Simulated fluctuations in the brightness temperature of 21 cm emission from galaxies. Red indicates over-density and blue under-density. The circles show how to perform IM experiment with the radio telescope in order to measure the 21 cm emission.

exclusively constructed for IM experiments. Radio telescopes with apertures ~ 100 m have sufficient surface brightness sensitivity to detect HI at high redshift if they have a filled or close to filled aperture, but they will preferentially detect objects of angular size comparable to their resolution which will typically be clusters.

Meanwhile, the recent understanding of 21 cm *Intensity Mapping* (IM) (Camera et al. 2014; Chang et al. 2008; Santos et al. 2015; Wolz et al. 2015; Wolz et al. 2014) in radio astronomy, is to use the full intensity field $T(\nu, \theta, \phi)$ in terms of frequency ν and sky position (θ, ϕ) to measure the power spectrum directly, without actually localizing the individual galaxies. Thus, in IM experiment, the 21 cm emissions are considered as a diffuse source without attempting to detect individual objects as shown in Fig. 1.3. The average signal is expected to be $\sim 100\mu\text{K}$ on degree scales with the bandwidth of \sim few MHz (Battye et al. 2012), with order one fluctuation. Detecting this involves a meticulous subtraction of the continuum emission from our own Galaxy and extragalactic sources explaining the fact that, the continuum emission is expected to be spectrally smooth as compared to the 21 cm emission. Therefore, radio telescopes used in IM experiment require a resolution and sensitivity sufficient enough to measure the large scale structure and especially the Baryon Acoustic Oscillation (BAO) wavelengths. Section 1.3 briefly discusses the importance of IM observational techniques and some of the current radio instruments purposely designed to perform this kind of experiment.

1.3 Significance of Intensity Mapping Techniques

IM technique has the advantage of not resolving sources but instead measure all the intensity originating from a region and also, include radiation from faint sources and from the diffuse intergalactic medium (IGM) which at high redshifts could not be detected in other ways but whose contribution to the total signal is often important. These intensity maps also have the advantage of containing spatial information that can be used to further understand the processes of structure formation or as a cosmological probe since the fluctuations in the intensity of emission or absorption lines are correlated with underlying dark matter density fluctuations (Bass et al. 2009, p. 366). Also, with the observational data from several lines one will also be able to cross-correlate the lines which can be used to remove foreground from 21 cm observations. This is achievable since diverse emission lines will be observed at different frequencies and so will be contaminated mainly by uncorrelated line foregrounds. In addition, the technique allows smaller and cheaper telescopes without long baselines such as Hydrogen Intensity and Real-time Analysis eXperiment (HIRAX), to be used in such experiments, hence increasing the science output in cosmology.

Presently, several IM experiments are in operation, such as the Green Bank Telescope (GBT⁶), Baryon acoustic oscillations In Neutral Gas Observations (BINGO⁷) (Battye et al. 2012), Canadian Hydrogen Intensity Mapping Experiment (CHIME⁸) (Bandura et al. 2014; Newburgh et al. 2014), Tianlai⁹ (Chen 2012) and Five-Hundred-Meter Aperture Spherical Radio Telescope (FAST¹⁰) (Nan et al. 2011). Among these instruments for IM experiments, the GBT produced the first HI signal at $z \sim 0.8$ and was cross-correlated with large-scale structure traced by galaxies in the WiggleZ dark energy survey (Masui et al. 2013; Contreras et al. 2013). Moreover, the capabilities of the next generation of radio telescopes such as dense aperture arrays for the SKA and HIRAX make it only more promising, being the fact that, the technique is relatively “cheaper” compared to the usual galaxy surveys described in the first paragraph of section 1.1. Furthermore, these new instruments will provide a broader range of frequencies and a very massive survey area in order to produce HI intensity maps. IM experiments can be carried out at different redshifts either in auto-correlation mode, that is, single dish observations like BINGO (Battye et al. 2012) or interferometric mode like CHIME (Newburgh et al. 2014).

⁶<https://science.nrao.edu/facilities/gbt>

⁷<http://www.bingotelescope.org/en/>

⁸<https://chime-experiment.ca/>

⁹<http://tianlai.bao.ac.cn/>

¹⁰<http://fast.bao.ac.cn/en/>

1.4 Problem Identification

Radio observations made with radio interferometers suffer from two main instrumental effects namely; Direction-Independent (DI) and Direction-Dependent (DD) effects. The complex instrumental gains in Fourier components due to the electronic devices that follow the antenna feeds are DI effects. These DI effects are easily calibrated and corrected separately from imaging. The DD effects are much more complicated, since they are applied during imaging and therefore, are transformed into a convolution of the measured components. This makes it very relevant to both calibrate the unknown DD effect and then correct the known or measured one. The ionospheric structure and the primary beam response of an alt-azimuthally mounted telescope are the common sources of DD effects. These results in telescope mis-pointings and antenna structure deformation caused by the wind and gravitational load on the dishes, differential heating, etc. These two time-varying terms go a long way to limit observations with the existing as well as the next generation of telescopes currently under construction. The challenges put forward by the ionosphere are especially stern at very low frequencies and with large interferometric arrays such as LOFAR¹¹ (van Haarlem et al. 2013; Wijnholds et al. 2010).

These challenges are also very crucial in IM experiments. For instance, using the IM technique requires the correct subtraction of the foreground continuum signal from our galaxy as well as extra-galactic sources, since the HI signal is weaker by several orders of magnitude than the astrophysical foreground signals (Yatawatta et al. 2013). Existing foreground subtraction techniques (Alonso et al. 2015; Gu et al. 2013) depend on the smoothness of this signal as a function of frequency. In the absence of instrumental corruptions, this assumption is perfectly valid. However, physical observations are affected by DD effects, that is, variations in gain amplitude and phase over the field-of-view (FoV), as well as polarisation leakage. In IM experiment, the primary beam in particular is a challenge, as it modulates the intensity as a function of the sky position, which is exactly what is being measured by this technique in the first place. In the case of Karoo Array Telescope (KAT-7¹²), MeerKAT¹³ and upcoming dish arrays, this will be dominated by pointing errors and polarisation leakages. Existing approaches to DD effects such as DD solutions (Smirnov 2011) are not directly applicable, since individual galaxies are not mapped out by this experiment. Hence, a different approach to map out DD effects in a stochastic sense, need to be developed.

1.5 Research Objective

The key focus of this project is to develop IM techniques for mapping out primary beams of a radio telescope and then, introduce realistic errors to perturb these modelled beams. We then attempt a correction and calibration of these distorted modelled beams and ultimately,

¹¹<http://www.lofar.org/>

¹²<http://public.ska.ac.za/kat-7>

¹³<http://www.ska.ac.za/gallery/meerkat/>

use the final data for intensity mapping experiments. Thus, we use these modelled beams to simulate the full-sky polarisation maps and then, determine the amount of foregrounds that have corrupted the total intensity due to polarisation leakage and errors in the primary beams which have not been accounted for. The study used Oxford’s Square Kilometre Array Radio-telescope (OSKAR¹⁴), a beamforming simulator, specifically developed to generate simulated data from large aperture arrays, such as those envisaged for phase I of the SKA, to simulate the notional beams of KAT-7. The next beams produced for this study are Zernike models reconstructed from MeerKAT holography measured beams. The last primary beams used in this research are obtained from the Generalized Reflector Antenna farm analysis Software Package (GRASP¹⁵) of electromagneTIC RAdiation (TICRA) software.

1.6 Delimitation

The study’s main scope is to quantify two effects:

- (i) the contribution of polarisation leakage to the measured HI and CO power spectrum, given some more or less realistic primary beams and
- (ii) the uncertainty on the estimate of (i) introduced by unmodelled perturbations in the primary beam.

1.7 Rationale and Motivation

Normally, antenna feeds measure the components of a signal along two orthogonal polarization states by two separate feeds. The signals from the two feeds travel through essentially independent paths into the correlator. However, due to mechanical imperfections in the feed or imperfections in the electronics, the two signals can leak into each other at various points in the signal chain. When a portion of the two signals leak into each other, it is referred to as the *polarisation leakage*. In terms of Stokes parameters, this produces an unwanted transfer of a signal between the Stokes I and QUV measurements. It is a particular problem for IM observations because polarised foreground signals are generally not smooth as a function of frequency due to Faraday rotation of the QU vector (Asad et al. 2015). Leakage, therefore, results in a non-smooth foreground component being introduced into Stokes I , one which is not amenable to traditional foreground subtraction techniques. Correcting for leakage is a challenge, since it varies both as a function of time and frequency, hence, it is expected to limit observations with the existing as well as upcoming radio telescopes presently under construction (Bhatnagar et al. 2008). The study is motivated by this and therefore, concentrates rather on the effects of the primary beam particularly, DD polarisation leakage. The potential of IM has already been demonstrated (Wolz et al. 2015; Chang et al. 2008; Wolz et al. 2014;

¹⁴<http://www.oerc.ox.ac.uk/ska/oskar2/>

¹⁵<http://www.ticra.com/products/software/grasp>

Loeb and Wyithe 2008; Santos et al. 2015) and the capabilities of upcoming telescopes as mentioned in section 1.3 make it only more promising. However, considerable research into this technique is necessary since there are some sort of technical challenges in terms of data analysis and in particular measuring the primary beam response, which has to be overcome in order to make such an experiment work to its full potential.

1.8 Thesis Outline

The thesis is divided into seven different chapters as depicted in Fig. 1.4.

Chapter 1 briefly introduces the research topic by commencing with the general background of 21 cm emission line and continues by presenting the significance of IM experiment and clearly stating the research problem and objective. This chapter also justifies why the study is conducted and briefly explains how the simulations are done to produce the primary beams for various antenna types.

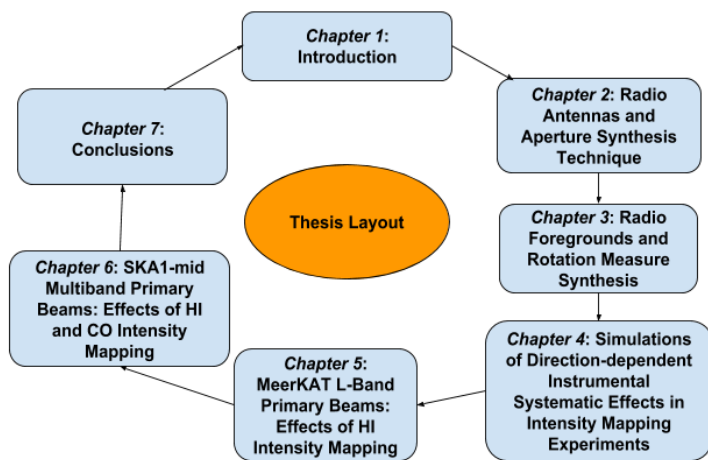


Figure 1.4: Structure of the thesis

The Chapter 2 discusses about radio telescope antennas where we clearly look at the numerous designs, operations and performances of antennas. Beamforming and radio array types are reviewed in this chapter. Also, we discuss a special technique known as aperture-synthesis, whereby we combine radio antennas as well as the Earth rotation to improve the u, v plane coverage for construction of radio images. The cheapest super-synthesis telescope is formed by 2 antenna elements. In one direction, the baseline varies through the movement of one antenna and in the other direction, the baseline vary through the Earth's rotation.

Foregrounds and rotation measure synthesis are discussed in Chapter 3. Here, the study mainly focused on synchrotron emission, some foreground separation techniques and rotation measure.

Chapter 4 presents the first methodology employed in this research. In this chapter, we describe extensively the observational effects of primary beam perturbation of KAT-7, using the OSKAR software package. We then go ahead to determine the polarisation leakage by introducing the convolution technique to simulate the foregrounds. Here, KAT-7 is used as a conceptual example for the purposes of this study. The study moves on further to compare the power spectrum of the simulated beams with the Jansky Very Large Array (JVLA¹⁶) holography measured beams.

Chapter 5 describes the second methodology of this study. In this chapter, we produce modelled beams by fitting Zernike polynomials on MeerKAT measured beams to compute the reconstructed beams with less coefficients. These modelled beams are then used to simulate the foregrounds to estimate the effect on IM.

The third methodology in this work is presented in Chapter 6, where we generate GRASP simulated beams of SKA1-mid for bands 1, 2 and 5. These EM beams of various bands are reconstructed with Zernike model, using the strongest Zernike coefficients and in addition, we try to perturb these GRASP beams by introducing errors in the feed coordinates to displace the feed from its principal focus. Finally, we perform IM experiment by simulating the foregrounds with all these modelled beams to estimate not only HI flux at lower bands but also, CO signal too at higher bands.

Conclusions and recommendations are discussed in Chapter 7.

¹⁶<https://science.nrao.edu/facilities/vla>

Chapter 2

Radio Antennas and Aperture Synthesis Technique

Overview

Chapter Two introduces us to the general antenna parameters that are significant to describe the operation and performance of an antenna. A further discussion is made on how to mathematically derive the Stokes parameters from wave propagation. Beamforming and types of radio arrays are also discussed in this chapter. Finally, we give a brief description on super-synthesis technique for constructing radio images.

2.1 Introduction

The physical laws governing all classical EM phenomena are the famous Maxwell's equations:

$$\left\{ \begin{array}{l} \nabla \times \boldsymbol{\epsilon}(\mathbf{r}, t) = -\frac{\partial}{\partial t} \mathcal{B}(\mathbf{r}, t) - \boldsymbol{\mathcal{M}}(\mathbf{r}, t) \\ \nabla \times \mathbf{H}(\mathbf{r}, t) = \frac{\partial}{\partial t} \mathcal{D}(\mathbf{r}, t) + \boldsymbol{\mathcal{J}}(\mathbf{r}, t) \end{array} \right. \quad (2.1)$$

where,

- $\boldsymbol{\epsilon}(\mathbf{r}, t)$ electric field V/m ,
- $\mathbf{H}(\mathbf{r}, t)$ magnetic field A/m ,
- $\mathcal{D}(\mathbf{r}, t)$ electric induction C/m^2 ,
- $\mathcal{B}(\mathbf{r}, t)$ magnetic induction Wb/m^2 ,

Table 2.1: Radio Frequency Bands

Band	Range of Wavelength (cm)	Frequency (GHz)
L	30 – 15	1 – 2
S	15 – 7.50	2 – 4
C	7.5 – 3.75	4 – 8
X	3.75 – 2.50	8 – 12
Ku	2.50 – 1.67	12 – 18

$$\begin{aligned}\mathcal{J}(\mathbf{r}, t) & \text{ electric current density (source) } A/m^2, \\ \mathcal{M}(\mathbf{r}, t) & \text{ magnetic current density (source) } V/m^2.\end{aligned}$$

The mathematical model in equation 2.1 provides a complete description of the way electric and magnetic fields are generated and altered by each other, as well as by charges and currents. The electric and magnetic fields are represented as position vectors, in terms of amplitude and phase. The fields $\boldsymbol{\epsilon}$ and \boldsymbol{H} vary in magnitude and orientation depending on both the position \mathbf{r} and time t , at which they are measured. The operator ∇ denotes the presence of some type of rotation in the variables of the equation. In effect, the change of $\boldsymbol{\epsilon}$ and \boldsymbol{H} fields over time are equivalent to the change in the direction of the \boldsymbol{B} and \boldsymbol{D} fields respectively as EM waves move forward in space. These EM waves propagate at the speed of light and in an outward direction with respect to their origin. This phenomenon is termed as *EM Radiation* and obviously, in order to produce EM radiation, we must introduce a device capable of holding an alternating electric current. This device is known as an *antenna*. An antenna is therefore, defined as an electrical device designed to radiate or receive EM waves.

In radio astronomy, the antenna of a radio telescope operates in reception mode such that, a radio wave incident upon the antenna induces an electric current on its input terminals which can then be converted back into a radio frequency (RF) signal. This RF can be observed with a radio telescope at different ranges called *bands* as presented in Table 2.1 according to Institute of Electrical and Electronics Engineers (IEEE) standard. The KAT-7 can observe at L-band frequency which is very good for investigating HI IM experiments.

2.2 Antenna Parameters

The numerous designs of an antenna make it necessary to describe the performance of an antenna. This of course, requires a clear understanding of the parameters of an antenna. This section therefore discusses the antenna parameters:

2.2.1 Field Regions

The EM fields of an antenna display different patterns depending on the space surrounding the antenna at which they are measured. This surrounding space can be classified into three regions as depicted in Fig. 2.1 (see Balanis 2005, p. 34):

- *Reactive near-field*: This is the closest region of the antenna. The energy in this region oscillates towards and away from the antenna, making it purely reactive and completely storing the energy. This makes both the electric and magnetic fields out of phase. The outer boundary for this region is at a distance $R < 0.62\sqrt{\frac{D^3}{\lambda}}$ where, R is the distance from the antenna surface, D is the largest dimension of the antenna and λ is the wavelength in metres. The frequency of the EM waves is related to the wavelength such that, $\lambda = \frac{c}{\nu}$ where, $c = 2.99792458 \times 10^8$ m/s is the speed of light and ν is the frequency in Hz.
- *Radiating near-field*(also known as *Fresnel* region): This region lies between the reactive near-field and the far-field. The field strength in this region is lesser as compared to the reactive near-field. Thus, as the surrounding space from the antenna increases, the EM fields become less reactive, making part of the energy to be converted into radiation. Also, the angular field distribution in this region is a function of the distance from the antenna and hence, the outer boundary is at a distance $R < 0.62\frac{D^2}{\lambda}$.
- *Far-field* (also known as *Fraunhofer* region): This region exists at a distance $R > 2\frac{D^2}{\lambda}$. The reactive fields are no longer present and only the radiation fields exist. Also, the electric and magnetic fields in this region are perpendicular and in-phase. The ratio between their magnitudes are constant. Furthermore, the general radiation pattern in this region remains the same regardless of the distance from the antenna.

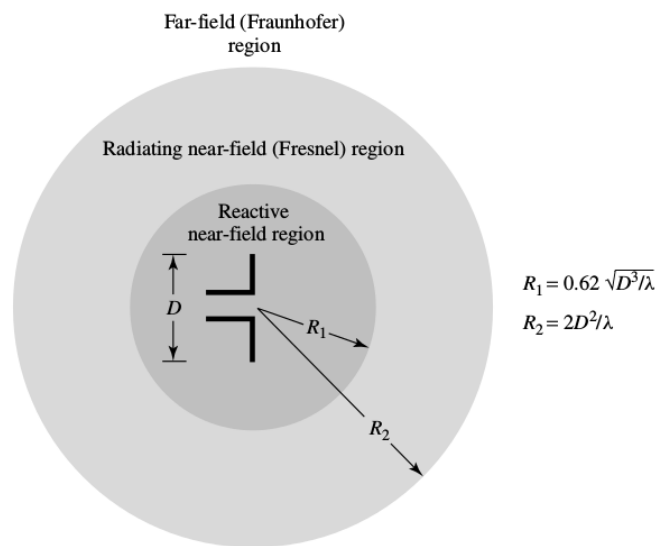


Figure 2.1: The different field regions of an antenna.

As the observation distance changes from near to far fields, the radiation pattern of an antenna also changes in shape in terms of amplitude and phase due to the variations of the fields.

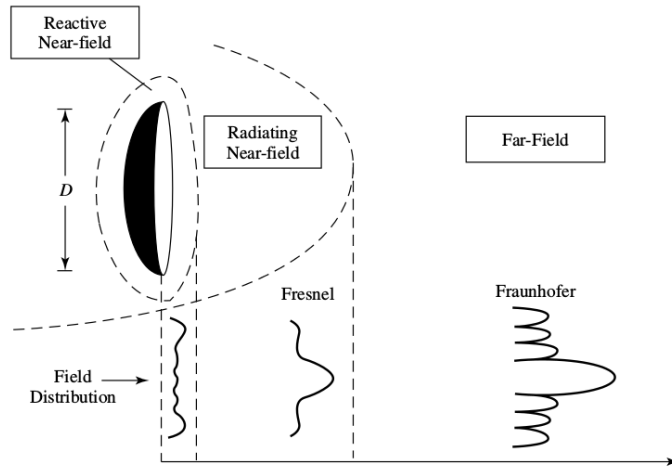


Figure 2.2: The different field regions of an antenna.

In Fig. 2.2 (see Balanis 2005, p. 35), the radiation pattern is almost uniformly distributed in the reactive near-field region. As the observation is gradually moved towards the radiating near-field, the radiation pattern begins to smooth and form lobes. The radiation pattern is fully formed at the far-field with minor and major lobes.

In radio astronomy, the antenna of a radio telescope operates in the far-field of the feed system to produce the desired illumination of the antenna.

2.2.2 Radiation Patterns

The antenna *pattern* is measured at the far-field region since there is no cause of change in the pattern when there is an increase in the distance. It describes the response of an antenna as a function of direction and generally comprises of a number of lobes as displayed in Fig. 2.3 (see Kraus 1966, p. 153). The lobes are briefly discussed as follows:

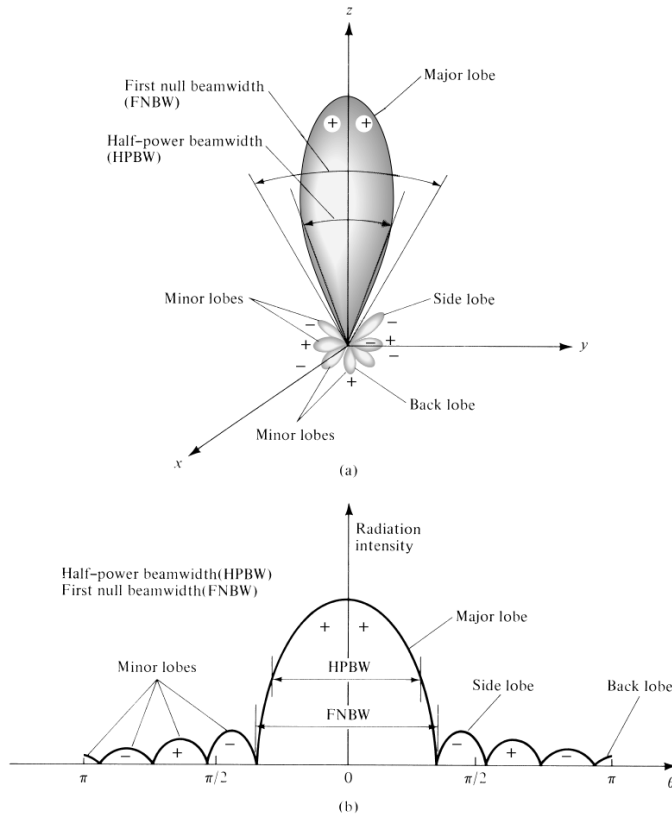


Figure 2.3: (a) Antenna pattern lobes in polar coordinates. (b) Antenna pattern lobes in linear power scale.

- The *major lobe* or the *main beam* contains the direction of maximum radiation. It is actually the region where the radiated power is most intense.
- Radiation from undesired direction is termed *minor lobe*. The highest minor lobe is referred to as the *side lobe* which is often adjacent to the main lobe as illustrated in Fig. 2.3. The minor lobe containing the direction opposite to that of the main beam is referred to as the *back lobe*.

2.2.3 Beamwidth

The angular distance between two identical points on opposite side of the pattern maximum is termed *beamwidth* of a pattern. The beamwidth is mostly presented in two ways:

- *Half Power Beam Width (HPBW)*: This is the angular difference between the points where the radiation intensity reaches half of its maximal value as shown in Fig. 2.3.
- *First Null Beam Width (FNBW)*: This is the angular difference between the two nulls enclosing the main lobe also presented in Fig. 2.3.

2.2.4 Radiation Intensity

The intensity of radiation is very dominant at the far-field region. It is mathematically expressed in terms of the far-zone electric field of an antenna:

$$U(\theta, \phi) = \frac{r^2}{2\eta} |\mathbf{E}(r, \theta, \phi)|^2 \quad (2.2)$$

where, U = radiation intensity (W/unit solid angle), $\mathbf{E}(r, \theta, \phi)$ = far-zone electric-field intensity of the antenna, r = radial electric-field component. The elevation angle θ describes the antenna tilt relative to the horizon while the azimuth angle ϕ describes the antenna traverse in a zero tilt state.

2.2.5 Radiation Patterns Types

There are three main categories of radiation patterns (see Fig. 2.4) namely:

- *Isotropic Radiation Pattern*: This results in constant pattern (spherical radiation pattern) in both azimuth and elevation planes. This hypothetical isotropic pattern is used as a reference to calculate antenna gain.
- *Omni Directional Radiation Pattern*: This pattern results in a uniform main beam at a particular plane and a constant decreasing pattern in the other. Thus, the pattern is 'dough-nut' in shape.
- *Directional Radiation Pattern*: This pattern contains one clear main beam in both azimuth and elevation planes.

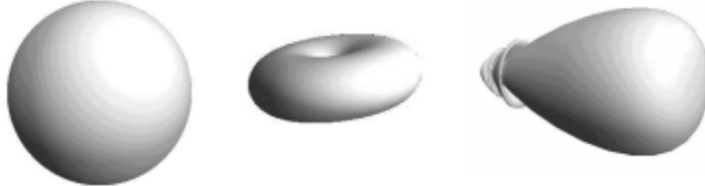


Figure 2.4: Graphical representation of antenna radiation properties. From left: shows the Isotropic patterns, middle: presents the Omni Directional Radiation Pattern and right: Directional pattern.

2.2.6 Gain

The antenna gain G , is expressed as;

$$G = 4\pi \frac{U(\theta, \phi)}{P_{in}} \text{ (dimensionless)} \quad (2.3)$$

where, U = radiation intensity and P_{in} is the overall accepted power.

The antenna gain takes into account the antenna efficiency since it is a measure of how much

power the antenna radiates in a certain direction, relative to how much power was incident upon the antenna.

2.3 EM Wave Polarisation

Consider a plane wave propagating in the positive z direction as in Fig. 2.5, with electric-field components in the x and y directions as given by

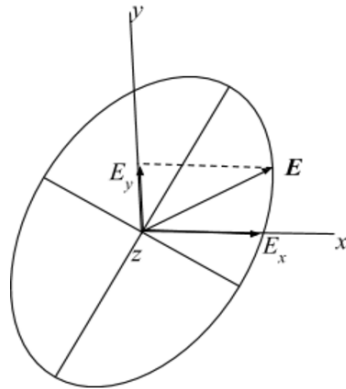


Figure 2.5: Relation of instantaneous electric-field vector \mathbf{E} to polarisation ellipse

$$E_x(z, t) = E_1 \cos\{\omega t - \beta z + \delta_x\} \quad (2.4a)$$

$$E_y(z, t) = E_2 \cos\{\omega t - \beta z + \delta_y\} \quad (2.4b)$$

where, the constant terms E_1 and E_2 characterize the maximum amplitude of x, y components respectively, $\omega = 2\pi\nu$ is the angular frequency, $\beta = 2\pi/\lambda$ is the measure of the ellipticity and δ_x, δ_y are phases of E_x and E_y respectively. Equations 2.4a and 2.4b characterize the two linearly polarised waves in the x and y directions respectively.

The resultant field is obtained by adding equation 2.4a to 2.4b vectorially:

$$\begin{aligned} \mathbf{E}(z, t) &= \hat{x}E_x(z, t) + \hat{y}E_y(z, t) \\ &= \hat{x}E_1 \cos\{\omega t - \beta z + \delta_x\} + \hat{y}E_2 \cos\{\omega t - \beta z + \delta_y\} \end{aligned} \quad (2.5)$$

where, \hat{x}, \hat{y} = unit vectors in x and y directions. Therefore, at $z = 0$, equation 2.5 becomes;

$$\mathbf{E}(t) = \hat{x}E_1 \cos\{\omega t + \delta_x\} + \hat{y}E_2 \cos\{\omega t + \delta_y\} \quad (2.6)$$

As clearly presented in Kraus 1966, p. 109, by eliminating the time t in equation 2.6, we obtain the most general expression of an ellipse as;

$$aE_x^2 - bE_xE_y + cE_y^2 = 1 \quad (2.7)$$

where, $a = 1/E_1^2 \sin^2(\delta)$, $b = 2 \cos(\delta)/E_1E_2 \sin^2(\delta)$, $c = 1/E_2^2 \sin^2(\delta)$ and $\delta = \delta_y - \delta_x$. Equation 2.7 shows that at any specific time t , the locus of points characterized by the propagation of E_x and E_y will trace out this curve. In equation 2.7, the product term E_xE_y actually shows a rotated ellipse. In general, the axes of the ellipse are not in x and y directions and therefore, the general case of elliptical polarisation as in Fig. 2.5 is presented in equation 2.5.

Obviously, from equation 2.5 if $E_1 = 0$, the wave is *linearly polarised* in the y direction and if $E_2 = 0$, the wave is linearly polarised in the x direction. If $\delta = 0$ and $E_1 = E_2$, the wave is linearly polarised at 45° with respect to the x axis. When $\delta = +90$ and $E_1 = E_2$, the wave is said to be *left circularly polarised* and when $\delta = -90$, it is known to be *right circularly polarised*.

2.3.1 Derivation of the Stokes Polarisation Parameters

In section 2.2, we dealt with fully polarised waves where, E_1, E_2 and δ are considered constants. A monochromatic (i.e. single-frequency) radiation is of this form. However, generally, in radio astronomy, the emission from celestial radio sources extends over wide frequency range and within any finite bandwidth $\Delta\nu$ consists of the superposition of a large number of statistically independent waves of a variety of polarisations. The resultant wave is said to be *randomly polarised*. In this section we consider a pair of plane waves that are orthogonal to each other at a point in space and choosing $z = 0$:

$$E_x(t) = E_1(t) \cos\{\omega t + \delta_x(t)\} \quad (2.8a)$$

$$E_y(t) = E_2(t) \cos\{\omega t + \delta_y(t)\} \quad (2.8b)$$

where, $E_1(t), E_2(t)$ are the instantaneous amplitudes, ω is the instantaneous angular frequency, $\delta_x(t), \delta_y(t)$ are the instantaneous phases of $E_x(t)$ and $E_y(t)$ respectively. The time variations of $E_1(t), E_2(t), \delta_x(t)$ and $\delta_y(t)$ are very slow compared to that of the mean frequency, ν ($\omega = 2\pi\nu$) which is of the order of the bandwidth $\Delta\nu$. Eliminating ωt term explicitly between equations 2.8a and 2.8b we get similar expression in equation 2.7:

$$\frac{E_x^2(t)}{E_1^2(t)} - 2\frac{E_x(t)E_y(t)}{E_1(t)E_2(t)} \cos \delta(t) + \frac{E_y^2(t)}{E_2^2(t)} = \sin^2 \delta(t) \quad (2.9)$$

where, $\delta(t) = \delta_y(t) - \delta_x(t)$. Equation 2.9 reduces into equation 2.7 when monochromatic radiation is considered, making E_x and E_y to be implicitly time dependent.

In order to measure the intensity of a radio wave, one takes the average per the time of observation . To do this, assume the time taken to be infinite because of a long period of time as relatively compared to the time for a single oscillation. The time average for equation 2.9 is therefore represented as;

$$\frac{\langle E_x^2(t) \rangle}{E_1^2} - 2 \frac{\langle E_x(t)E_y(t) \rangle}{E_1 E_2} \cos \delta + \frac{\langle E_y^2(t) \rangle}{E_2^2} = \sin^2 \delta \quad (2.10)$$

where, the symbol $\langle \rangle$ denotes the time average and

$$\langle E_i(t)E_j(t) \rangle = \lim_{T \rightarrow \infty} \int_0^T E_i(t)E_j(t)dt, \quad i, j = x, y \quad (2.11)$$

We multiply equation 2.10 by $4E_1^2E_2^2$ to get;

$$4E_2^2\langle E_x^2(t) \rangle - 8E_1E_2\langle E_x(t)E_y(t) \rangle \cos \delta + 4E_1^2\langle E_y^2(t) \rangle = (2E_1E_2 \sin \delta)^2 \quad (2.12)$$

and then use equation 2.11 to find the average terms in equation 2.10 to get;

$$\langle E_x^2(t) \rangle = \frac{1}{2}E_1^2 \quad (2.13a)$$

$$\langle E_y^2(t) \rangle = \frac{1}{2}E_2^2 \quad (2.13b)$$

$$\langle E_x(t)E_y(t) \rangle = \frac{1}{2}E_1E_2 \cos \delta \quad (2.13c)$$

Substituting equations 2.13a, 2.13b and 2.13c into equation 2.12, we get;

$$2E_1^2E_2^2 - (2E_1E_2 \cos \delta)^2 + 2E_1^2E_2^2 = (2E_1E_2 \sin \delta)^2 \quad (2.14)$$

Representing equation 2.14 in perfect square form, we add and subtract $E_1^4 + E_2^4$ to get;

$$(E_1^2 + E_2^2)^2 - (2E_1E_2 \cos \delta)^2 - (E_1^2 - E_2^2)^2 = (2E_1E_2 \sin \delta)^2 \quad (2.15)$$

We can deduce the intensities from equation 2.15:

$$S_0 = E_1^2 + E_2^2 \quad (2.16a)$$

$$S_1 = E_1^2 - E_2^2 \quad (2.16b)$$

$$S_2 = 2E_1E_2 \cos \delta \quad (2.16c)$$

$$S_3 = 2E_1E_2 \sin \delta \quad (2.16d)$$

Equation 2.16 is then expressed as;

$$S_0^2 = S_1^2 + S_2^2 + S_3^2 \quad (2.17)$$

Equations 2.16a, 2.16b, 2.16c and 2.16d represent the Stokes polarisation parameters for a plane wave. These parameters are real quantities with S_0 being the total intensity. The parameter S_1 characterizes the linear horizontal or vertical polarisation, that of S_2 characterizes the amount of linear $\pm 45^\circ$ polarisation and S_3 represents the amount of right or left circular polarisation contained within the beam. These parameters can be used to determine the degree of polarisation P_{deg} , for a given state of polarisation:

$$P_{deg} = \frac{I_{pol}}{I_{tot}} = \frac{(S_1^2 + S_2^2 + S_3^2)^{1/2}}{S_0}, \quad 0 \leq P_{deg} \leq 1 \quad (2.18)$$

where, I_{pol} is the intensity of the sum of the polarization components and I_{tot} is the total intensity of the signal. $P_{deg} = 1$ relates to completely polarised light, $P_{deg} = 0$ relates to unpolarised light and $0 < P_{deg} < 1$ relates to partially polarised light.

The Stokes parameters can also be obtained by ignoring the time average approach and express equations 2.8a and 2.8b in terms of complex amplitudes:

$$E_x(t) = E_1 \exp\{i(\omega t + \delta_x)\} = E_x \exp\{i\omega t\} \quad (2.19a)$$

$$E_y(t) = E_2 \exp\{i(\omega t + \delta_y)\} = E_y \exp\{i\omega t\} \quad (2.19b)$$

where, $E_x = E_1 \exp\{i\delta_x\}$ and $E_y = E_2 \exp\{i\delta_y\}$ are the complex amplitudes. The Stokes polarisation parameters from these complex amplitudes are:

$$S_0 = E_x E_x^* + E_y E_y^* \quad (2.20a)$$

$$S_1 = E_x E_x^* - E_y E_y^* \quad (2.20b)$$

$$S_2 = E_x E_y^* + E_y E_x^* \quad (2.20c)$$

$$S_3 = i(E_x E_y^* - E_y E_x^*) \quad (2.20d)$$

Substituting equations 2.19a and 2.19b into equation 2.20, we reproduce the expression in equation 4.36.

The Stokes parameters give a full characterization of any polarisation state of a plane wave. In chapter four, we discuss further on how to formulate the Stokes parameters in terms of column matrix to obtain not only measurable intensities but also observables too.

For a more general discussion on wave polarisation see (Born and Wolf 1965; Kraus 1966; Wood 1988; Shurcliff 1962; Goldstein 2003).

In short, an EM wave received by an antenna consists of both electric and magnetic fields. If we are to track the curve traced by the tip of the electric field vector, in some fixed location in space, we will get, as time varies, a curve referred to as the polarization ellipse . Also,

for a specified location we would generally get different curves, that is to say, the antenna polarization is dependent upon the direction of observation.

2.4 Antenna Arrays

An *antenna array* is a combination of 2 or more spatially separated antennas used to measure or direct the radiation intensity of a source towards a desired angular sector in order to have an improved performance over that of a single antenna. A very relevant characteristic of an array is that, the radiation pattern can be changed when we electronically steer or scan the antenna elements towards some other direction by changing their relative amplitudes and phases. This phenomenon does not occur when we use just a single antenna whose radiation pattern remain fixed. The use of an array for an observation gives us the opportunity to impose a particular desired array pattern without changing its physical dimensions. Furthermore, by manipulating the received signals from the individual antenna elements in different ways, we can achieve many signal processing functions such as spatial filtering (Armstrong, Zarb Adami, and Jones 2009; Leshem and van der Veen 2000; Wijnholds and van der Veen 2008), interference suppression (Ben-David and Leshem 2008; Levanda and Leshem 2010a; Mitchell and Robertson 2005), gain enhancement (Yatawatta 2008), target tracking (Woodburn et al. 2015; Duev et al. 2015), etc.

2.4.1 Mathematical Formulation of Antenna Array

Consider N antenna elements with corresponding $\bar{g}_k(\theta, \phi) |_{k=1,2,3,\dots,N}$ pattern of the k^{th} antenna. We take the elevation angle to vary over $-90^\circ \leq \theta \leq 90^\circ$ and that of the azimuthal angle to vary over $-180^\circ \leq \phi \leq 180^\circ$. Then, the overall output pattern $\bar{g}(\theta, \phi)$ is defined as:

$$\bar{g}(\theta, \phi) = \sum_{n=1}^N w_n \bar{g}_n(\theta, \phi) \exp\{i\xi\psi_n(\theta, \phi)\} \quad (2.21)$$

where, the element location is $\psi_n = x_n \sin \theta \cos \phi + y_n \sin \theta \sin \phi + z_n \cos \theta$, $\xi = \frac{2\pi}{\lambda}$ is the wavenumber, $w_n |_{n=1,2,3,\dots,N}$ are the elements complex weights.

If the antenna elements are identical, equation 2.21 becomes;

$$\bar{g}(\theta, \phi) = \bar{g}_1(\theta, \phi) \sum_{n=1}^N w_n \exp\{i\xi\psi_n(\theta, \phi)\} \quad (2.22)$$

where, $\bar{g}_1(\theta, \phi)$ is the element factor and $\sum_{n=1}^N w_n \exp\{i\xi\psi_n(\theta, \phi)\}$ is the array factor (AF). Equation 2.22 characterizes the *array pattern multiplication*.

Assuming we place N antenna elements uniformly linear on a particular axis with uniform spacing $n\Delta|_{n=0,1,2,3,\dots,N-1}$, then;

$$AF = \sum_{n=0}^{N-1} w_n \exp\{i\xi n\Delta \cos \theta\} \quad (2.23)$$

where, $w_n = \exp\{-i\xi n\Delta \cos \theta_0\} = (\exp\{i\gamma\})^n$.

From the geometrical progression theory, we can recall:

$$\sum_{n=0}^{\infty} \alpha^n = \frac{1}{1-\alpha}, \alpha \neq 1 \text{ and } \sum_{n=0}^{N-1} \alpha^n = \frac{1-\alpha^N}{1-\alpha}, \alpha \neq 1.$$

Applying these two theories to equation 2.23 and letting $\gamma = \xi\Delta(\cos \theta - \cos \theta_0)$, we get;

$$AF = \frac{1 - \exp\{iN\gamma\}}{1 - \exp\{i\gamma\}} \quad (2.24a)$$

$$= \frac{\exp\{iN\gamma/2\} \exp\{iN\gamma/2\} - \exp\{-iN\gamma/2\}}{\exp\{i\gamma/2\} \exp\{i\gamma/2\} - \exp\{-i\gamma/2\}} \quad (2.24b)$$

$$= \exp\{i(N-1)\gamma/2\} \frac{\sin(N\gamma/2)}{\sin(\gamma/2)} \quad (2.24c)$$

$$= \exp\{i(N-1)\xi\Delta/2(\cos \theta - \cos \theta_0)\} \frac{\sin\{\xi N(\Delta/2)(\cos \theta - \cos \theta_0)\}}{\sin\{\xi(\Delta/2)(\cos \theta - \cos \theta_0)\}} \quad (2.24d)$$

Since, $\frac{\sin(Nx)}{\sin(x)}$ behaves like $N \operatorname{sinc}(x)$, the maximum value of equation 2.24 occurs when $\theta = \theta_0$. Therefore, normalizing the centre array at $z = 0$, we get:

$$AF = \frac{1}{N} \frac{\sin\{\xi N(\Delta/2)(\cos \theta - \cos \theta_0)\}}{\sin\{\xi(\Delta/2)(\cos \theta - \cos \theta_0)\}} \quad (2.25)$$

2.4.2 Beamforming

The combination of multiple signals with different complex weights from different receiving antenna elements form a new radiation pattern. This technique is known as *beamforming* and can be done in analogue component such as LOFAR with high-band antennas (HBA) or after the signal is digitized, such as in the LOFAR stations. The algorithms used to generate the technique can be classified into *coherent*, *incoherent* and multi-pixel beamformer methods. The application of coherent beamforming allows a narrow beam to be formed and therefore, provides a higher gain which is very useful for example, during pulsar observation. Coherent beamforming increases the sensitivity in narrow FoV. Unlike coherent beamforming, incoherent beamforming does not affect FoV but increases the overall sensitivity. This kind of algorithm is very useful when searching for rare events where the location of occurrence is not known. The application of a multi-pixel beamformer such as the Giant Metre wave Radio Telescope (GMRT)¹) combines the enhanced sensitivity of a coherent array beamformer with the wide FoV seen by an incoherent array beamformer. This algorithm is implemented using the recorded base-band data as in (Roy, Bhattacharyya, and Gupta 2012) making it possible

¹<http://gmrt.ncra.tifr.res.in/>

to form sixteen directed beams in real-time. The multi-pixel beamformer can be used to improve the capabilities of studying pulsars.

2.4.3 Types of Radio Arrays

In this subsection, we discuss the main types of antenna receiving elements that can be used for radio interferometric observations. The advantages and disadvantages are also discussed.

2.4.3.1 Phased-Array Feeds

Generally, a single dish has one pixel and only records the total power captured within its primary beam at any given time. We can produce an image by pointing the single beam at different directions and then project the output on a sky grid. A feed design for a dish which incorporates multiple feeds instead of the single “pixel” feed is known as a *phased-array feed* (PAF). This new technology in radio astronomy is same as having several arrays pointing at different places simultaneously. Its feed horn is electrically large and collects nearly all focused signal energy. Imaging with an array of multi-beam antennas gives a good resolution and increase in FoV. This increase in FoV comes at a cost of each receiving element requiring its own isolated analogue front-end and digital back-end, making the feed more expensive. This is a new technology undergoing development and currently, PAFs have a higher system temperature and more limited analogue bandwidth compared to a single pixel feed. Additionally, the calibration of PAFs are a new challenge, and the software and techniques are in an ongoing state of development. Some of the PAF-based arrays are the Aperture Tile In Focus (APERTIF) project upgrade for Westerbork Synthesis Radio Telescope (WSRT) as in Fig. 2.6 and reproduced from (Garrett 2012), Australian Square Kilometre Array Pathfinder (ASKAP²) also displayed in Fig. 2.6, GBT.



Figure 2.6: Wide gain in FoV enabled by PAFs. Right-centre: APERTIF installed at the focus of a WSRT telescope. Extreme right: PAFs installed on ASKAP (courtesy CSIRO).

2.4.3.2 Transiting Arrays

Unlike a dish that can track a particular point in the sky over many hours, a transiting array has elements with limited mobility and allows the sky to drift through the primary beam of

²<http://www.atnf.csiro.au/projects/askap/index.html>

the elements. Its feed has an effective primary beam which is large compared to that of a dish. As a source enters into the beam, it starts with a small apparent flux, then gradually increases until the source peaks at the zenith. It then decreases as it moves across the beam side lobes until it finally sets at the horizon. Some of the transiting Arrays are Precision Array for Probing the Epoch of Reionization (PAPER), Long Wavelength Array (LWA), Medicina Northern Cross and the Murchison Widefield Array (MWA³) as shown Fig. 2.7. There are obvious cost advantages to building an array with no moving parts. Such arrays have wide FoV and can have the individual elements placed close together. This allows for large-scale structure experiments such as Epoch of Reionization (EoR) and BAO studies. The disadvantages compared to dishes create a new challenge for calibration and imaging. The individual elements are less sensitive compared to a dish, so more elements are needed, which requires larger correlator systems. Also, as the sky transits, the apparent flux of sources changes, so the primary beam must be well known in order to get back to the intrinsic flux of the sky. Depending on the scale of the primary beam, a transiting array has set amount of time per day in which a section of the sky can be observed. This means that, a deep integration of a region of sky is not possible without observing for many days.



Figure 2.7: Transiting Arrays:- PAPER (top-left), LWA (bottom-left), Medicina Northern Cross (top-right) and MWA (bottom-right).

2.4.3.3 Aperture Arrays

We can convert a transiting array into a digital dish to form an *aperture array*. This makes it possible to point the digital dish in many directions of the sky simultaneously. The idea with an aperture array is that by updating the beamforming weights, the beam of the aperture array can track a region of the sky. The aperture array takes advantages from both dishes and

³<http://www.mwatelescope.org/>

transiting arrays. The main cost is the analogue and digital electronics to build such an array. For this reason, aperture arrays are mainly used for low-frequency science, such as LOFAR as in Fig. 2.8 and the future SKA-LOW shown in Fig. 2.9, as the Dense Aperture Array (DAA) components are cheaper. With improved technology, the price of higher frequency components will make it possible to increase the observable frequency. A second issue with aperture arrays is that the primary beam changes depending on pointing location and frequency. As the beam is a weighted sum of all the individual elements there is limited precision to the beam shape. There is a design difference of sparse and dense aperture arrays. When the elements of the aperture array are placed closer than $\lambda/2$ observing wavelength the array is *dense*. The array is fully sampling the wavefront and there are no beam artefacts such as *grating lobes* (a type of side lobe) which introduces significant structure into the beam. If the elements are further apart than $\lambda/2$ then these side lobes structures appear and limit the sensitivity and FoV. For a single observing frequency, designing an aperture array is simple as all the elements are spaced at $\lambda/2$. But, for wide-band arrays, if the elements are placed at $\lambda_i/2$ for a wavelength λ_i , then for any wavelength $< \lambda_i$ the array configuration under-samples that observing wavelength and introduces large grating lobes. Therefore, a balance between observing bandwidth, cost and dense versus sparse trade-off must be made during the array design.



Figure 2.8: Aperture Array:- LOFAR.



Figure 2.9: SKA-2 Dense Aperture Arrays precursor telescope.

A more detailed discussions on radio arrays can be seen in (Foster 2015; Garrett 2012).

2.5 Power received from radio sources in the sky

The receivers of a radio telescope are very sensitive to the orientation state of the incoming radiation. More generally, in radio astronomy, two receivers are attached to each receiving feedhorn, with a splitter feeding horizontally polarised radiation to one receiver and vertically polarised radiation to the other. The sum of what is obtained in each polarisation is known as the *total intensity*. In each polarisation, the power P_w received per unit bandwidth from an element of solid angle of the sky is defined as equation (2.26);

$$P_w = \frac{1}{2} A_e \iint_{\Omega} B_s(\theta, \phi) P_n(\theta, \phi) d\Omega \quad (2.26)$$

where A_e = effective aperture (collecting area) of antenna [m^{-2}],
 $B_s(\theta, \phi)$ = brightness distribution of radio emission across the sky [$\text{W m}^{-2} \text{Hz}^{-1} \text{sr}^{-1}$],
 $P_n(\theta, \phi)$ = normalised power (beam) pattern of the antenna,
 $d\Omega = \sin \theta d\theta d\phi$, element of solid angle [sr].

In radio astronomy, what we are mostly interested in is the integral of the brightness over a radio source say S . This notation S is known as the *flux density* and it is expressed as equation (2.27);

$$S = \iint_{\text{source}} B_s(\theta, \phi) d\Omega \quad (2.27)$$

Consider the radio source is observed with a radio telescope with the power pattern $P_n(\theta, \phi)$, then, the observed flux density is computed by the product of the integral of the brightness distribution and the antenna beam pattern:

$$S_0 = \iint_{\text{source}} B_s(\theta, \phi) P_n(\theta, \phi) d\Omega \quad (2.28)$$

In equation (2.28), if the radio source is relatively smaller than the beam and it is in the centre of the beam, then, $P_n(\theta, \phi) \approx 1$. But if the source is extended with simple geometry, then simple analytic function will enable S_0 to be corrected and this is discussed in the Gaylard 2012 technical report.

The SI unit of flux density is usually expressed in $\text{W m}^{-2} \text{Hz}^{-1}$. However, the radio emission is not very strong as the radio emitters are very far away, and the unit known as the Jansky [Jy], after the radio astronomy pioneer Karl Jansky, was adopted in 1973. It is defined as $10^{-26} \text{W m}^{-2} \text{Hz}^{-1}$.

2.6 Aperture Synthesis Technique

2.6.1 Construction of Radio Images

Radio telescopes are used to measure the flux density of an observed radio source by integrating the intensity over the telescope beam. Intensity image of the observed source is then produced from the data obtained from the radio telescopes.

Fig. 2.10(a) as in (Joardar et al. 2010) displays a single dish radio telescope steering at a distant radio source with parallel rays illuminating the dish aperture. Consider that the aperture plane is located at the origin of a rectangular coordinate system (u, v, w) with w pointing directly at the source as in Fig. 2.10(b) and the u and v axes point east and north in the (u, v) plane normal to the w axis. Also, on the sky, consider the electric field distribution to be centered on different coordinate system (l, m) . These (l, m) are the direction cosines projected onto the (u, v) plane. The electric field distribution $\varepsilon(u, v)$ on the u, v plane is defined in terms of the electric field distribution of $V(l, m)$ on the sky. Considering that we have full information about $\varepsilon(u, v)$, we can then find the auto-correlation of each of the electric field points on the u, v plane to get $W(u, v)$. The intensity field distribution $I(l, m)$ of the source is measured when we find the Fourier transform on $W(u, v)$. Realistically $\varepsilon(u, v)$ is not achievable, since the antenna produces a single output. This single output is very significant as it shows a basic relation between intensity map of radio source on the sky with the aperture illumination.

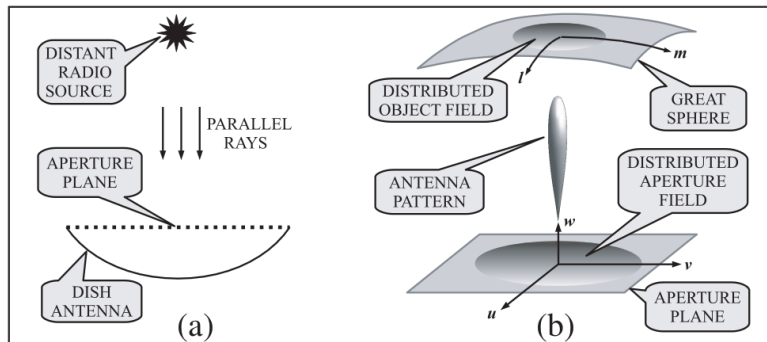


Figure 2.10: (a) A distant radio astronomical source illuminates a dish antenna with parallel rays. (b) Electric field distributions of a source on the great sphere and antenna aperture on the aperture plane

Although single dish radio telescopes like the 100 m GBT and the huge but fixed 305 m Arecibo Observatory are very advantageous in making primary surveys of the sky at low resolution, the resolution of a telescope is limited by its collecting area (Wright 2004; Emerson 2002). Interferometry is a technique for connecting multiple radio antennas to efficiently form single antenna with a far greater collecting area than the individual components. The separation between the antennas and the rotation of the Earth leads to differences in the observed path length from the object under observation. When the data from each of the

antennas is put together, an interference pattern is generated, which can be reconstructed to form an image of the observation. Instead of a single dish antenna, an interferometer with the assistance of the rotation of Earth can synthesize a large antenna aperture. This technique is known as *super-synthesis* (Machin, Ryle, and Vonberg 1952; Thompson and Bracewell 1974).

Consider a large number of radio telescopes distributed across a plane area situated at a given longitude, latitude and altitude as shown in Fig. 2.11(a) such that they track a distant radio source located on the celestial North pole. Consider also a rectangular coordinate system (u', v', w') whose origin is at the phase center of telescope plane as in Fig. 2.11(b) reproduced from (Joardar et al. 2010) such that w' axis points towards the zenith (source) and the u', v' plane remains stationary to the observed source. From the observed source towards the antennas, due to the rotation of the Earth, the position of the antennas appears to be moving over the u', v' plane. The outputs of individual radio telescopes is recorded at each integration time and then placed on the u', v' plane.

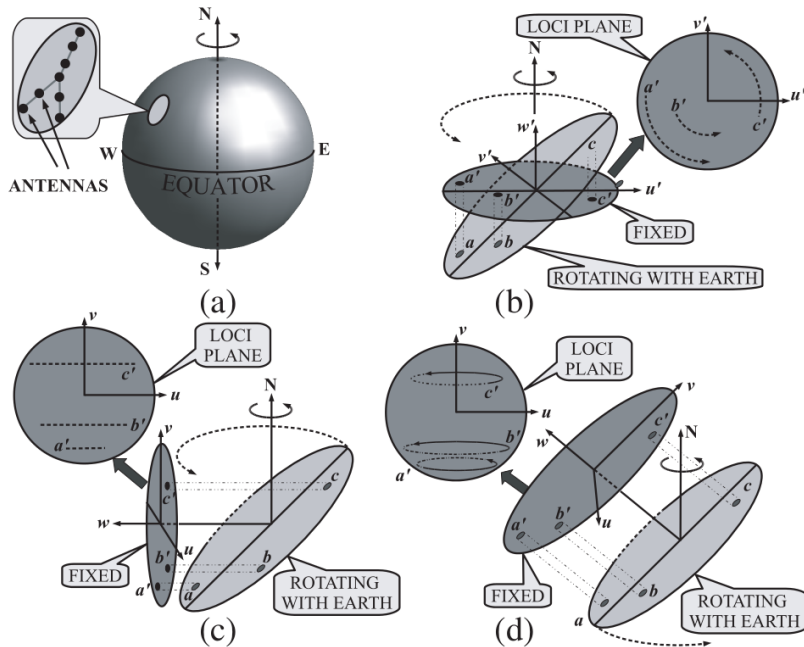


Figure 2.11: The principle of super synthesis. (a) An interferometer rotates with the Earth rotation (b) Observing a radio source towards celestial North Pole. (c) Observing a radio source along the celestial equator. (d) Observing a radio source along a celestial latitude in between.

The loci a' , b' and c' of the radio telescopes a , b and c respectively on the u', v' plane forms circles over a period of 24 h. Having numerous radio telescopes at different baselines from the origin of the (u', v', w') coordinates over a period of 24 h, the u', v' plane gets highly populated. The u', v' plane then forms the aperture of a large synthesized antenna. Thus, we apply Fourier transform on the u', v' plane data after calibration to obtain the field distribution of the source. Considering a radio source on the celestial equator as presented in Fig. 2.11(c), the loci a' , b' and c' on the u', v' plane form straight lines. Thus, if all the radio telescopes are mounted on a single East-West line then their respective loci be a straight line and this

not good enough for making a radio image. It is therefore necessary to mount some of the radio telescopes spread along the North-South axis. If the observed source is located at a celestial latitude between $(0^\circ, 90^\circ)$ or $(-90^\circ, 0^\circ)$, each of the loci form an ellipse as shown in Fig. 2.11(d).

2.6.2 Correlator Super-synthesis Arrays

The correlation products between any pair of antennas are used to fill the u, v plane, where the (u, v, w) coordinates are measured in wavelengths. If there are N antennas in an array, then the number of cross correlation is defined as $N \left(\frac{N-1}{2} \right)$. In any pair of antennas in an interferometer, when we fix one of the antennas at the origin of the (u, v, w) , the baseline between the two antennas on the u, v plane will rotate through 180° in 12 h. We obtain similar observation results when the other antenna is considered as the origin of the (u, v, w) coordinates. This makes it possible to cover 360° of baseline rotation in half a day. Thus, data obtained from an interferometer is a measure of the spatial coherence function called *visibility* and is denoted as $V(u, v)$. This visibility data cover only 1/2 of the u, v plane from a 12 h observation, but the other 1/2 can be obtained using equation 2.29, where $V^*(u, v)$ is the complex conjugate of $V(u, v)$. Hence, we can derive 24 h of observed data from a 12 h observation.

$$V(-u, -v) = V^*(u, v) \quad (2.29)$$

2.6.3 The Van Cittert-Zernike Equation

Consider a 2 element interferometer observing a radio source as in Fig. 2.12(a) (Joardar et al. 2010) such that the first element is positioned at the origin of the (u, v, w) coordinate system. Also, consider $I(l, m)$ to be the intensity distribution of the source on the celestial sphere such that the origin of the l, m coordinate system is at the phase reference position. If we denote $I(\bar{s})$ as the sky brightness at a frequency ν in the direction \bar{s} and assume $A(\bar{s})$ to be the effective aperture area of an antenna in the same direction, then the signal power received over a bandwidth $\Delta\nu$ within a solid angular element $d\Omega$ for each antenna is given by $A(\bar{s})I(\bar{s})\Delta\nu d\Omega \cos(2\pi\nu\tau_g)$. Therefore, the correlated signal power dr over $d\Omega$ is given as;

$$dr = A(\bar{s})I(\bar{s})\Delta\nu d\Omega \cos(2\pi\nu\tau_g) \quad (2.30)$$

Integrating equation 2.30 over the celestial sphere we get the correlator power r :

$$r(\vec{d}_\lambda, \bar{s}) = \Delta\nu \int A(\bar{s})I(\bar{s}) \cos[2\pi(\vec{d}_\lambda \cdot \bar{s})] d\Omega \quad (2.31)$$

where, \vec{d}_λ is the baseline vector specified by the (u, v, w) coordinates and measured in wavelengths.

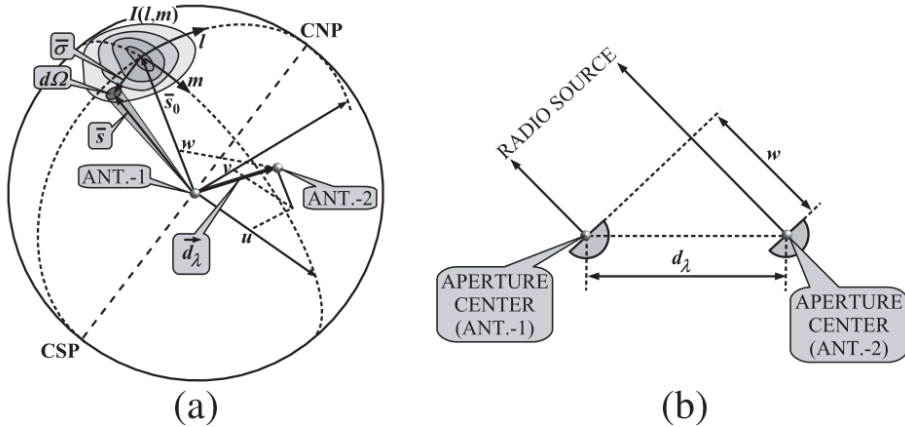


Figure 2.12: Geometry of a radio source and a simple interferometer. (a) An observed radio source with intensity distribution $I(l, m)$ using a simple two element radio interferometer. (b) Lower the elevation angle of the radio source the larger the value of w .

If we put $\bar{s} = \bar{\sigma} + \bar{s}_0$ such that $\bar{\sigma}$ is the position vector from the phase reference point to the observing point. Rewriting equation 2.31 we get;

$$\begin{aligned} r(\vec{d}_\lambda, \bar{s}_0) &= \Delta\nu \cos[2\pi(\vec{d}_\lambda \bar{s}_0)] \int A(\bar{\sigma}) I(\bar{\sigma}) \cos[2\pi(\vec{d}_\lambda \bar{\sigma})] d\Omega \\ &\quad - \Delta\nu \sin[2\pi(\vec{d}_\lambda \bar{s}_0)] \int A(\bar{\sigma}) I(\bar{\sigma}) \sin[2\pi(\vec{d}_\lambda \bar{\sigma})] d\Omega \end{aligned} \quad (2.32)$$

The visibility V is defined as a complex function:

$$V = |V| \exp(j\phi_\nu) = \int A'(\bar{\sigma}) I(\bar{\sigma}) \exp(-j2\pi \vec{d}_\lambda \bar{\sigma}) d\Omega \quad (2.33)$$

with the real part being;

$$V = |V| \cos(\phi_\nu) = \int A'(\bar{\sigma}) I(\bar{\sigma}) \cos(2\pi \vec{d}_\lambda \bar{\sigma}) d\Omega \quad (2.34)$$

and the imaginary part being;

$$V = |V| \sin(\phi_\nu) = - \int A'(\bar{\sigma}) I(\bar{\sigma}) \sin(2\pi \vec{d}_\lambda \bar{\sigma}) d\Omega \quad (2.35)$$

where, $A'(\bar{\sigma}) = \frac{A(\bar{\sigma})}{A_0}$ is the normalized beam pattern of an antenna with A_0 being the peak antenna gain.

Substituting equation 2.34 into 2.33, we get;

$$r(\vec{d}_\lambda, \bar{s}_0) = A_0 \Delta\nu |V| \cos[2\pi(\vec{d}_\lambda \bar{\sigma} - \phi_\nu)] \quad (2.36)$$

Equation 2.36 shows that an interferometer measures the visibility which is a measure of the wavefront's spatial coherence across the baseline.

To produce an image from equation 2.36, we need to know their positions on the u, v, w coordinate system and compare them with l, m coordinate system. As the elevation angle of the observed source decreases as in Fig. 2.12(b), the w term increases:

$$\vec{d}_\lambda \bar{s} = ul + vm + wn \quad (2.37)$$

If $\bar{s} = \bar{s}_0$ equation 2.37 simplifies to;

$$\vec{d}_\lambda \bar{s} = w \quad (2.38)$$

The solid angle $d\Omega$ can be expressed in polar coordinates as $d\Omega = \sin \theta d\theta d\phi$, where θ and ϕ are the polar and azimuthal angles in the (u, v, w) plane, that is, $\theta = \sin^{-1}(\sqrt{l^2 + m^2})$ and $\phi = \tan^{-1}(m/l)$. Using the Jacobian method, we can transform the coordinates (θ, ϕ) into (l, m) :

$$d\Omega = \frac{dl dm}{n} = \frac{dl dm}{\sqrt{1 - l^2 - m^2}} \quad (2.39)$$

Using equations 2.37 to 2.39, we can therefore rewrite the visibility V in equation 2.37 in terms of u, v, w :

$$V(u, v, w) = \int_{-\infty}^{\infty} \int_{-\infty}^{\infty} \frac{A'(l, m)I(l, m)}{\sqrt{1 - l^2 - m^2}} \exp\{-j2\pi[ul + vm + w(\sqrt{1 - l^2 - m^2} - 1)]\} dl dm \quad (2.40)$$

Equation 2.40 is known as *van Cittert-Zernike equation* (Thompson, Moran, and Swenson 2001; Thompson and Bracewell 1974; Rau et al. 2009) and it shows that the visibility $V(u, v, w)$, is a Fourier transform of the product of the sky brightness $I(l, m)$, the primary beam response $A'(l, m)$ and $1/\sqrt{1 - l^2 - m^2}$.

When the distance of the observed source becomes less, $|l|$ and $|m|$ become very less such that $w(\sqrt{1 - l^2 - m^2} - 1)$ approaches zero and equation 2.40 reduces to;

$$V(u, v, w) \approx V(u, v, 0) = \int_{-\infty}^{\infty} \int_{-\infty}^{\infty} \frac{A'(l, m)I(l, m)}{\sqrt{1 - l^2 - m^2}} \exp\{-j2\pi(ul + vm)\} dl dm \quad (2.41)$$

and the inverse transform being defined by;

$$\frac{A'(l, m)I(l, m)}{\sqrt{1 - l^2 - m^2}} = \int_{-\infty}^{\infty} \int_{-\infty}^{\infty} V(u, v) \exp(j2\pi(ul + vm)) du dv \quad (2.42)$$

2.6.4 Filling the u,v Plane with Visibilities

Consider the phase reference position of an observed radio source is at (H_0, δ_0) in the local equatorial coordinate system. Assume X_λ, Y_λ and Z_λ are the baseline components in a rectangular coordinate system measured in wavelengths (Thompson, Moran, and Swenson 2001), then the u, v can be written as;

$$u^2 + \left[\frac{v - Z_\lambda \cos(\delta_0)}{\sin(\delta_0)} \right]^2 = X_\lambda^2 + Y_\lambda^2 \quad (2.43)$$

Equation 2.43 represents an ellipse which splits into 2 in the u, v plane if $Z_\lambda \neq 0$ (Thompson, Moran, and Swenson 2001). Fig. 2.13(a) produced from (Joardar et al. 2010) displays equation 2.43 when observing a radio source at declination δ_0). That for Fig. 2.13(b) displays cases of a North-South baseline for different values of δ_0 .

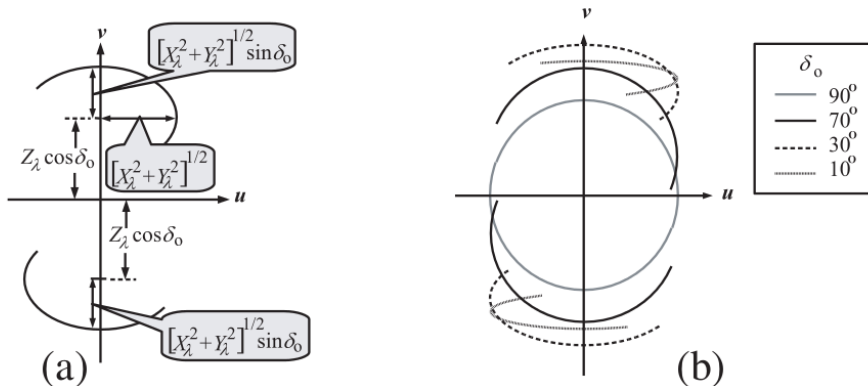


Figure 2.13: Locus on the u, v plane.. (a) Locus of the ellipse on u, v plane for a baseline with $Z_\lambda \neq 0$ observing a radio source at declination δ_0 . (b) Different declinations for different cases.

The KAT-7 consists of seven observing antennas located at latitude -30° , longitude 21° and altitude $1038m$ in configuration as shown in Fig. 2.14(a). Fig. 2.14(b) displays the u, v coverage at particular synthesis time with observed radio source at the phase centre. The circular structure rotates along with the Earth. If the zenith coincides with a celestial pole, then each point traces out a circle. Otherwise, the tracings could be elliptical, broken ellipse, or straight line (zero declination). When we increase the synthesis time, more data fill the u - v plane. Using equation 2.42, the intensity distribution $I(l, m)$ or image of the radio source is made. This is actually done after calibrating the data (Thompson, Moran, and Swenson 2001; Thompson and Bracewell 1974; Rau et al. 2009; Beardsley et al. 2016; Junkleowitz et al. 2016).

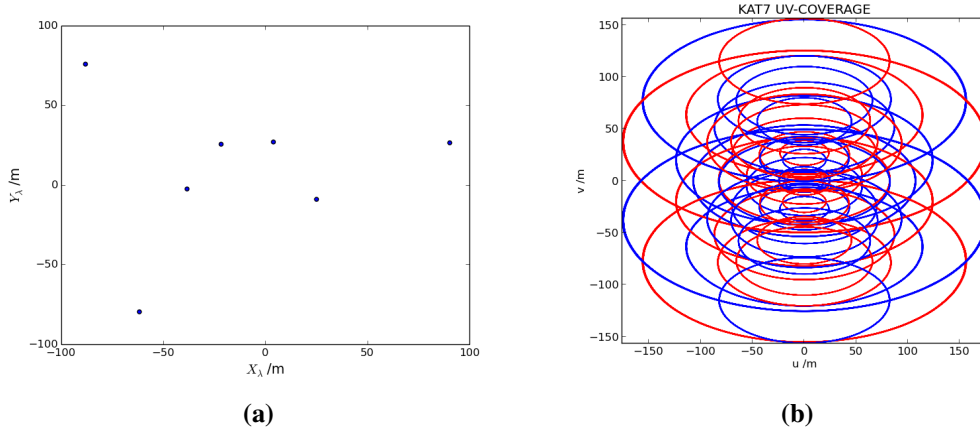


Figure 2.14: Filling the u - v plane with visibilities. (a) The KAT-7 configuration. (b) The u - v plane coverage of a 4h period of observation obtained from a source at the phase centre.

Using Fast Fourier Transform (FFT) approach, the data on u - v plane is interpolated on a uniform grid (Thompson, Moran, and Swenson 2001; Fu and Wu 2005; Zhang, Wu, and Sun 2007) and at the same time employ tapering technique (Thompson, Moran, and Swenson 2001) to reduce the side lobes of the synthesized antenna beam. The dirty image obtained after FFT may contain lots of artifacts (Desai et al. 2016). These are removed using algorithms such as CLEAN (Abrantes et al. 2009; Camps et al. 1998; Levanda and Leshem 2010b; Coughlan and Gabuzda 2012) or MEM (Coughlan and Gabuzda 2012; Junklewitz et al. 2016; Coughlan and Gabuzda 2013).

Chapter 3

Radio Foregrounds and Rotation Measure Synthesis

Overview

This chapter presents foreground simulation (i.e. diffuse synchrotron emission) targeted for the intensity mapping experiment that is set to study the redshifted 21 cm hyperfine line of neutral hydrogen and CO line. Also, Faraday rotation measure synthesis is discussed.

3.1 Introduction

The measurement of redshifted 21 cm emission is one of the most powerful tool to survey the large scale structure of the Universe from dark ages to present epoch (Furlanetto, Oh, and Briggs 2006). The emission emerging from different astrophysical sources, other than the HI signal, results in the foreground emission whose order of magnitude is 4 to 5 larger than the expected 21 cm signal (Ghosh et al. 2011). A detail study of the foreground components is required to extract the 21 cm signal.

3.2 Galactic Foreground

Numerous research studies (Wolz et al. 2014; Jelić et al. 2010; Santos et al. 2015; Alonso et al. 2015; Kiyotomo 2014) have clearly shown that synchrotron emission from the Galaxy dominates at low microwave frequencies $\lesssim 30$ GHz, whilst that of thermal dust emission is at higher frequencies $\lesssim 70$ GHz. Between these two components in frequency, lies the thermal free-free and non-thermal dust emissions, which are formed as a result of spinning dust grains as in Fig. 3.1. The subsections from 3.2.1 to ?? discuss briefly the components of

the Galactic foregrounds, paying particular attention to their contribution to the polarisation measurements.

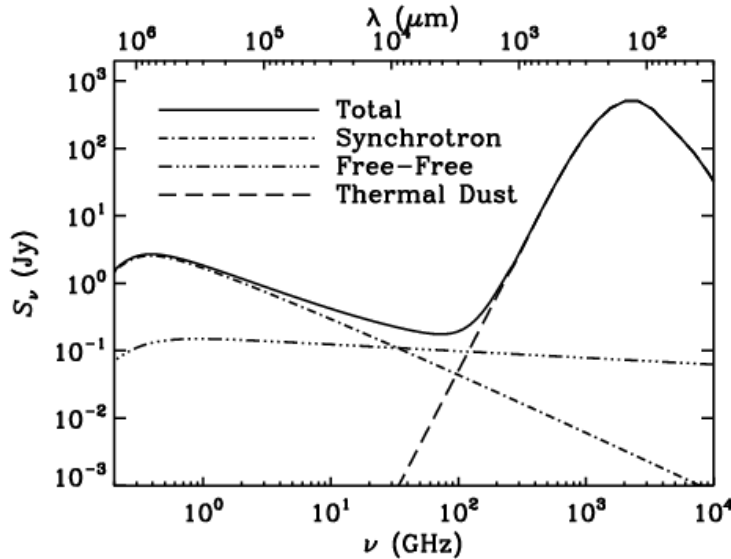


Figure 3.1: A model of radio galaxy spectrum (see Murphy 2011). The individual contributions from non-thermal synchrotron, free-free, and thermal dust emission are indicated by dot-dashed, triple dot-dashed, and dashed lines, respectively.

3.2.1 Diffuse Galactic Synchrotron Emission

A varying magnetic field can accelerate charge particles to emit radiation. The Diffuse Galactic Synchrotron Emission (DGSE) emerges from interactions between cosmic ray electrons and magnetic fields in the Galaxy. These interacting particles are accelerated to relativistic speeds in very high energetic environments, such as shock-waves from supernovae explosions. The synchrotron intensity and spectrum depend on the magnetic field strength and cosmic ray energy, showing significant spatial variations on the sky. The energy distribution of cosmic ray electrons follows a power-law such that $N(E) \propto E^{-\tau}$ where the energy $E > 10$ GeV (Adriani et al. 2011). The spectral index τ of the distribution is ≈ 3.0 and this is universally accepted when modelling in synchrotron and magnetic field.

The intensity of a synchrotron radiation S_{sync} , at a frequency ν is mathematically expressed as (Miville-Deschénes et al. 2008);

$$S_{sync}(\nu) = \epsilon_{sync}(\nu) \int_z n_e B_{\perp}^{(1+\tau)/2} dz \quad (3.1)$$

where equation 3.1 is integrated with respect to the sight-line z , n_e is cosmic ray density and $B_{\perp} = \sqrt{B_x^2 + B_y^2}$ is the x, y components of the magnetic field of the sky. From the power law

we can express the emissivity term $\varepsilon_{sync}(\nu)$ as;

$$\varepsilon_{sync}(\nu) = \varepsilon_0 \nu^{-(\tau-1)/2} \quad (3.2)$$

Recall Rayleigh-Jeans law at frequency ν :

$$B_\nu(T) = \frac{2\nu^2 k_B T}{c^2} \quad (3.3)$$

where, c is the speed of light, k_B is the Boltzmann constant and T is the temperature in Kelvin. Using equation 3.3, we can convert equation 3.1 into a brightness temperature T_{sync} at frequency ν :

$$T_{sync}(\nu) = \frac{c^2 S_{sync}(\nu)}{2k_B \nu^2} \quad (3.4)$$

Hence, the brightness temperature T_{sync} of synchrotron emission in a particular sight-line is expressed in power law at frequency ν :

$$T_{sync}(\nu) = T_{sync}(\nu_0) \left(\frac{\nu}{\nu_0} \right)^{\gamma_{sync}} \quad (3.5)$$

where, $\gamma_{sync} = -(\tau+3)/2$. The spectral index γ_{sync} , as discussed by (Navarro 2014) changes at different frequency bands as displayed in table 3.1.

Table 3.1: Measured Spectral Indices at Different Frequency Bands

γ_{sync}	Frequency Band (GHz)
-2.55	0.045 – 0.408
-2.71	0.408 – 2.30
-3.01	2.300 – 33.0

Fig. 3.2 is the 408 MHz full-sky survey taken from (Navarro 2014) and originally produced by (Haslam et al. 1982) displaying the sky in mollview form in Galactic coordinates at a frequency where the diffuse synchrotron emission is most dominant. A number of extragalactic sources are visible in the map, including the Cen A galaxy and the Magellanic clouds.

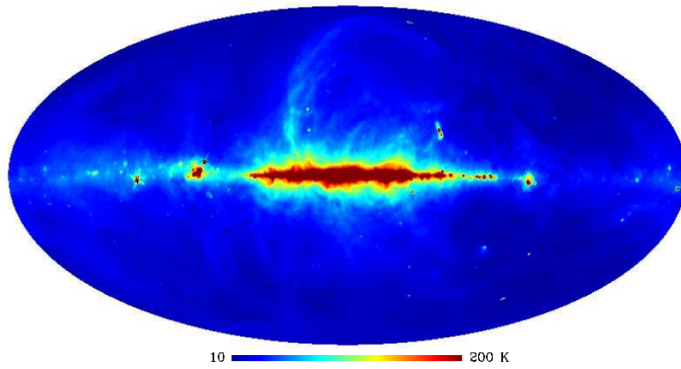


Figure 3.2: 408 MHz Full-Sky Map.

Synchrotron emissions are intrinsically linearly polarised since the cosmic ray electrons accelerated by the magnetic fields emit photons and are therefore polarized perpendicularly to the lines of field. Thus, the cosmic rays and magnetic field distributions of a galaxy can be used to predict the polarization foreground from synchrotron emission and remove it from observed maps. The degree of linear polarization integrated over all electron energy and frequency is defined as $l = (\tau + 1)/(\tau + 7/3)$. The polarisation factor (l) can be increased to 0.75 if the cosmic ray spectral index $\tau \approx 3$. We can express the polarised intensity in terms of Stokes parameters Q and U at frequency ν such that;

$$I(\nu) = \sqrt{Q(\nu)^2 + U(\nu)^2} \quad (3.6)$$

with the angle of polarisation to be:

$$\varphi(\nu) = \frac{1}{2} \arctan \left(\frac{U(\nu)}{Q(\nu)} \right) \quad (3.7)$$

From equation 3.1, we can mathematically express the Stokes parameters Q and U of polarised synchrotron emission integrated along the sight-line z as (Miville-Deschénes et al. 2008);

$$Q_{sync}(\nu) = l_{sync} \epsilon_{sync}(\nu) \int_z n_e B_{\perp}^{(1+\tau)/2} \cos(2\alpha) \sin(\beta) dz \quad (3.8)$$

and

$$U_{sync}(\nu) = l_{sync} \epsilon_{sync}(\nu) \int_z n_e B_{\perp}^{(1+\tau)/2} \sin(2\alpha) \sin(\beta) dz \quad (3.9)$$

where, $\cos(2\alpha) = \frac{B_x^2 - B_y^2}{B_{\perp}^2} \quad 0 < \cos(2\alpha) < 1$, $\sin(2\alpha) = -\frac{B_x^2 B_y^2}{B_{\perp}^2} \quad 0 < \sin(2\alpha) < 1$ and
 $\sin(\beta) = \sqrt{1 - \frac{B_x^2}{B_{\perp}^2}} \quad 0 < \sin(\beta) < 1$.

In this work, the scheme used to simulate the full-sky polarisation maps presented in Fig. 3.3 is fully described in Appendix D of Shaw et al. 2015, where they basically produce a large-scale base map by extrapolating the Haslam map (Loeb and Wyithe 2008) with a spectral index map from (Miville-Deschénes et al. 2008) and then randomly generate maps that add in fluctuations in frequency and on small angular scales. The smoothed synchrotron maps in Figs. 3.3 to 3.7 are presented by a sample of Hierarchical Equal Area isoLatitude Pixelation (HEALPix¹) (Górski et al. 2005) of the sphere at a resolution of $N_{side} = 512$. Other techniques for simulating full-sky radio emission are presented by de Oliveira-Costa et al. 2008; Geil, Gaensler, and Wyithe 2011; Jelić et al. 2008; The Polarbear Collaboration: P. A. R. Ade et al. 2014; Tucci et al. 2002. These simulated full-sky maps are convolved with the modelled beams discussed in Chapters 4, 5 and 6 to estimate the amount of foregrounds that have leaked from intensity to polarisation due to errors in the beams.

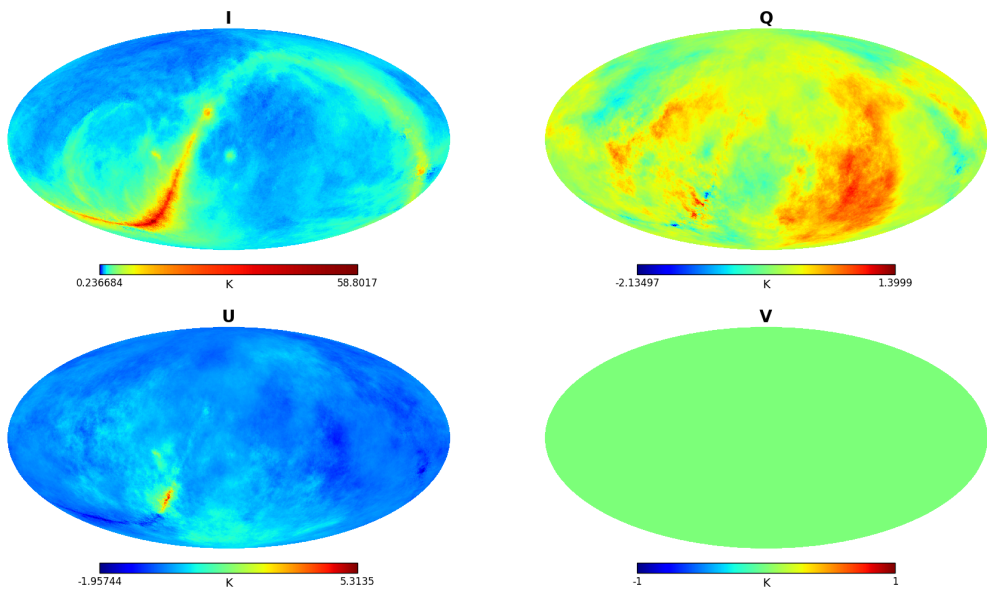


Figure 3.3: 1000 MHz full-sky synchrotron maps simulated by using m -mode formalism. These synchrotron maps characterize the full-sky polarisation maps for our low resolution simulated observations and are presented here in the mollweide projection form defined by equatorial coordinates in terms of Stokes parameters I, Q, U and V .

¹<http://healpix.sourceforge.net/>

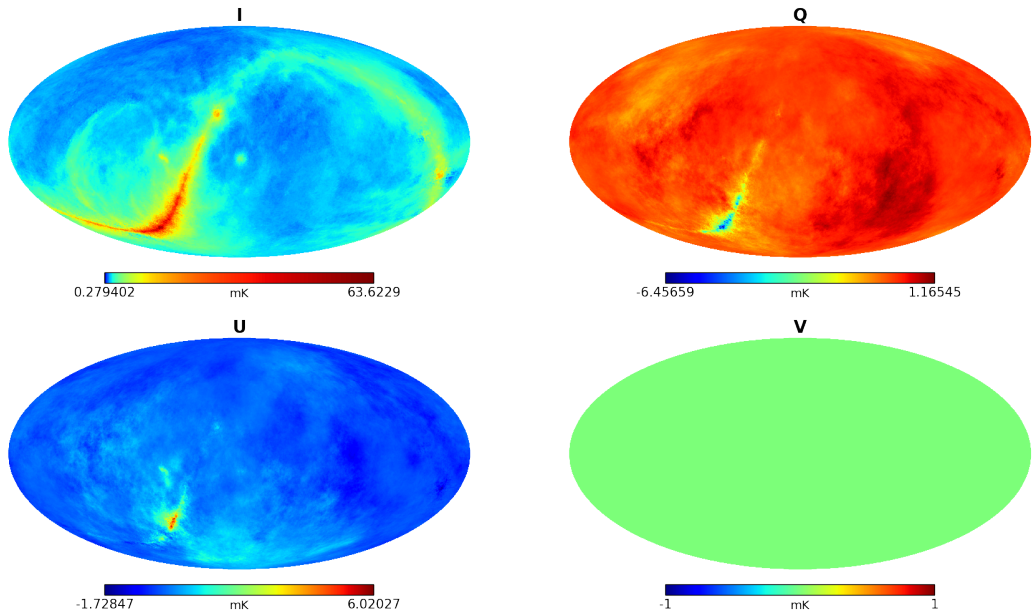


Figure 3.4: 950 MHz full-sky synchrotron maps simulated by using m -mode formalism.

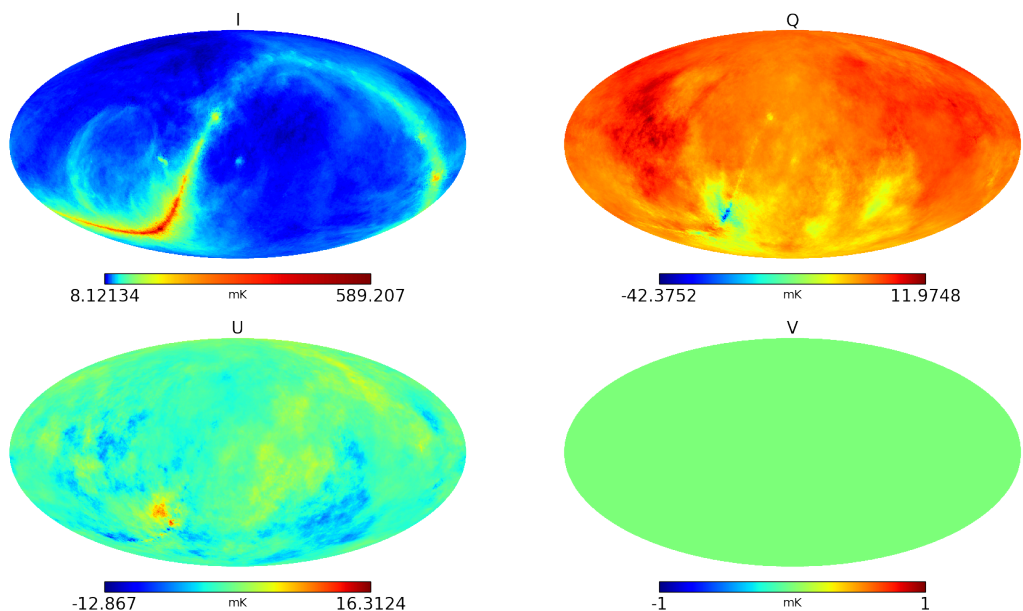


Figure 3.5: 450 MHz full-sky synchrotron maps simulated by using m -mode formalism.

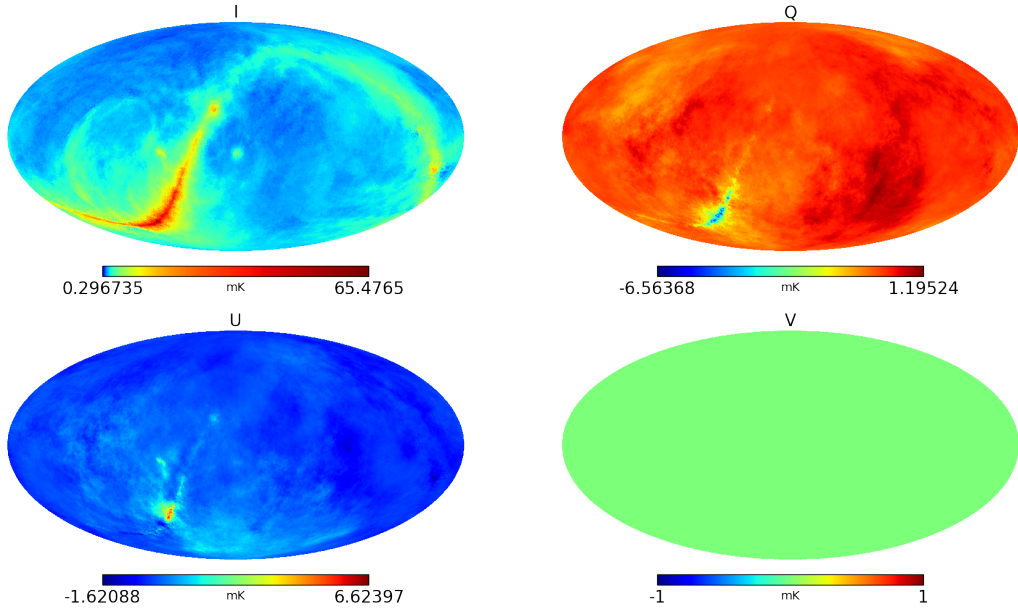


Figure 3.6: 990.5 MHz full-sky synchrotron maps simulated by using m -mode formalism.

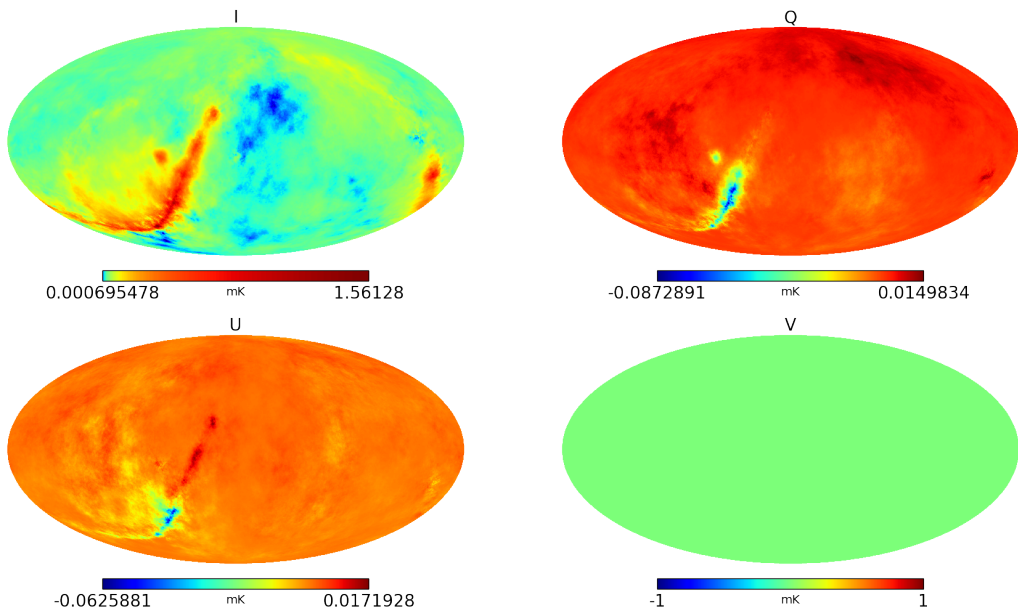


Figure 3.7: 4.6 GHz full-sky synchrotron maps simulated by using m -mode formalism.

3.3 Faraday Rotation Measure Synthesis

Polarisation is the term used to describe the orientation of the electric field in a light wave. Usually, light is not polarised when created but can be made so by transporting it through a medium which transmits electric fields oriented in a specific direction and absorbs all others. Radio emission from astronomical sources such as galactic and extra-galactic sources and

pulsars is often linearly polarised. Of course, other sources such as OH masers from galactic star formation due to Zeeman splitting are mostly circularly polarised (Acosta-Pulido et al. 2015, p. 146–152). Generally, polarisation in radio astronomy is related to the presence of magnetic fields. For instance, radio emission due to synchrotron radiation is linearly polarised with the electric vectors directed perpendicularly to the projection of the magnetic field in the emission regions onto the plane of the sky (Bell and Enßlin 2012; Brentjens and de Bruyn 2005). However, the direction of the polarisation may alter as the radio waves propagate through the ISM. This effect is called Faraday rotation and it allows radio astronomers to understand magnetic field along the line of sight in both the ISM and earth's ionosphere.

The polarisation angle of Faraday rotation is quantified in terms of its rotation measure (Φ_{RM}) and it is mathematically expressed as;

$$\chi(\lambda) = \chi_0 + \Phi_{RM} \cdot \lambda^2 \quad (3.10)$$

such that,

$$\Phi_{RM} = 0.81 \int_{source}^{observer} n_e \vec{B} \cdot d\vec{l} \quad (3.11)$$

where the polarisation angle measured at wavelength λ is $\chi(\lambda)$, χ_0 is the intrinsic polarisation, n_e is the electron density in cm^{-3} , B is the magnetic field in μG and l is the pathlength in pc. The dot product of the magnetic field and the pathlength (i.e. $\vec{B} \cdot d\vec{l}$) describe the projection of the field along the line of sight.

The observed complex polarisation is described by Burn 1966 as $P(\lambda^2) = pI \exp(2j\chi)$, where p is the degree of polarisation. Substituting equation 3.10 for χ in Burn 1966 equation and integrating over all possible values of the rotation measure to get;

$$P(\lambda^2) = \int_{-\infty}^{+\infty} pI \exp(2j[\chi_0 + \Phi_{RM} \cdot \lambda^2]) d\Phi_{RM} \quad (3.12a)$$

$$= \int_{-\infty}^{+\infty} F(\Phi_{RM}) \exp(2j\Phi_{RM} \cdot \lambda^2) d\Phi_{RM} \quad (3.12b)$$

where the intrinsic polarised flux is characterised by the *Faraday dispersion function* $F(\Phi_{RM})$ in terms of Faraday depth. Note how the expression in equation 3.12b takes the form of a Fourier transform. Therefore, we can invert equation 3.12b to obtain the intrinsic polarisation in terms of observable quantities to have;

$$F(\Phi_{RM}) = \int_{-\infty}^{+\infty} P(\lambda^2) \exp(-2j\Phi_{RM} \cdot \lambda^2) d\lambda^2 \quad (3.13)$$

Brentjens and de Bruyn 2005 proposed a window function $W(\lambda^2)$ to address the situations where we cannot observe at wavelengths $\lambda^2 < 0$ nor observe at all values of $\lambda^2 > 0$.

In this research, we simulate the polarisation maps of the Galactic synchrotron emission at low radio frequencies, where we use a simple model of the Galactic synchrotron polarization at high frequencies Giardino et al. 2002 together with Faraday screens that are introduced to account for the effects of rotation and depolarization at low frequencies.

Chapter 4

Simulations of Direction-dependent Instrumental Systematic Effects in Intensity Mapping Experiments

Overview

Chapter Four presents a notional primary beam simulations of KAT-7 using the OSKAR software. These beams are corrupted and then use for intensity mapping experiments.

4.1 Primary Beam Modelling

Over the past few years, there have been numerous techniques and software packages for modelling the primary beam response of an antenna. Some of the well known beam pattern packages are the `cassbeam`¹ - Cassegrain antenna simulator (Brisken 2003) which works by a simple geometrical ray-tracing technique and the commercially available GRASP² and FEKO³ software suites which operate through sophisticated EM modelling techniques. The latter two options produce the most accurate results but are quite expensive in computational and commercial terms. Appendix A.1 briefly describes how the ray tracing technique is used to obtain accurate voltage patterns for realistic antenna models such as the effects of central blockage, feed support legs and deviations from axis-symmetry. The EM simulation of GRASP is also discussed in Chapter 6 and in this research, the technique is used to construct the SKA1-MID primary beams.

¹<https://github.com/ratt-ru/cassbeam>

²<http://www.ticra.com/products/software/grasp>

³<https://www.feko.info/product-detail/overview-of-feko>

The purpose of this chapter is to study the observational effects of primary beam distortion. To do this, we develop a recipe for computing both an ideal beam pattern and a set of many perturbed patterns representing deformations of the antenna. These are technically achievable with GRASP or FEKO, but practically laborous for the purpose of this research where many perturbed patterns are essentially considered. Moreover, the study does not need a physical *precise* model of the KAT-7 primary beam, since future IM observations will not be carried out by KAT-7. KAT-7 is a notional example that is adopted for the purposes of this study. Therefore, what is rather needed is a relatively cheap way to compute ideal and perturbed beams, with perturbations that are representative of those seen in actual telescopes.

The GPU-accelerated OSKAR package use digital beamforming technique (Dulwich et al. 2009; Mort et al. 2010) to simulate primary beams of aperture arrays. It has the ability to include the following for each station beam response:

- (i) Introduce independent specification of pointing direction for each station or tile,
- (ii) Introduce apodisation weighting (this will modify the shape of the station beam),
- (iii) Introduce antenna element position and dipole orientation error and
- (iv) Introduce systematic and random element phase and gain errors.

The simulator is also capable of simulating interferometers (Mort et al. 2017; Sinclair et al. 2014) produced from large aperture arrays by utilising the Radio Interferometer Measurement Equation (RIME) (Hamaker, Bregman, and Sault 1996; Smirnov 2011) to generate the simulated visibilities. In general, this software is relatively ‘flexible’ to use for the scope of this Chapter compared to the previous softwares mentioned above.

Below, we show that OSKAR can be used to compute “dish-like” primary beams, by generating a geometric dipole distribution that mimics the aperture illumination function (AIF) of a dish. We stress that the resulting beam pattern is completely notional, and cannot be treated as a physically accurate model of the KAT-7 beam. It is, however, broadly representative of the dish beam. Furthermore, perturbations with respect to this ideal notional beam can be readily generated by perturbing the dipole distribution. The OSKAR approach gives us a practical way of generating such ideal and perturbed beams. As pointed out above, this is sufficient for the purposes of our work. Later in this section, we compare the primary beam perturbations produced by our approach with those seen in holographic measurements of JVLA antennas and show that the simulated perturbations are also broadly representative.

4.2 OSKAR Beam Model

In order to generate a “dish-like” primary beam model using OSKAR, we aim to mimic the AIF of a KAT-7-like dish by a 2D distribution of dipole positions. There are two important

features of the AIF that we need to model: a tapering off towards the edge of the dish (due to the illumination pattern of the feed), and aperture blockage by the centrally-mounted feed and its four supporting struts. To simulate illumination tapering, we generate a random distribution of 2D positions with a density that tapers off towards the edges of the dish. This is achieved by computing a set of positions as $x_d = R \cos(\psi)$ and $y_d = R \sin(\psi)$, where ψ is drawn from a uniform random distribution over a circular medium as $[0, 2\pi]$, and R is randomly generated by computing the *inverse transform method* (ITM) to enable us to draw a 1D radial probability distribution f_X . The following algorithm describes the ITM used to draw random values from a cumulative distribution function (CDF), F_X of a known density f_X :

- (i) Find the quantile function F_X^{-1} .
- (ii) Generate a uniform random number u .
- (iii) Return the random number $x = F_X^{-1}(u)$.

This study assumed the density function to be the Generalized Normal distribution, which is also known as the Super Gaussian (Pogany and Nadarajah 2009; Decker 1994), such that for $X \sim N(\mu, \sigma^s)$, we have;

$$f_X(x) = \frac{\sqrt{s}}{2\sigma\Gamma(\frac{1}{s})} \exp\left(-\left|\frac{x-\mu}{\sigma\sqrt{2}}\right|^s\right) \quad (4.1)$$

where, $-\infty < x < \infty$ is a random value, $-\infty < \mu < \infty$ is the mean, $\sigma > 0$ is the standard deviation, $s > 0$ is the peak factor and the gamma function is defined as $\Gamma(a, x) = \int_x^\infty t^{a-1} e^{-t} dt$.

The CDF of equation (4.1) is derived from the error functions such that the error function $erf(z)$ is defined by;

$$erf(z) = \frac{2}{\sqrt{\pi}} \int_0^z \exp(-t^2) dt \quad (4.2a)$$

$$= \frac{1}{\sqrt{\pi}} \gamma(1/2, z^2) \quad (4.2b)$$

and that of the complementary error function $erfc(z)$ is defined by;

$$erfc(z) = \frac{2}{\sqrt{\pi}} \int_z^\infty \exp(-t^2) dt \quad (4.3a)$$

$$= \frac{1}{\sqrt{\pi}} \Gamma(1/2, z^2) \quad (4.3b)$$

$$= 1 - erf(z) \quad (4.3c)$$

From equation (4.3), we can rewrite equation (4.2) as;

$$erf(z) = 1 - \frac{1}{\sqrt{\pi}} \Gamma(1/2, z^2) \quad (4.4)$$

If we put $s = 2$ in equation (4.1), the normal distribution is produced and the respective CDF becomes;

$$\int_{-\infty}^x f(x'|\mu, \sigma^2) dx' = \frac{1}{2} \left[1 + erf\left(\frac{x' - \mu}{\sigma\sqrt{2}}\right) \right] \quad (4.5)$$

From equation (4.4) we can rewrite equation (4.5) as;

$$F_2(x) = 1 - \frac{1}{2\sqrt{\pi}} \Gamma\left(\frac{1}{2}, \frac{x - \mu}{\sigma\sqrt{2}}\right) \quad (4.6)$$

Extending equation (4.6) into the general form in equation (4.1), we get;

$$F_s(x) = \begin{cases} \frac{\Gamma\left(\frac{1}{s}, \left\{\frac{x-\mu}{\sigma\sqrt{2}}\right\}^s\right)}{2\Gamma(\frac{1}{s})}, & \text{if } x \leq \mu \\ 1 - \frac{\Gamma\left(\frac{1}{s}, \left\{\frac{x-\mu}{\sigma\sqrt{2}}\right\}^s\right)}{2\Gamma(\frac{1}{s})}, & \text{if } x > \mu \end{cases} \quad (4.7)$$

Using equation (4.7) in the ITM, we can now draw a random number u from a uniform distribution over $[0, 1]$ and then compute the sample R as $R = |F^{-1}(u)|$. This results in a “flat-top Gaussian” radial density distribution as shown in Fig. 4.1, left. The parameters of the Super Gaussian distribution, σ and s control the width of the distribution and the aggressiveness of the taper. The values adopted in this work to produce the radial distribution in the figure are $\sigma = 0.82$ and $s = 12.0$.

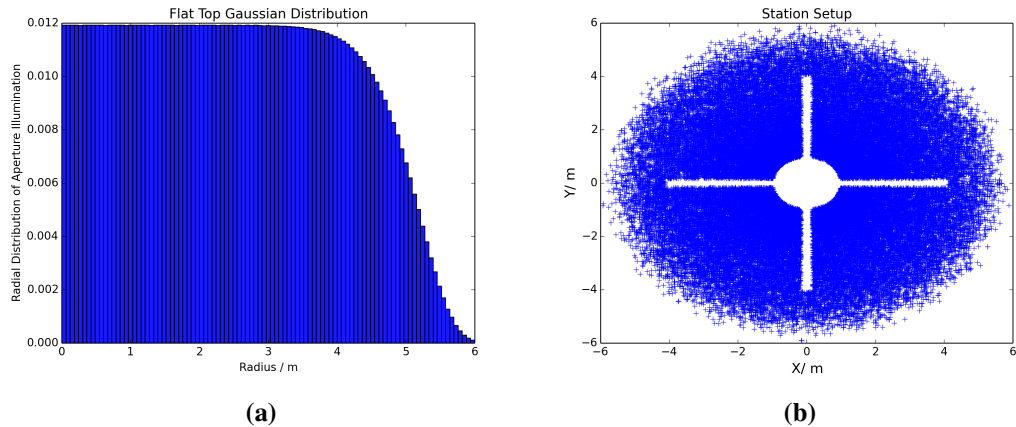


Figure 4.1: (a) The “flat-top Gaussian” radial distribution of dipole positions, mimicking a realistic aperture illumination where the dipoles get less dense towards the edge of the dish and (b) the resulting 2D dipole distribution with a mask applied to mimic aperture blockage ensures effective illumination and avoids tapering off.

We imitate the aperture blockage by simply masking the 2D positions. This ultimately results in the dipole distribution shown in Fig. 4.1, right. This dipole distribution is then fed into OSKAR as the “station layout”. For a given set of observational parameters (in particular, pointing at zenith), OSKAR then computes the station primary beam response. The resulting *Jones matrix* elements are shown in Fig. 4.2. Note how the beam pattern is broadly similar to that expected from a prime-focus dish. In particular, the first side-lobe shows the four-fold symmetry caused by the strut blockage. The presence of the phase component in Fig. 4.2 clearly shows that the so-called ideal beam is not that perfect since we are randomly placing the dipoles in the KAT-7 dish-like form, hence, the nominal X and Y dipoles are not directly orthogonal. In effect, we get the maximum $rmse \approx 0.10\%$ perturbed inaccuracies on the dish surface as reported in Fig. 4.3.

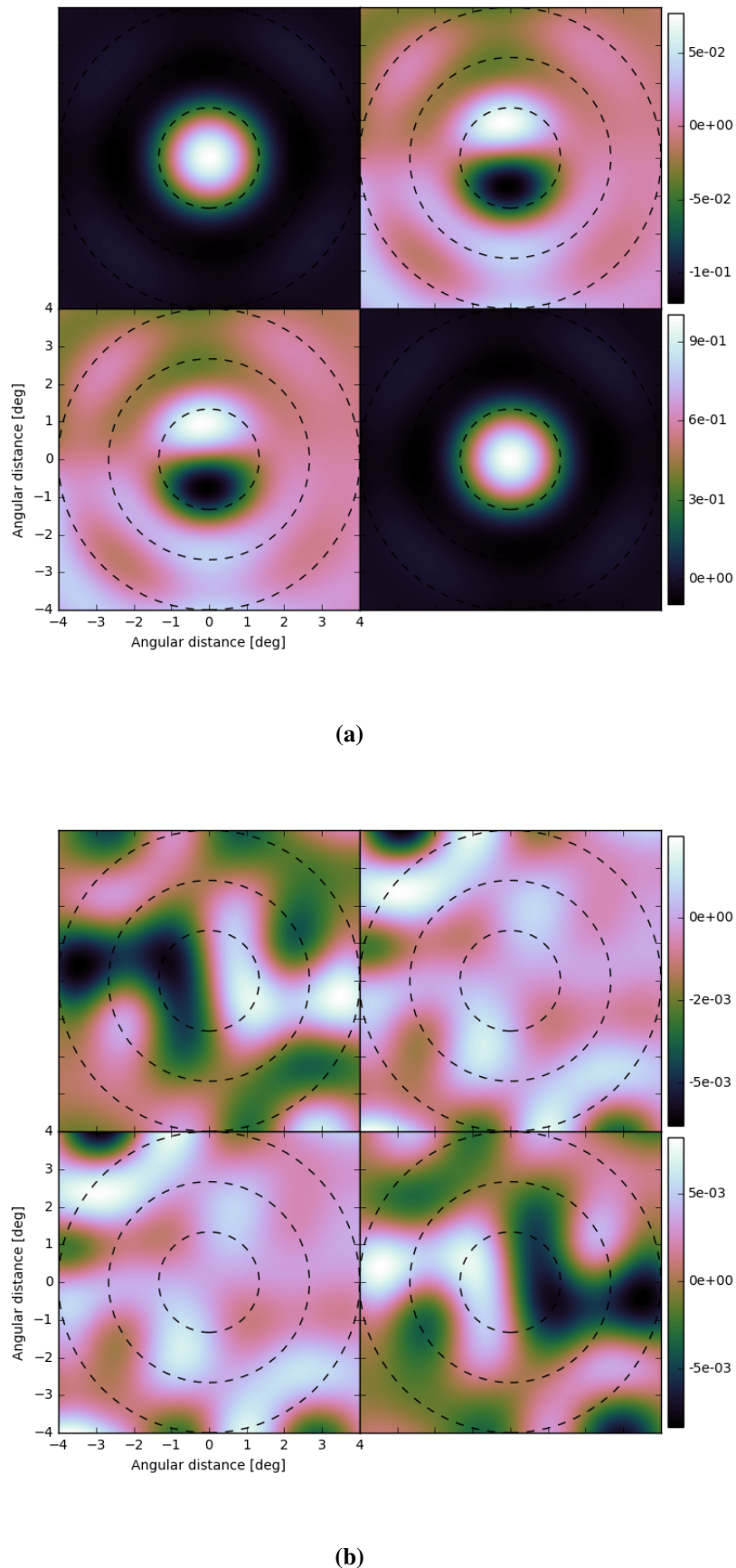


Figure 4.2: Jones matrix representation of the KAT-7-like beams produced by OSKAR and shown at 1 GHz: (a) real part (b) imaginary part. The intensity of the imaginary parts increases with fewer dipoles and becomes very less when more dipoles are used.

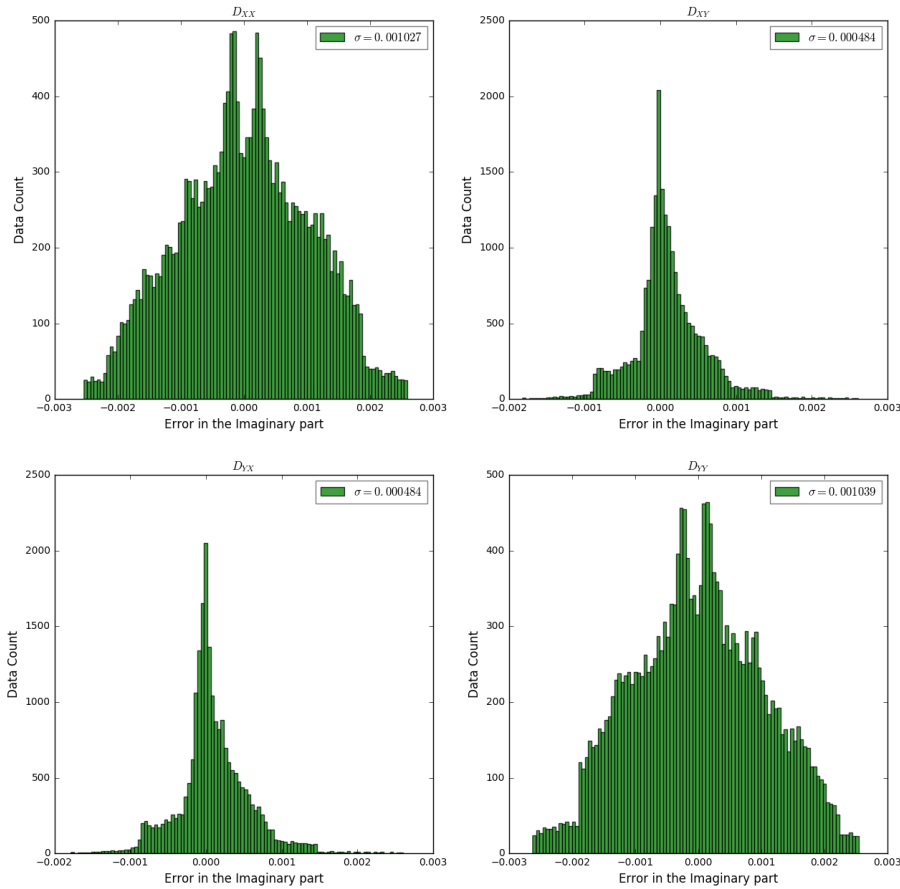


Figure 4.3: Histogram plots of the imaginary components in Fig. 4.2 showing the distribution of inaccuracies on the KAT-7 dish-like surface.

4.2.1 Jones and Mueller matrices

The Jones (Jones 1948; Jones 1942) formalism, originally formulated to describe optical polarization, was adapted to radio interferometry by Hamaker, Bregman, and Sault 1996 and extended to direction-dependent effects by Smirnov 2011. Here we use the derivations of the latter two works.

An electromagnetic plane wave propagating along axis z can be described at any point in space and time, by two complex amplitudes, e_x and e_y . Conventionally, we arrange these into a column vector, $e = [e_x, e_y]^T$. A single-dish observation aims to measure the pairwise coherencies of these amplitudes:

$$x = \begin{bmatrix} \langle e_x e_x^* \rangle \\ \langle e_x e_y^* \rangle \\ \langle e_y e_x^* \rangle \\ \langle e_y e_y^* \rangle \end{bmatrix} = \langle e \otimes e^* \rangle, \quad (4.8)$$

where $\langle \cdot \rangle$ represents the average over a time/frequency interval, and \otimes is the outer (or Kronecker) product operator. From these measured coherencies, the Stokes parameters $IQUV$ (written as a column vector s) may be derived, by definition, as (Born and Wolf 1980):

$$s = \begin{bmatrix} I \\ Q \\ U \\ V \end{bmatrix} = \begin{bmatrix} \langle e_x e_x^* \rangle + \langle e_y e_y^* \rangle \\ \langle e_x e_x^* \rangle - \langle e_y e_y^* \rangle \\ \langle e_x e_y^* \rangle + \langle e_y e_x^* \rangle \\ -i(\langle e_x e_y^* \rangle - \langle e_y e_x^* \rangle) \end{bmatrix} \quad (4.9)$$

We can rewrite this in terms of a 4×4 conversion matrix S^{-1} as⁴:

$$s = \begin{bmatrix} 1 & 0 & 0 & 1 \\ 1 & 0 & 0 & -1 \\ 0 & 1 & 1 & 0 \\ 0 & -i & i & 0 \end{bmatrix} x = S^{-1} x. \quad (4.10)$$

What the instrument actually measures is a set of pairwise correlations between two voltages induced by the EM field on two orthogonal mode feeds, v_a and v_b . The Jones formalism assumes that these are linearly related to the EM field (i.e. that all signal propagation effects are linear). This can be written as $v = Je$, where v is a column vector of the two voltages, and the 2×2 *Jones matrix* J describes signal propagation. The *measured* coherency x' can then be written as

$$x' = \langle v \otimes v^* \rangle = (J \otimes J^*) \langle e \otimes e^* \rangle = (J \otimes J^*) x, \quad (4.11)$$

and the measured Stokes parameter vector s' relates to the original Stokes vector via the so-called *Mueller matrix* M :

$$s' = Ms = S^{-1}(J \otimes J^*)Ss \quad (4.12)$$

For the purposes of this work, we ignore all propagation effects except the primary beam. In the context of this research, the Mueller matrix refers to the Mueller matrix of the primary beam. This matrix is direction-dependent (i.e. each direction of arrival will have its own matrix associated with it). The total Stokes flux measured by a single dish observation is then an integration over the FoV:

⁴This follows Smirnov 2011 in defining S as the conversion matrix between Stokes vectors and coherency vectors, $v = Ss$. Conversely, S^{-1} operates in the opposite direction. Note that Hamaker, Bregman, and Sault 1996 use T to refer to S^{-1} .

$$s'_{\text{tot}} = \iint_{lm} M(l, m) s(l, m) dldm, \quad (4.13)$$

where the integration is, in principle, over the entire celestial sphere, but in practice, since the Mueller matrix becomes negligibly small outside of a certain FoV, it can be replaced by a 2D integral over the tangent plane lm .

The Mueller matrix $M(l, m)$ corresponding to our KAT-7-like dish (Fig. 4.4a) can be derived from the Jones matrix $J(l, m)$ of Fig. 4.2. Note the physical meaning of the matrix elements J in equation (4.12) as displayed in Fig. 4.2. The on-diagonal terms of the Jones matrix describe the sensitivity of each feed, as a function of direction, to its matched EM field component. The off-diagonal terms describe leakage, i.e. the sensitivity of the feed to the nominally orthogonal EM field component. This leakage is due to mechanical and electronic imperfections in the antennas and feeds. The next subsection presents a mathematical model of the Mueller matrix derived in terms of Jones matrices.

4.2.1.1 Derivation of Mueller Matrix

The Mueller matrix gives a detailed characterisation of a polarisation element (Bass et al. 2009) such that the polarisation change is described in terms of intensities S_k . Therefore, following (Goldstein 2003), we decompose each element of J_{ij} in equation (4.12) into further 2×2 matrices to get:

$$J_{ij} = \frac{1}{2} \sum_{k=0}^3 \sigma_k \zeta_k \quad (4.14)$$

where,

$$\begin{aligned} \sigma_0 &= \begin{pmatrix} 1 & 0 \\ 0 & 1 \end{pmatrix}, & \sigma_1 &= \begin{pmatrix} 0 & 1 \\ 1 & 0 \end{pmatrix} \\ \sigma_2 &= \begin{pmatrix} 0 & -i \\ i & 0 \end{pmatrix}, & \sigma_3 &= \begin{pmatrix} 1 & 0 \\ 0 & -1 \end{pmatrix} \end{aligned}$$

The matrices $\{\sigma_0, \sigma_1, \sigma_2, \sigma_3\}$ provide a basis for the determination of the Mueller matrix M_{ij} . The matrix σ_0 is an identity matrix, σ_1, σ_2 and σ_3 are the 3 Pauli matrices which describe the propagation behaviour of the signal. ζ_k is associated to Pauli matrices:

$$[\zeta_k]_\alpha = [\sigma_k] \quad (4.15)$$

Hence, for $k = 0$,

$$\sigma_0 = \begin{pmatrix} 1 & 0 \\ 0 & 1 \end{pmatrix} = \begin{pmatrix} \zeta_{0,0} & \zeta_{0,1} \\ \zeta_{0,3} & \zeta_{0,4} \end{pmatrix} \quad (4.16)$$

We can deduce from equation (4.16) that;

$$\zeta_0 = \begin{pmatrix} \zeta_{0,0} \\ \zeta_{0,1} \\ \zeta_{0,2} \\ \zeta_{0,3} \end{pmatrix} = \begin{pmatrix} 1 \\ 0 \\ 0 \\ 1 \end{pmatrix} \quad (4.17)$$

Similarly, for $k = 1, 2$ or 3 , we get;

$$\zeta_1 = \begin{pmatrix} 1 \\ 0 \\ 0 \\ -1 \end{pmatrix}, \quad \zeta_2 = \begin{pmatrix} 0 \\ 1 \\ 1 \\ 0 \end{pmatrix}, \quad \zeta_3 = \begin{pmatrix} 0 \\ -i \\ i \\ 0 \end{pmatrix} \quad (4.18)$$

Normalizing equations (4.17) and (4.18) we get;

$$A = \frac{1}{2} \begin{pmatrix} 1 & 1 & 0 & 0 \\ 0 & 0 & 1 & -i \\ 0 & 0 & 1 & i \\ 1 & -1 & 0 & 0 \end{pmatrix} \quad (4.19)$$

The Mueller matrix M_{ij} in component form, can be expressed as;

$$M_{ij} = (A^*)^{-1} (J_{ij} \otimes J_{ij}^*) A^* \quad (4.20)$$

where, the symbol \otimes , represents the Kronecker product. Considering $U = (A^*)^{-1} = A^H$, we get;

$$M_{ij} = U (J_{ij} \otimes J_{ij}^*) U^{-1} \quad (4.21)$$

where, the notation H , represents Hermitian transpose such that;

$$U = \frac{1}{2} \begin{pmatrix} 1 & 0 & 0 & 1 \\ 1 & 0 & 0 & -1 \\ 0 & 1 & 1 & 0 \\ 0 & -i & i & 0 \end{pmatrix}$$

characterises the propagation effects of the measured signals.

The Jones matrices in equation (4.21) can be expanded as;

$$J \otimes J^* = \begin{pmatrix} J_{00} J_{00}^* & J_{00} J_{01}^* & J_{01} J_{00}^* & J_{01} J_{01}^* \\ J_{00} J_{10}^* & J_{00} J_{11}^* & J_{01} J_{10}^* & J_{01} J_{11}^* \\ J_{10} J_{00}^* & J_{10} J_{01}^* & J_{11} J_{00}^* & J_{11} J_{01}^* \\ J_{10} J_{10}^* & J_{10} J_{11}^* & J_{11} J_{10}^* & J_{11} J_{11}^* \end{pmatrix} \quad (4.22)$$

If we substitute equation (4.22) into (4.21), we can then expand the Mueller matrix elements in terms of Jones matrix elements:

$$m_{II} = (J_{00} J_{00}^* + J_{01} J_{01}^* + J_{10} J_{10}^* + J_{11} J_{11}^*)/2 \quad (4.23a)$$

$$m_{IQ} = (J_{00} J_{00}^* - J_{01} J_{01}^* + J_{10} J_{10}^* - J_{11} J_{11}^*)/2 \quad (4.23b)$$

$$m_{IU} = (J_{00} J_{01}^* + J_{01} J_{00}^* + J_{10} J_{11}^* + J_{11} J_{10}^*)/2 \quad (4.23c)$$

$$m_{IV} = i(J_{00} J_{01}^* + J_{10} J_{11}^* - J_{01} J_{00}^* - J_{11} J_{10}^*)/2 \quad (4.23d)$$

$$m_{QI} = (J_{00} J_{00}^* + J_{01} J_{01}^* - J_{10} J_{10}^* - J_{11} J_{11}^*)/2 \quad (4.23e)$$

$$m_{QQ} = (J_{00} J_{00}^* - J_{01} J_{01}^* - J_{10} J_{10}^* + J_{11} J_{11}^*)/2 \quad (4.23f)$$

$$m_{QU} = (J_{00} J_{01}^* + J_{01} J_{00}^* - J_{10} J_{11}^* - J_{11} J_{10}^*)/2 \quad (4.23g)$$

$$m_{QV} = i(J_{00} J_{01}^* - J_{10} J_{11}^* - J_{01} J_{00}^* - J_{11} J_{10}^*)/2 \quad (4.23h)$$

$$m_{UI} = (J_{00} J_{10}^* + J_{10} J_{00}^* + J_{01} J_{11}^* + J_{10} J_{01}^*)/2 \quad (4.23i)$$

$$m_{UQ} = (J_{00} J_{01}^* - J_{01} J_{00}^* + J_{10} J_{11}^* + J_{11} J_{10}^*)/2 \quad (4.23j)$$

$$m_{UU} = (J_{00} J_{11}^* + J_{11} J_{00}^* + J_{01} J_{10}^* + J_{10} J_{01}^*)/2 \quad (4.23k)$$

$$m_{UV} = i(J_{00} J_{11}^* + J_{10} J_{01}^* - J_{11} J_{00}^* - J_{01} J_{10}^*)/2 \quad (4.23l)$$

$$m_{VI} = i(-J_{00} J_{10}^* + J_{10} J_{00}^* - J_{01} J_{11}^* + J_{11} J_{01}^*)/2 \quad (4.23m)$$

$$m_{VQ} = i(-J_{00} J_{10}^* + J_{10} J_{00}^* + J_{01} J_{11}^* - J_{11} J_{01}^*)/2 \quad (4.23n)$$

$$m_{VU} = i(-J_{00} J_{11}^* + J_{11} J_{00}^* - J_{01} J_{10}^* + J_{10} J_{01}^*)/2 \quad (4.23o)$$

$$m_{VV} = (J_{00} J_{11}^* - J_{10} J_{01}^* + J_{11} J_{00}^* - J_{01} J_{10}^*)/2 \quad (4.23p)$$

If we substitute the elements in equation (4.23) into equation (4.12), we get:

$$\begin{pmatrix} S'_I \\ S'_Q \\ S'_U \\ S'_V \end{pmatrix} = \begin{pmatrix} m_{II} & m_{IQ} & m_{IU} & m_{IV} \\ m_{QI} & m_{QQ} & m_{QU} & m_{QV} \\ m_{UI} & m_{UQ} & m_{UU} & m_{UV} \\ m_{VI} & m_{VQ} & m_{VU} & m_{VV} \end{pmatrix} \begin{pmatrix} S_I \\ S_Q \\ S_U \\ S_V \end{pmatrix} \quad (4.24)$$

The elements M_{ij} in equation (4.24) represent the complete beams in Fig. 4.4. The diagonal terms of the Mueller matrix describe the sensitivity of the measured Stokes $IQUV$ components to their true counterparts, as a function of direction. The off-diagonal terms describe spurious

leakage between the measured Stokes components. We can schematically write this as;

$$M = \begin{bmatrix} I \rightarrow I' & Q \rightarrow I' & U \rightarrow I' & V \rightarrow I' \\ I \rightarrow Q' & Q \rightarrow Q' & U \rightarrow Q' & V \rightarrow Q' \\ I \rightarrow U' & Q \rightarrow U' & U \rightarrow U' & V \rightarrow U' \\ I \rightarrow V' & Q \rightarrow V' & U \rightarrow V' & V \rightarrow V' \end{bmatrix}$$

Fig. 4.4a displays the KAT-7-like modelled beams produced from OSKAR in Mueller matrix form. For example, the elements $I \rightarrow Q, U, V$ in the 4×4 images describe how much of Stokes I intensity leaks into the polarisation components Q, U, V while, $Q \leftrightarrow U, Q \leftrightarrow V, U \leftrightarrow V$ are the cross-polarisation leakage terms. Section 4.2.2 describes further how the OSKAR package is used to introduce errors in the modelled beams to produce beam distortion.

4.2.2 Primary Beam Perturbation

The modelled beams produced in this chapter are corrupted with two kinds of errors. The first error type is the introduction of systematic and time-variable gain and phase errors. The nominal purpose of this in OSKAR is to simulate per-element gain and phase error before the beamformer, so that the beam-forming weight B^w , for a particular beam direction (θ_{bm}, ϕ_{bm}) , with dipole position (x, y, z) and time t becomes;

$$B^w(u) = B_{geo}^w(u)(G_0 + G_{error}) \exp(j[\phi_0 + \phi_{error}]) \quad (4.25)$$

where $u = (\theta_{bm}, \phi_{bm}, x, y, z, t)$, G_{error} and ϕ_{error} are pseudo-random values at each time-step t using a Gaussian distribution with standard deviations G_{std} and ϕ_{std} respectively. The complex multiplicative factor applied to each element is denoted by the parameters Gain G_0 and phase ϕ_0 respectively. This complex factor joins with the geometric beam-forming weight B_{geo}^w to produce the array factor to evaluate the station beam at each source position. For the purpose of our “disk-like” simulation, we introduced 5° phase error and 10% gain error into the beam-forming weight to distort the beams as shown in Appendix A.1a. These sort of errors represent imperfections in the parabolic reflector surface (which, in real life, result in amplitude and phase errors over the aperture). The second error introduced is to uniformly change the orientation of the dipoles to create systematic error feed angle displacement as presented in Appendix A.1b. Figs. 4.4b and 4.4c show the beam errors produced by computing the differences between the true modelled beams in Fig. 4.4a and the two distorted beams in Appendices A.1a and A.1b respectively. The on-diagonal components of these beam errors represent the residual leakages and the off-diagonals show the residual systematic leakages. The maximum residual leakages produced in Figs. 4.4b and 4.4c are $\approx 20\%$ and 10% respectively.

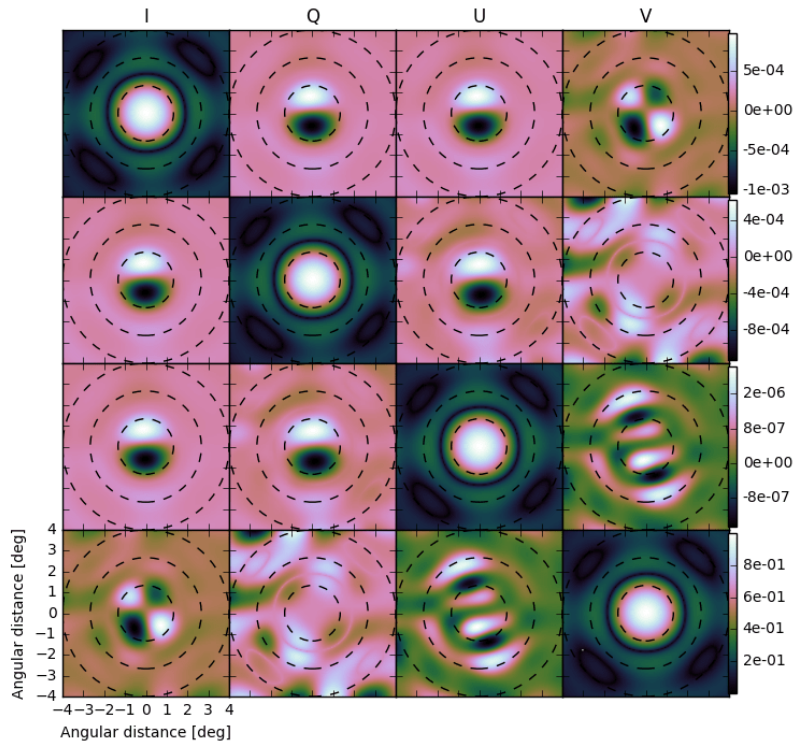
In order to see whether the level of beam distortion introduced in this manner is realistic, we compare the beam patterns obtained via holography measurements of two different JVLA

dishes as presented in Appendices A.2a and A.2b. The measurement technique employed in producing these beams is based on the EVLA Memo (Perley and al. 2015) which consists of the utilisation of the Fourier transform relation between the complex far-field (i.e. amplitude and phase) radiation pattern of an antenna $\chi(u, v)$ and the complex aperture distribution $\zeta(l, m)$:

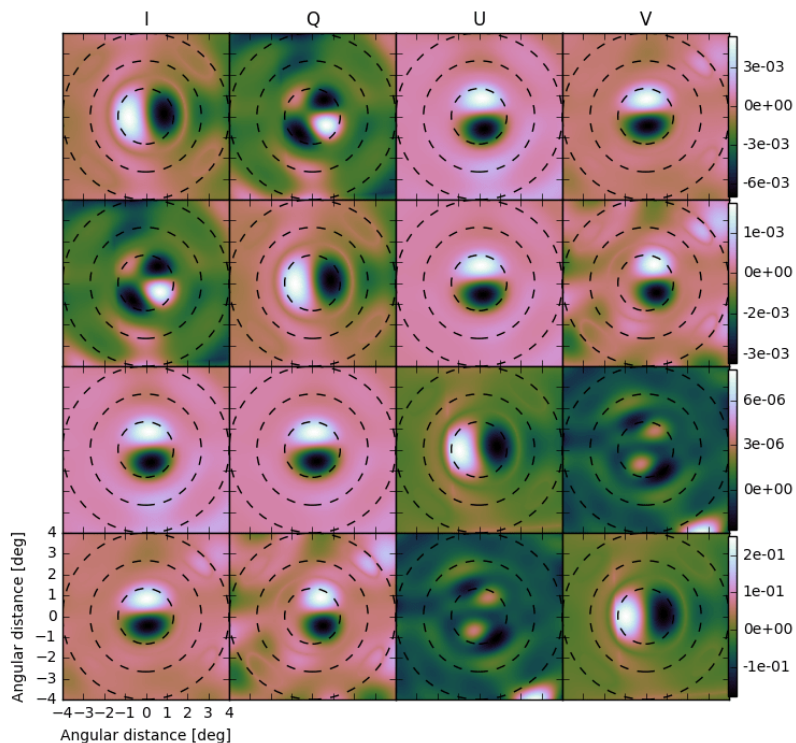
$$\chi(u, v) = \iint_{-\infty}^{+\infty} \zeta(l, m) \exp\{i2\pi(lu + mv)\} dl dm \quad (4.26)$$

where $u = x/\lambda$ and $v = y/\lambda$ denote the rectilinear coordinates in wavelength, in the aperture plane. The coordinates (l, m) are the direction cosine with respect to the aperture plane. The difference between the two holography measurements Fig. 4.4d corresponds to the real-life differences between the primary beam patterns of two nominally identical dishes. Note how these beam errors give a maximum residual leakage of $\simeq 10\%$. This demonstrates that our beam distortion procedure, using the error values we have adopted, results in physically realistic primary beam distortion levels.

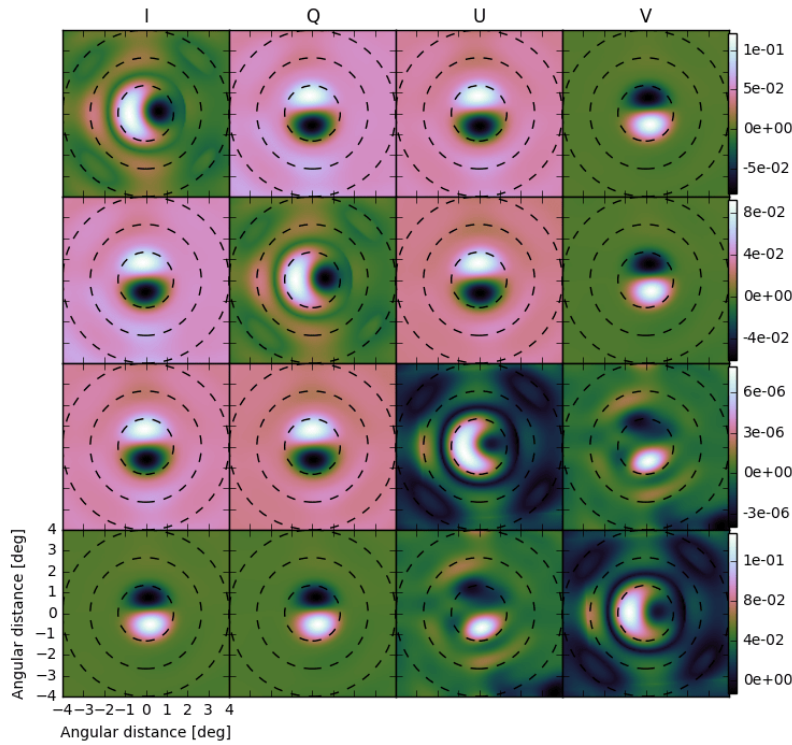
Having thus armed ourselves with an instrumental model, we now proceed to discuss the nature of our simulated sky.



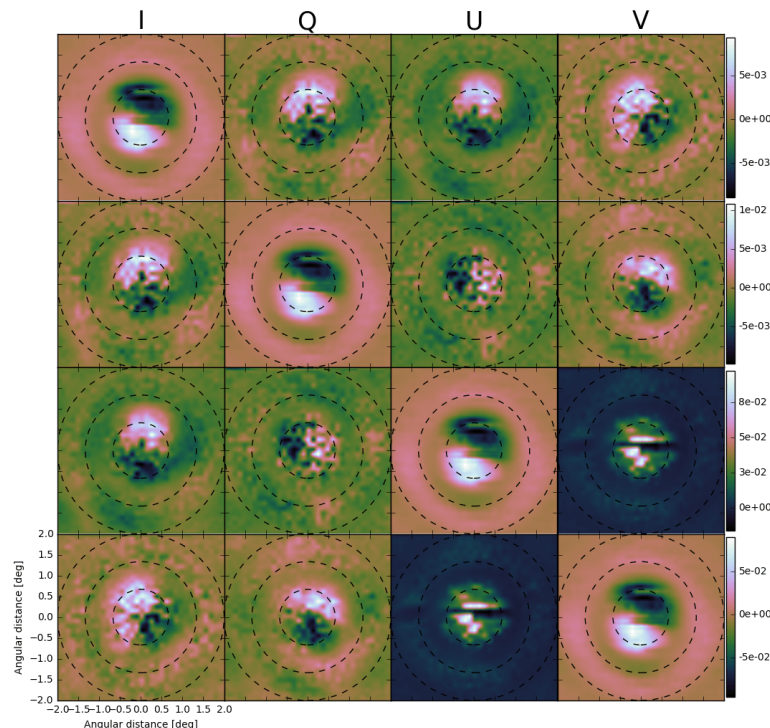
(a) 4×4 images of KAT-7 uncorrupted OSKAR beams.



(b) Difference between the uncorrupted OSKAR beams in Fig. 4.4a and the gain and phase error beams in appendix A.1a



(c) Difference between uncorrupted OSKAR beams in Fig. 4.4a and the dipole orientation error beams in appendix A.1b.



(d) Difference between JVLA holography measured beams in Appendices A.2a and A.2b.

Figure 4.4: Mueller matrix representations of full polarisation beams produced at 1 GHz

4.3 Simulation

4.3.1 Full-sky Convolution

Convolution is a mathematical operation that interpolates two functions ψ_1 and ψ_2 to produce a third function χ that is typically viewed as a modification of one of the original functions. Consider $C_v(x)$ to be the convolution of $H_1(x)$ with $H_2(x)$, then its Fourier pair $\chi(v)$, is the product of $\psi_1(v)$ and $\psi_2(v)$ which are the Fourier pairs of $H_1(x)$ and $H_2(x)$ respectively. Thus,

$$H_1(x) \otimes H_2(x) \rightleftharpoons \psi_1(v).\psi_2(v) \quad (4.27)$$

where, the symbol \otimes denotes the convolution operator. By definition,

$$\begin{aligned} C_v(x) &= H_1(x) \otimes H_2(x) \\ &= \int_{-\infty}^{\infty} H_1(x')H_2(x - x')dx \end{aligned} \quad (4.28)$$

Taking the Fourier transform of both sides in equation (4.28), we get;

$$\begin{aligned} \chi(v) &= \int_{-\infty}^{\infty} C_v(x)e^{-2\pi jvx}dx \\ &= \int_{-\infty}^{\infty} \int_{-\infty}^{\infty} H_1(x')H_2(x - x')e^{-2\pi jvx}dx'dx \end{aligned} \quad (4.29)$$

Let $y = x - x' \Rightarrow dy = dx$

$$\chi(v) = \int_{-\infty}^{\infty} \int_{-\infty}^{\infty} H_1(x')H_2(y)e^{-2\pi jv(x'+y)}dx'dy \quad (4.30)$$

Equation (4.30) can therefore be separated to give

$$\begin{aligned} \chi(v) &= \int_{-\infty}^{\infty} H_1(x')e^{-2\pi jvx'}dx'. \int_{-\infty}^{\infty} H_2(y)e^{-2\pi jvy}dy \\ &= \psi_1(v).\psi_2(v) \end{aligned} \quad (4.31)$$

Expressing the general definition in equation (4.31) into 2D discrete form, we have;

$$\begin{aligned} \chi(v_1, v_2) &= H_1(v_1, v_2) \otimes H_2(v_1, v_2) \\ &= \sum_{i=-\infty}^{\infty} \sum_{j=-\infty}^{\infty} H_1(i - v_1, j - v_2)H_2(i, j) \end{aligned} \quad (4.32)$$

In equation (4.32), the values $\chi(v_1, v_2)$ of the discrete function χ for any particular (v_1, v_2) follows by multiplying each value $H_2(i, j)$ of the discrete function H_2 with a kernel function $H_1(i - v_1, j - v_2)$ between a particular (v_1, v_2) and varying (i, j) where, $(-\infty < i, j < +\infty)$. Thus, each value $\chi(v_1, v_2)$ of the function χ is a weighted mean of the values $H_2(i, j)$ with weights $H_1(i - v_1, j - v_2)$ defined by the function H_1 . In this chapter, we apply similar

technique to simulate the foreground of the sky.

To perform an IM experiment, the radio telescope(s) is pointed at different patches of the sky so that the instrument can measure the overall intensity emerging from patches from the autocorrelation of the radio signal, as a function of frequency. In order to emulate this observation technique in our IM simulation, the discrete convolution in equation (4.33) is used to measure the intensities of the full sky synchrotron maps in Fig. 3.3. Let (θ, ϕ) denote the celestial coordinates of the foregrounds of the sky such that, B are the fully polarised beams and f_{sky} are the foregrounds of the sky. We can then model the convolved foregrounds to be:

$$\begin{aligned} F^{conv}(\theta, \phi) &= B(\theta, \phi) \otimes f_{sky}(\theta, \phi) \\ &= \sum_{(\theta', \phi') = \lfloor (\theta, \phi) \rfloor} B(\theta' - \theta, \phi' - \phi) \cdot f_{sky}(\theta', \phi') \end{aligned} \quad (4.33)$$

where $(\theta', \phi') \leq npix$ and the symbol $\lfloor \cdot \rfloor$ denotes the nearest pixels. The measured foreground pixel values $F^{conv}(\theta, \phi)$ of the discrete function F^{conv} for any particular (θ, ϕ) follows by multiplying each foreground pixel value $f_{sky}(\theta, \phi)$ of the discrete function f_{sky} with a beam $B(\theta' - \theta, \phi' - \phi)$ between a particular (θ', ϕ') and varying (θ, ϕ) . Thus, each pixel value $F^{conv}(\theta, \phi)$ of the function F^{conv} is a weighted mean of the pixel values $f_{sky}(\theta, \phi)$ with weights $B(\theta' - \theta, \phi' - \phi)$ defined by the function B .

If we take the modelled beams B in Fig. 4.4a to convolve the full-sky polarisation maps (f_{sky}) in Fig. 3.3, we obtain the convolved maps F^{conv} in Fig. 4.5. The same approach is repeated using the distorted beams in Appendices A.1a and A.1b to produce the corrupted maps in Appendices A.3 and A.4. The differences between these corrupted convolved figures produce the residual plots in Figs 4.6 and 4.7 respectively. In addition, using the holography measured beams in Appendices A.2a and A.2b to produce their respective convolved maps, we obtain their residual plots in Fig 4.8. The original spatial distributions of the foregrounds in Fig. 3.3 are clearly maintained in the diagonals of the convolved maps as shown in Fig. 4.5. This happens when we simulate the full-sky maps with the gain terms in the diagonals of our beams.

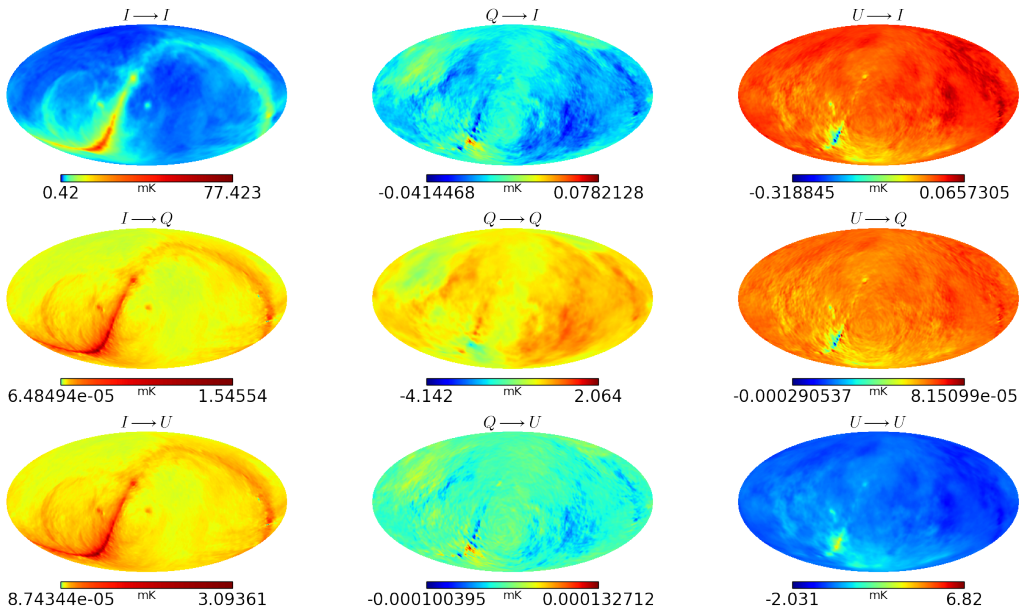


Figure 4.5: Convolved full-sky polarisation maps using the non-distorted OSKAR beams. For example, we used the m_{II} beam in Fig. 4.4a to convolve Stokes I in Fig. 3.3 and produce the convolved map $I \rightarrow I$, then we used m_{QI} beam to convolve Stokes Q to obtain the convolved map $Q \rightarrow I$, also, using the m_{UI} beam to convolve Stokes U we produced the convolved map $U \rightarrow I$. The other convolved maps are produced in the same manner using their respective beams.

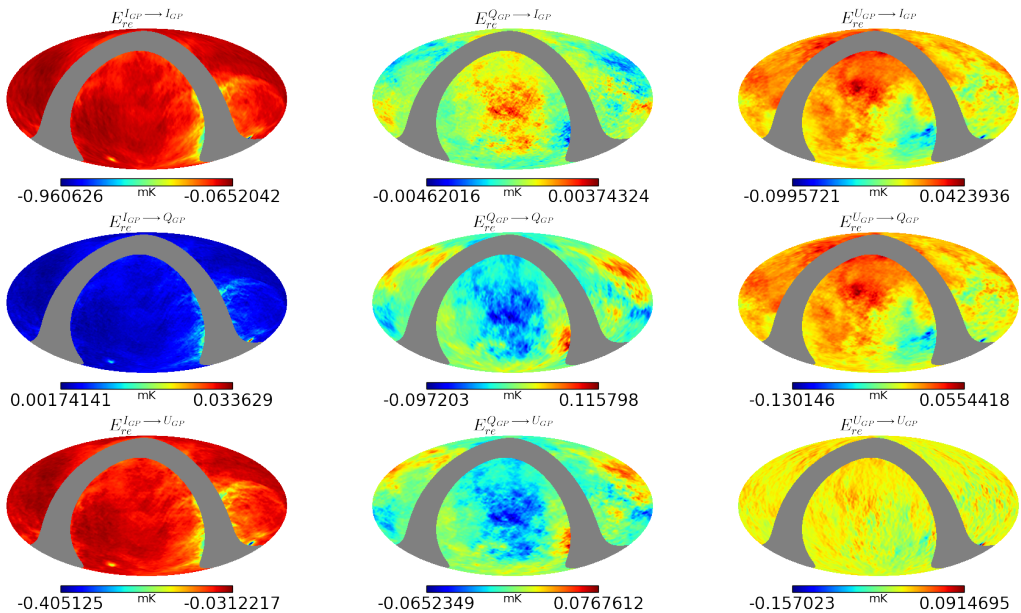


Figure 4.6: Systematic errors of full-sky maps produced by computing the relative error between the absolute of the convolved true sky maps and the corrupted sky maps due to gain and phase error beams.

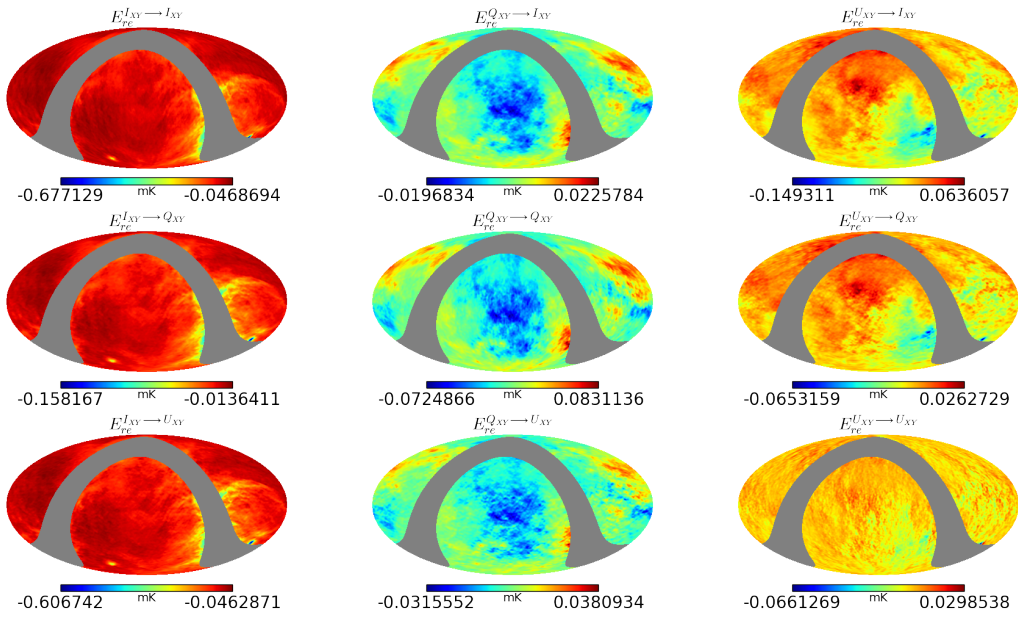


Figure 4.7: Systematic errors of full-sky maps produced by computing the relative error between the absolute of the convolved true sky maps and the corrupted sky maps due to dipole orientation error beams.

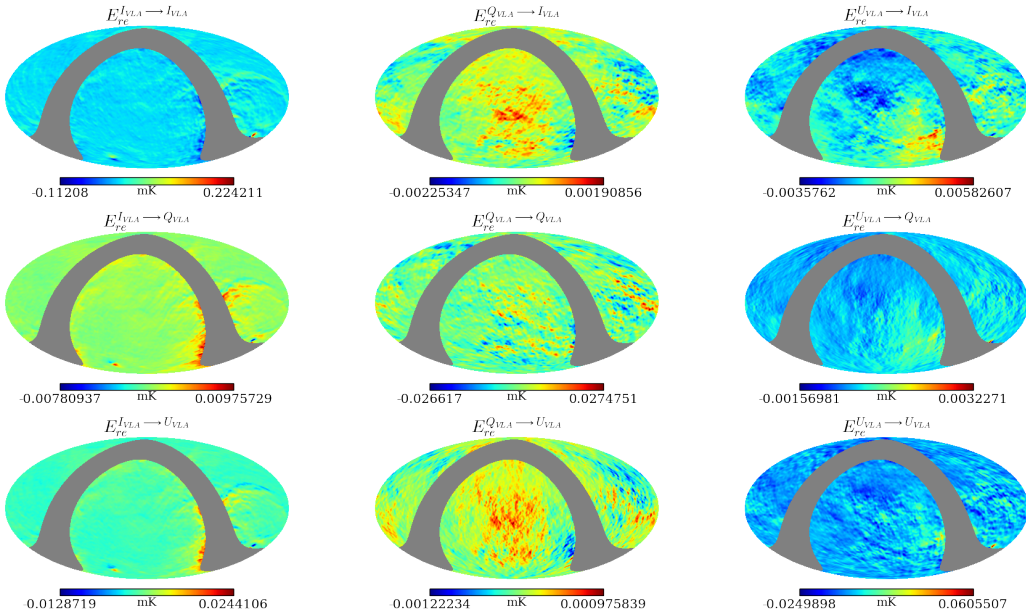


Figure 4.8: Systematic errors of full-sky maps produced by computing the relative error between the absolute of the convolved true sky maps and the JVLA holography beams for antennas 5 and 6.

In IM experiments, what is actually interested in, is to measure the total intensity of a signal. Therefore, in section 4.3.2, we present a mathematical model of the convolved power spectrum using the angular power spectrum to describe the spatial distribution of the measured foregrounds in a spherical harmonic domain.

4.3.2 Angular Power Spectrum

In CMB studies (Abitbol, Hill, and Johnson 2016; Krachmalnicoff et al. 2016; Wolz et al. 2015; Souradeep, Saha, and Jain 2006; Saha, Jain, and Souradeep 2006; White 1998), it is a common practice to characterize the distribution of flux in a sphere with the angular power spectrum. The same approach is employed in this project to describe the diffuse foreground intensity over spherical harmonics $Y_{l,m}$.

Consider the foreground of the sky is emitted by our own galaxy or the distribution galaxies emitting 21-cm with an intensity equivalent to $T(\hat{\sigma})$. We can measure the total source emission temperature $T(\hat{\sigma})$, in each sky pixel and represent the distribution as an expansion in 2D spherical harmonics:

$$T(\hat{\sigma}) = \sum_{l=0}^{\infty} \sum_{m=-l}^{l} a_{lm} Y_{lm}(\hat{\sigma}) \quad (4.34)$$

where $\hat{\sigma} \equiv (\psi, \xi)$ is the unit vector in some direction in the sky and $Y_{lm}(\hat{\sigma})$ are the spherical harmonic functions evaluated in the direction $\hat{\sigma}$ such that, they form a complete orthonormal set on the unit sphere and can be expressed as;

$$Y_{lm}(\psi, \xi) = (-1)^m \sqrt{\frac{2l+1}{4\pi} \frac{(l-m)!}{(l+m)!}} P_l^m(\cos \psi) e^{im\xi} \quad (4.35)$$

In equation (4.35), the indices $l = 0, \dots, \infty$ and $-l < m < l$ with P_l^m denoting the Legendre polynomials. l is known as the multipole which denotes a given angular scale γ in the sky, where $\gamma \simeq 180^\circ/l$. The coefficients a_{lm} in equation (4.34),

$$a_{lm} = \int_{\psi=-\pi/2}^{\pi/2} \int_{\xi=0}^{2\pi} T_{lm}(\hat{\sigma}) Y_{lm}^*(\hat{\sigma}) d\xi d\psi \quad (4.36)$$

is related to what we normally do in the Fourier space.

Consider any two pixels, then the correlation function of the temperatures is expressed as;

$$C_{cr}(\Theta) = \langle T(\hat{\sigma}_i) T(\hat{\sigma}_j) \rangle, \quad \Theta = \sigma_i \cdot \sigma_j \quad (4.37)$$

where the brackets $\langle \rangle$, denote averaging over $2l+1$ values of m . Equation (4.37) strictly relies on the separation angle between two sources as discussed in Schramm and Galeotti 1997, p. 78 and therefore, can be rewritten in terms of Legendre polynomials:

$$C_{cr}(\Theta) = \sum_{l=0}^{\infty} \frac{2l+1}{4\pi} C_l P_l(\cos \Theta) \quad (4.38)$$

From equation (4.38), we can estimate the statistical distribution of the angular power spectrum \hat{C}_l of the entire sky in terms of a_{lm} :

$$\hat{C}_l = \frac{1}{2l+1} \sum_m |\hat{a}_{lm}|^2, \quad -l < m < l \quad (4.39)$$

In this work, we used *anafast* in HEALPix library to compute the auto-power spectrum \hat{C}_l of foregrounds of the sky in section 4.3.1 by executing an approximate, discrete point-set quadrature on a sphere sampled at the HEALPix pixel centres. Spherical harmonic transforms are then computed using recurrence relations for Legendre polynomials on co-latitude ψ and Fast Fourier Transforms on longitude ξ .

4.4 Results and Analysis

The measured maps of $\{I^T, Q^T, U^T\}$ (in row 1), $\{I_D^{GP}, Q_D^{GP}, U_D^{GP}\}$ (in row 2) and $\{I_D^{XY}, Q_D^{XY}, U_D^{XY}\}$ (in row 3) in Fig. 4.9 are generated by convolving both the true and perturbed model beams with the foregrounds in Fig. 3.3 and then summing across each of the convolved Stokes terms. The last two rows are the corresponding errors in Stokes I, Q and U . Note the similarities between these measured maps, if we compute the differences between them, we can see these simulated maps are not the same and this is even confirmed by the systematic differences in the maps displayed in Figs. 4.6 and 4.7. A similar approach is employed to obtain the measured maps in Appendix A.5. These are obtained when the foregrounds are convolved with the JVLA measured beams.

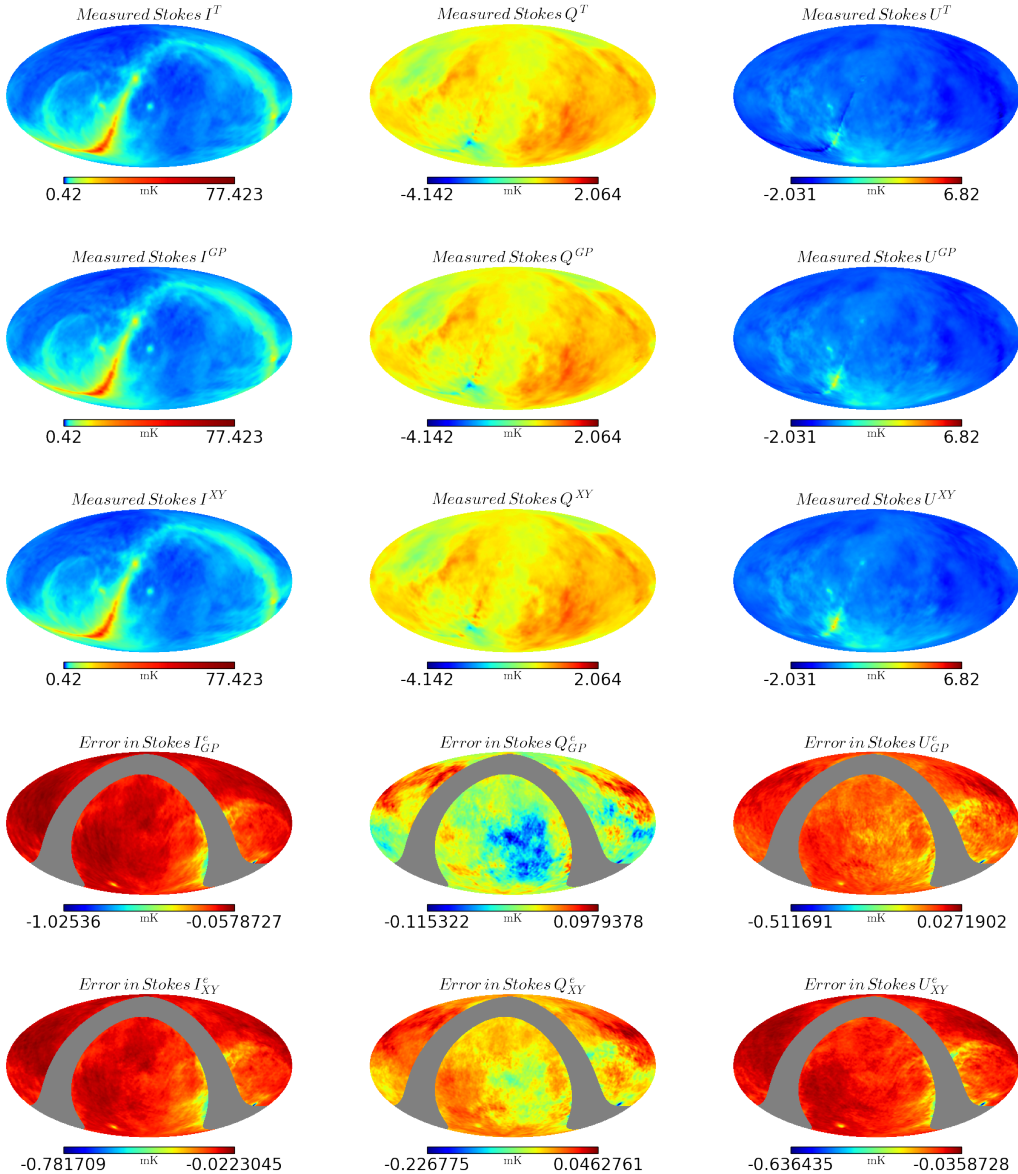


Figure 4.9: The top and middle maps depict the measured foregrounds of Stokes I , Q and U for using the non-distorted and the gain and phase error full polarisation beams respectively. The bottom maps are the corresponding errors in I , Q and U .

The auto-power spectra presented in Fig. 4.10 estimate the density of the measured foregrounds at different multipole moments. Note how the beam power in each plot of both OSKAR and the holographic measured beams is normalised to 1. It is computed by finding the quotient of the power spectrum of the convolved sky map and the original sky map. The OSKAR beam power plots in Stokes I , Q and U , converge at a multipole moment of $l = 60$. This value relates to an angular scale of 3.0° on the sky whilst the power spectra of the JVLA beams converge just at a multipole moment of $l = 90$, giving an angular scale of 2.0° on the sky. These angular scales are equivalent to the beam sizes used to convolve the original maps in Fig. 3.3. Note also the effect of these two beams on the convolved power spectra of Stokes I , Q and U . The measured values for the convolved power spectra of Stokes I , Q and

U are 10 mK^2 , 10^{-1} mK^2 and 10^{-1} mK^2 respectively. These values in Fig. 4.10 actually predicted the foreground's temperature of the true sky. Hence, the corresponding errors in I , Q and U due to perturbation of the beams are $\approx 10^{-2} \text{ mK}^2$, 10^{-4} mK^2 and 10^{-5} mK^2 respectively.

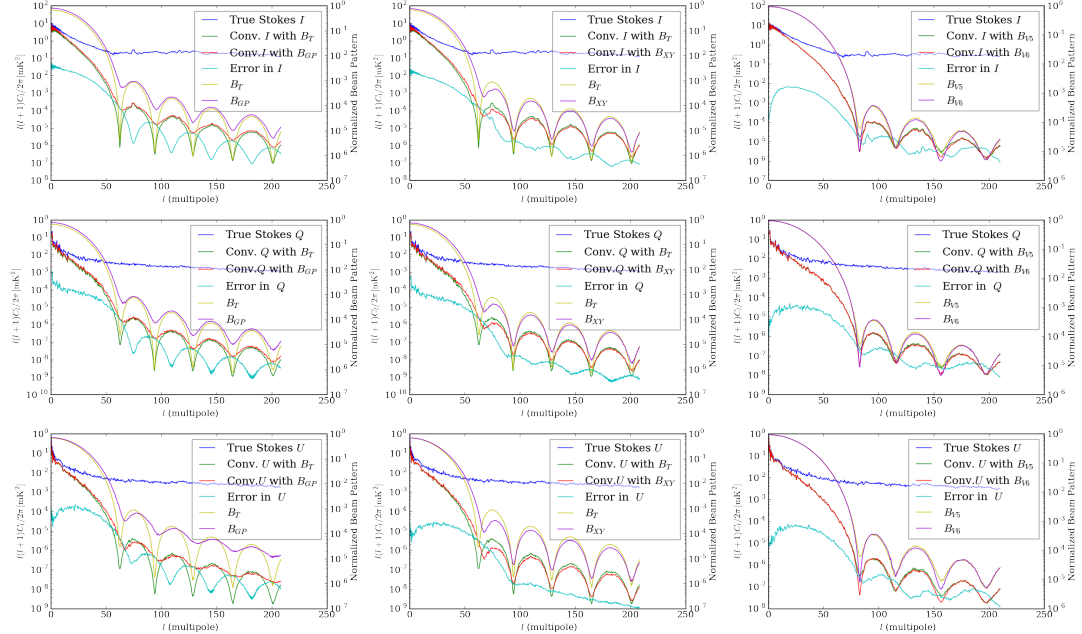


Figure 4.10: Convolved angular power spectra estimation of foreground maps. First row: Shows Stokes I spectra plots for using simulated beams and holography measured beams. Second row: Displays Stokes Q spectra plots for using simulated beams and holography measured beams. Third row: Displays Stokes U spectra plots for using simulated beams and holography measured beams.

In IM experiments, the HI signal is measured in Stokes I , so we are particularly interested in the total intensity and the leakages from polarisation into Stokes I (that is, $|Q + iU| \rightarrow I$). Fig. 4.11 shows how the $|Q + iU| \rightarrow I$ leakage and the error in the Stokes I map affect the HI signal. Here, a spherical power spectrum of the simulated model of 21-cm brightness temperature at $z \approx 0.67$ produced from the CRIME⁵ fast simulation software and described by Alonso, Ferreira, and Santos (2014) is generated and then compared with the spectra plots of the Galactic foregrounds. The HI signal power in Fig. 4.11(right) is higher than the I -leakage at a multipole moment of $l = 100$ which is about 3 orders of magnitude greater at lower scales. This occurs when we do not correct for the beam errors (i.e., gain, phase and orientation of dipole errors) in $Q \rightarrow I$ and $U \rightarrow I$ at all. The fractional leakage of $|Q + iU|$ and I is computed to give $\approx 1.0\%$ for the intrinsic case ($|Q + iU|_T$) where a true model of the beam is known. In this case, the power of the HI signal is higher than the I -leakage at a multipole moment of $l = 25$. The spectra plots reported in Fig. 4.11(left), try to correct the columns that feeds into Stokes I (i.e., $Q \rightarrow I$, $U \rightarrow I$ and $I \rightarrow I$) by assuming the corresponding beams (i.e., m_{QI} , m_{UI} and m_{II}) are not known to the extent to which they have

⁵<http://intensitymapping.physics.ox.ac.uk/CRIME.html>

been assumed in this project, then the power spectrum of the HI signal can be observed at a multipole moment of $l = 25$. We conclude that if the knowledge of the beam is of a similar quality than the one assumed in this chapter then we will be able to recover the cosmological HI signal without great problems and without further calibration on scales larger than $l = 100$, however, this work suggests that if polarisation calibration is performed correctly then results can be improved and we can recover scales above $l = 25$. In either case, given the strength of the foregrounds in the galactic centre we will not be able to recover scales larger than $l < 25$.

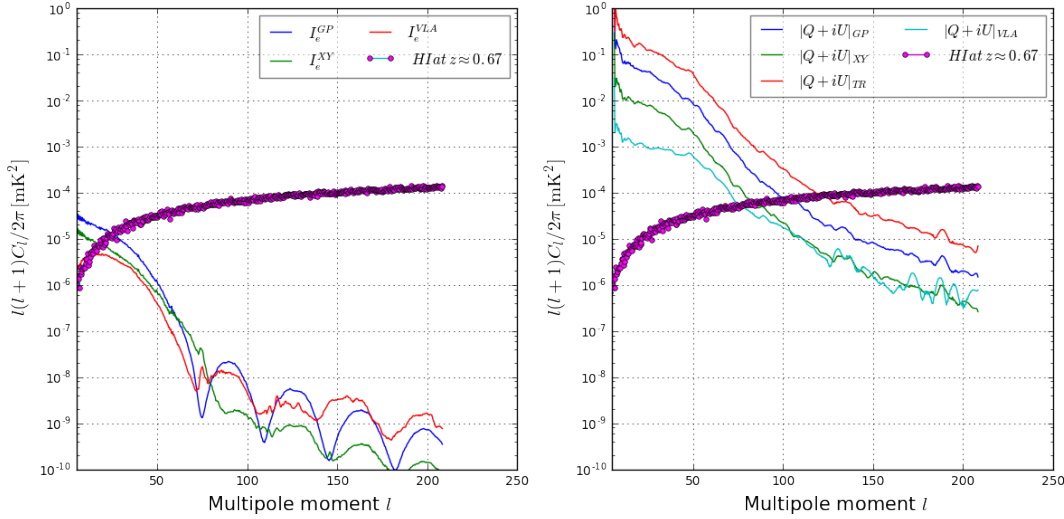


Figure 4.11: Comparing polarisation leakages when there is no beam correction with correcting the beam errors in Stokes I : (a) Quantifies the amount of leakages into Stokes I which is caused by both measured (holography) and modelled (OSKAR) beams. The solid circular spectrum is the simulated 21-cm brightness temperature described by Alonso, Ferreira, and Santos (2014) at a $z \approx 0.67$. The solid thin spectrum ($|Q + iU|_T$), is the leakage in I when the true modelled beams in Fig. 4.4a are used. The dashed spectra plots ($|Q + iU|_{\text{GP}}$, $|Q + iU|_{\text{XY}}$, $|Q + iU|_{\text{VLA}}$) are the leakages in I when we use modelled beams with gain, phase and dipole displacement and holography measured beams respectively. (b) These spectra plots show the estimate of the 21-cm signal when we correct for the errors in Stokes I beam.

The spectra plots in Fig. 4.12 evaluate the systematic effects of beam errors on Stokes I , Q and U . These residuals are determined as a result of the respective differences between the distorted and non-distorted measured full-sky maps as depicted in Fig. 4.6. We then compute the standard errors of these residual plots to estimate the uncertainties in the angular power spectra when modelled beams are assumed whilst the foreground maps are convolved with the measured beams. Table A.1 in Appendix A.4 shows the corresponding inaccuracies in the power spectrum estimation. For instance, the standard errors introduced in $Q \rightarrow I$ are $\approx 0.015\%$ (due to gain and phase errors) and 0.014% (due to dipole orientation errors). Also, that of $U \rightarrow I$ are $\approx 0.005\%$ and 0.0045% accordingly. The uncertainties in the spectra plots are as a result of the inaccuracies on the surface of the modelled dish as presented in Fig. 4.3.

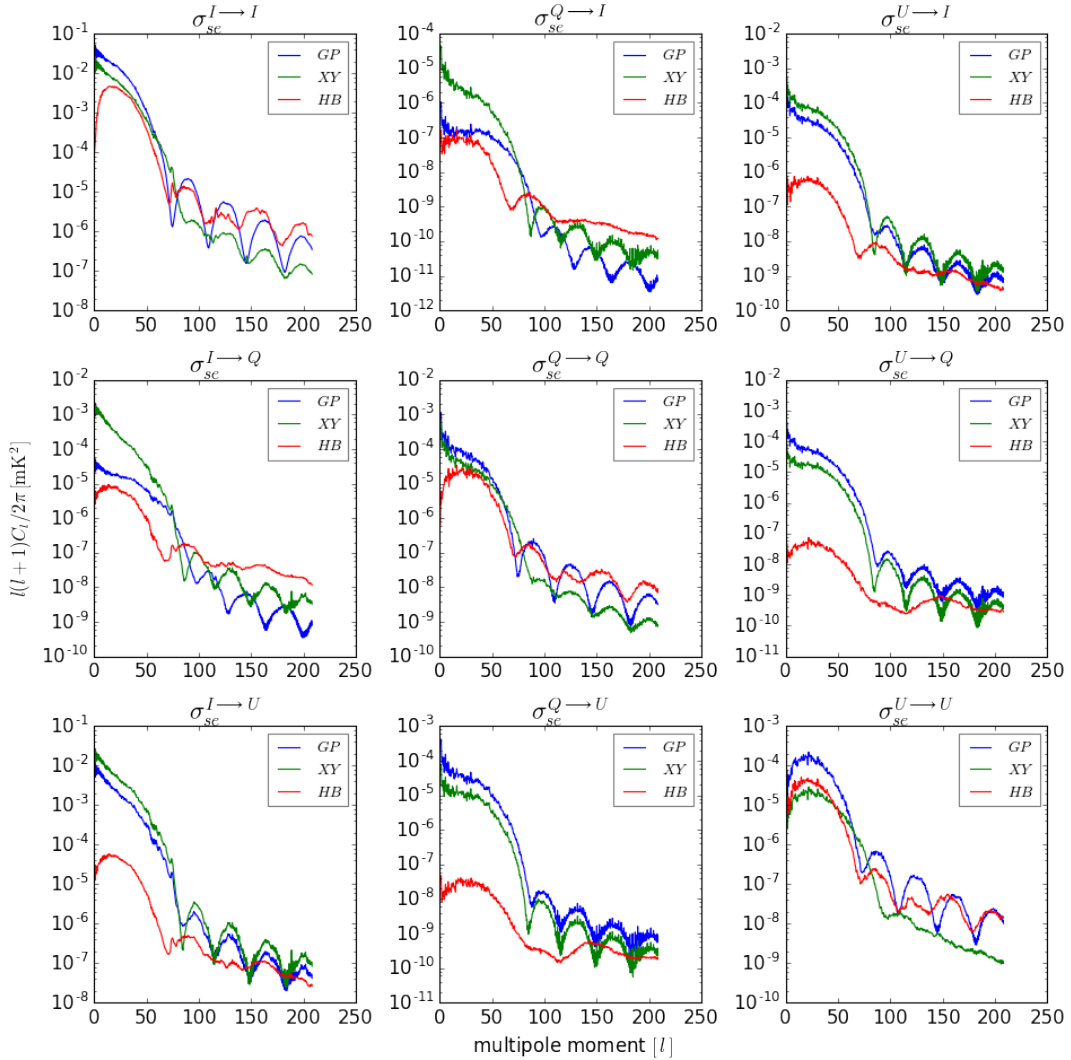


Figure 4.12: These are the spectra plots of the systematic errors in Fig. 4.6. The notations GP and XY in the legends denote the residuals for gain-phase and dipole orientation errors in the OSKAR beams, that of HB depicts the errors in the holography beams. These errors are then used to estimate the imperfections in the simulation by computing the expected value of the standard deviations of the sampling distributions of the residual maps to produce Table A.1.

4.5 Conclusions

The study introduced a relatively cheaper technique to produce realistic primary beams of KAT-7 and perturbed these beams (using gain, phase and dipole orientation errors) for intensity mapping experiments. These fully polarised modelled beams are then used to simulate the full-sky polarisation maps by the method of convolution in order to compute the intensities of the diffused Galactic foregrounds and determine the amount of signals that have seeped from linear polarisation into total intensity. The simulation is repeated using the JVLA holography measured beams and then compared with the modelled beam simulation in

order to estimate the error introduced in the power spectrum when modelled beams are used. The following are the key findings of the research:

- The fractional error introduced in the convolved power spectrum estimation for assuming modelled beams to measured beams are 0.08% for Stokes I , 0.03% for Q and 0.07% for U . This is due to the imperfections in the nominal orientation of the dipoles which describe the distribution of the KAT-7 dish-like surface. Our beam modelling showed that there is 0.10% perturbed inaccuracies on the dish surface.
- If we construct a model of a beam and then carry out polarisation rotation and calibration of the phase in order to correct the beam in Stokes I then, the level of leakage to get in Stokes I is $\approx 10^{-2}$ mK 2 , given the lack of knowledge of the beam. But, if we don't do any correction at all from the beam then, the kind of leakage we get is $\approx 10^{-1}$ mK 2 .
- Furthermore, the power of the HI signal can be estimated at a moment of $l = 25$ when the beam is corrected in Stokes I (i.e., $Q \rightarrow I$, $U \rightarrow I$ and $I \rightarrow I$) and at a moment of $l = 100$ without any beam correction. This makes the latter moment to be > 2 orders of magnitude higher than when we correct the error in the beam.
- Finally, if a true model of the beam is assumed, then the fractional leakage of the intrinsic $|Q + iU|_T \rightarrow I$ is $\approx 1.0\%$, hence, making it possible to measure the power spectrum of the 21-cm signal at a multipole moment of $l = 25$ which conforms to when we correct the beam error in Stokes I .

In summary, the outputs of this research have shown how OSKAR can be used for beam pattern simulations, especially for large aperture arrays like those envisaged for the SKA. Hence, with the fully polarised modelled beams produced from OSKAR and the convolution technique for foregrounds simulations, we can estimate the amount of foregrounds that had leaked from intensity into polarisation and vice-versa. Our future work is to implement a similar approach with MeerKAT holography measured beams to investigate HI intensity mapping observation.

Chapter 5

MeerKAT L-Band Primary Beams: Effects of HI Intensity Mapping

Overview

This Chapter introduces us to Zernike model and how it can be used to reconstruct a realistic beam model using the strongest coefficients with corresponding basis patterns. Intensity mapping experiment is performed with these primary beams to evaluate the angular power spectrum of 21 cm signal.

5.1 Introduction

Image reconstruction produced from an original data is an inverse problem. Usually, it is difficult to explicitly solve the inverse problem directly. To overcome this difficulty, many orthogonal moment based feature extraction methods such as Zernike Moments (ZM) (Goswami and Prasad 2013; Thuong et al. 2015; Teague 1980), Krawtchouk moments (Clemente et al. 2017; Yap, Paramesran, and Ong 2003), Legendre Moments (LM) (Zhang et al. 2010; Yap and Raveendran 2005), Tchebichef moments (Mukundan, Ong, and Lee 2001; Shu et al. 2010), etc., have been introduced into image analysis and achieved great success. The analysis in (Wu et al. 2017; D’Angelo and Rampone 2016; Zhang and Lu 2004) shows that the moments based feature representations own some advantages such as compact representation, robustness to noise, invariance properties (i.e. rotation, scale and translation) and low computational as well as storage costs. In this research, ZM method is used to reconstruct the image since, apart from the previous advantages given, the number of coefficients used to reconstruct the image are independent of the number of Zernike polynomials used in the sequence. This condition of independence or orthogonality, means that any number of additional terms can

be added without impact on those already computed.

This chapter further explores how the IM techniques discussed in chapter 4 scale to MeerKAT telescopes. Thus, instead of using OSKAR to simulate perturbed fully polarised beams, we fit Zernike polynomials to MeerKAT holography measured beams and then perturbed with the fit. We then simulate these reconstructed beams with the foregrounds to determine the leakage terms.

5.2 Methodology

5.2.1 Mathematical Basis of Zernike Polynomials

Consider a wavefront denoted by $\Phi_w(\rho, \theta)$, in polar coordinates (ρ, θ) , to be a linear combination of Zernike polynomials over a circular unit, then this phenomenon can mathematically be expressed as;

$$\Phi_w(\rho, \theta) = \sum_{n,m}^M C_n^m Z_n^m(\rho, \theta) \quad (5.1)$$

The *basis of Zernike moment* $Z_n^m(\rho, \theta)$, in equation 5.1 is defined as (Ferreira et al. 2015);

$$Z_n^m(\rho, \theta) = \begin{cases} N_n^m R_n^{|m|}(\rho) \cos(\rho m \theta), & m \geq 0 \\ -N_n^m R_n^{|m|}(\rho) \sin(\rho m \theta), & m < 0 \end{cases} \quad (5.2)$$

The *radial polynomial* $R_n^{|m|}(\rho)$ and the *normalisation factor* N_n^m in equation 5.2 are respectively denoted as: $R_n^{|m|}(\rho) = \sum_{s=0}^{\frac{n-|m|}{2}} (-1)^s \frac{(n-s)!}{s! (\frac{n+|m|}{2}-s)! (\frac{n-|m|}{2}-s)!} \rho^{n-2s}$, $N_n^m = \sqrt{\frac{2n+1}{1+\delta_{m,0}}}$

where $\delta_{m,0}$ is the Kronecker delta function such that $\delta_{0,0} = 1$ and $\delta_{m,0} = 0$ when $m \neq 0$. The index $n \geq 0$: $n = 0, 1, 2, \dots$ and for a specific n , the index m takes the values $m = -n, -n + 2, -n + 4, \dots, n$.

The Zernike polynomials $Z_n^m(\rho, \theta)$ are a set of complete orthogonal over a unit circle and this is conveniently represented in equation 5.2 as the products of angular functions and radial polynomials. The orthogonality of this function makes the coefficients not to be dependent on each other (Charman 2005; Wyant and Creath 1992) and hence, these coefficients are normally expressed in double (n, m) or single (j) modes. The n mode characterizes the order of aberration and mode m represents the azimuthal frequency of the sinusoidal. The radius parameter, denoted ρ , is continuous over the range of $(0, 1)$ and this means the azimuthal component is continuous over the range of θ , such that $0 \leq \theta \leq 2\pi$. Fig. 5.1 displays 8 of such radial responses, where it can clearly be observed that the polynomials converge as they approach the edge of the unit disc. This also confirms that, the Zernike polynomials of all orders are confined to the interval $(-1, 1)$ and therefore, can be used as basis functions of

image moments as shown in Fig. 5.2.

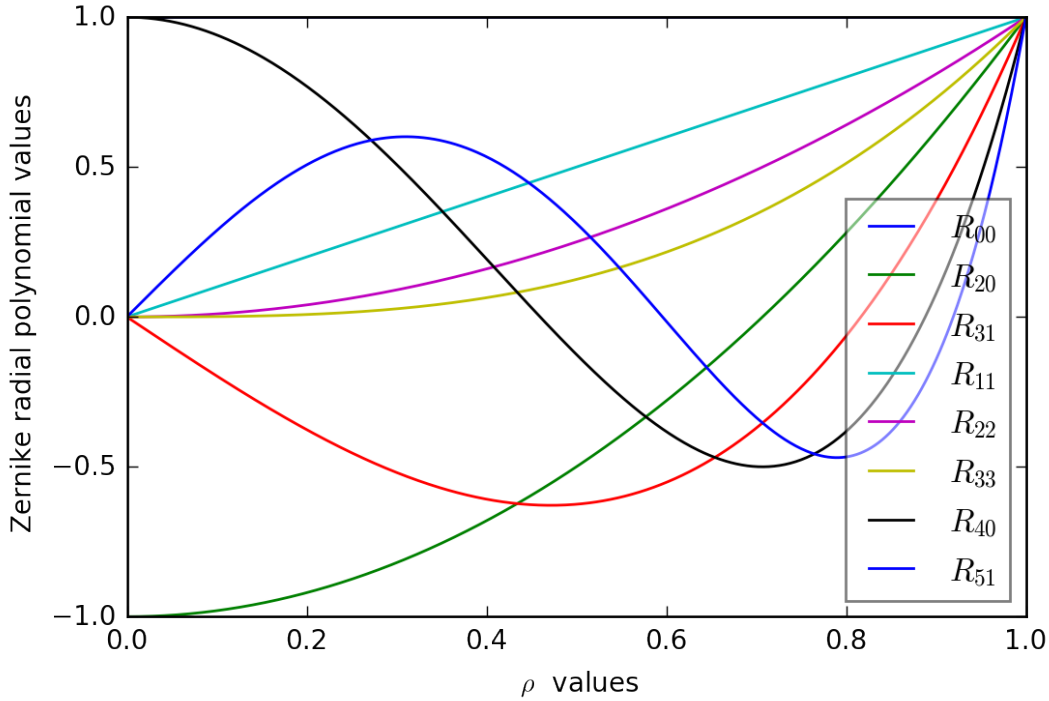


Figure 5.1: Expansion of eight orthogonal radial polynomial $R_n^{|m|}(\rho)$ plots. Here, the value of unity can be obtained at the outer edge, since $R_n^{|m|}(1) = 1$.

The surface plots in Fig. 5.2 depict the Zernike pyramid formed by the first 10 levels. In the central column, the modes are invariant by rotation (i.e. $m = 0$) and hence, the column can be seen as a symmetry around the axis. On each level (i.e. same n value), the Zernike modes of opposite azimuthal frequency value have the same overall shape, but a different orientation. These pairs are required to enable any mode to be freely oriented around 360° , by selectively adjusting the weight of each mode to obtain the desired orientation.

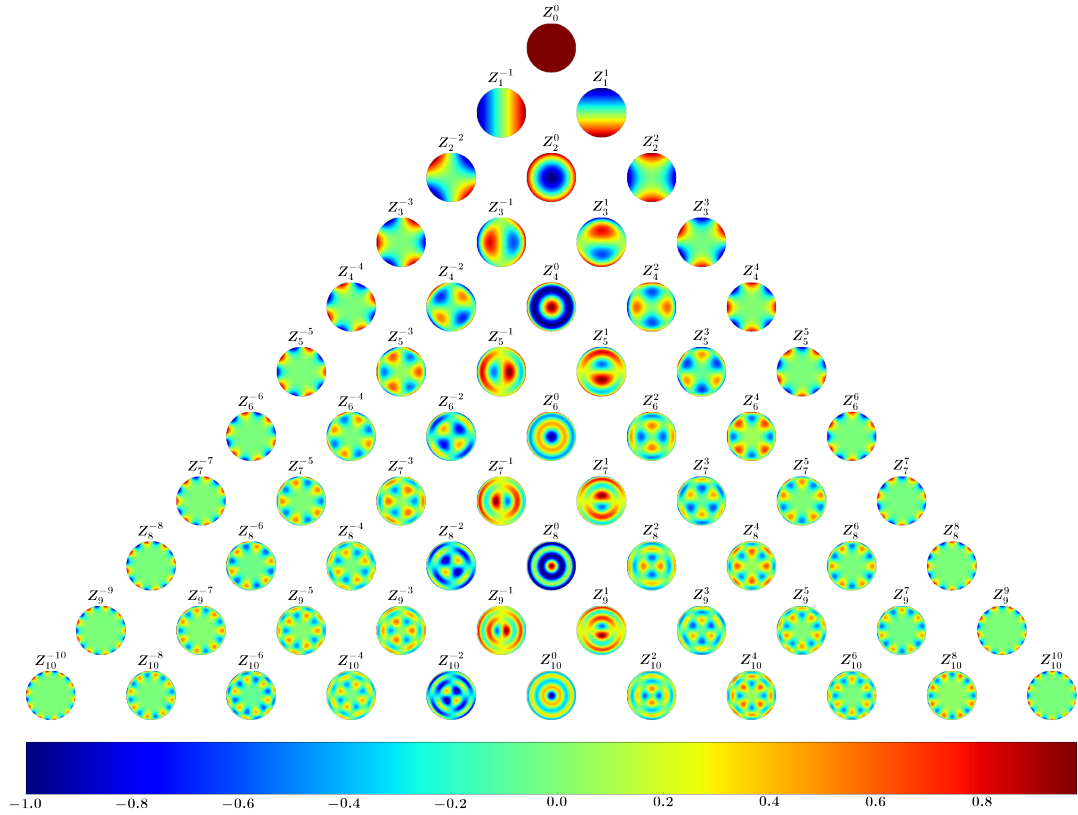


Figure 5.2: Representation of basis patterns of Zernike moments $Z_n^m(\rho, \theta)$ of order 10, plotted on a unit circle.

Occasionally, a single mode scheme is used to describe the Zernike expansion coefficients (Noll 1976; Wyant and Creath 1992). Since the polynomials depend upon two parameters n and m , ordering of a single mode scheme is arbitrary. To obtain the single mode j , it is convenient to lay out the polynomials in a pyramid with row number n and column number m . The single mode, j , starts at the top and the corresponding single indexing scheme, with index variable j , is shown in Table 5.1. In the single mode scheme, we have;

$$Z_j(\rho, \theta) = Z_n^m(\rho, \theta) \quad (5.3)$$

where $j = \frac{n(n+2)+m}{2}$, $n = \left\lceil \frac{-3+\sqrt{(9+8j)}}{2} \right\rceil$ and $m = 2j - n(n+2)$. The special bracket notation $\lceil . \rceil$ corresponds to the ceil function.

Table 5.1: Relationship between single and double index schemes to third order.

Radial order, n	Angular frequency, m						
	-3	-2	-1	0	1	2	3
0				$j = 0$			
1			$j = 1$		$j = 2$		
2		$j = 3$		$j = 4$		$j = 5$	
3		$j = 6$		$j = 7$		$j = 8$	$j = 9$

In this research, we will deal exclusively with the double indexed Zernike polynomials as portrayed by Campbell 2003; Lakshminarayanan and Fleck 2011.

5.2.2 Orthonormality

The orthonormality of the Zernike polynomials of modes (n, m) and (n', m') can be expressed as:

$$\frac{\int_0^1 \int_0^{2\pi} Z_n^m(\rho, \theta) Z_{n'}^{m'}(\rho, \theta) \rho d\rho d\theta}{\int_0^1 \int_0^{2\pi} \rho d\rho d\theta} = \delta_{nn'} \quad (5.4)$$

where $\delta_{nn'} = \begin{cases} 1 & \text{if } n = n' \\ 0 & \text{if } n \neq n' \end{cases}$. The function in equation 5.4 can be defined in radial orthogonality term as:

$$\int_0^1 R_n^m(\rho, \theta) R_{n'}^{m'}(\rho, \theta) \rho d\rho = \frac{1}{2(n+1)} \delta_{nn'} \quad (5.5)$$

and angular orthogonality term as:

$$\int_0^{2\pi} d\theta \begin{cases} \cos m\theta \cos m'\theta \\ \sin m\theta \sin m'\theta \\ \cos m\theta \sin m'\theta \\ \sin m\theta \cos m'\theta \end{cases} = \begin{cases} \pi(1 + \delta_{m0}) \delta_{mm'} \\ \pi \delta_{mm'} \\ 0 \\ 0 \end{cases} \quad (5.6)$$

5.2.3 Numerical Computation of Zernike Coefficients

Equation (5.1) shows the global fitting system of the Zernike representation; that is, the complete data approximated by a definite function of some degree k . Now, assume L discrete data points are given from the measured wavefront, denoted as $\Phi_w^\tau(\rho_\tau, \theta_\tau) |_{\tau=1,2,3,\dots,L}$, where (ρ_τ, θ_τ) are the normalised 2D polar coordinates and Φ_w^τ are the corresponding wavefront values. The only unknown parameters in equation (5.1) are the Zernike coefficients C_n^m . This section estimates the parameters of C_n^m by rewriting equation (5.1) in a simple form as expressed in equation (5.7) and then solve the least square problem using the matrix inversion approach.

$$\mathbf{Z} \mathbf{c} = \boldsymbol{\Phi} \quad (5.7)$$

where $\boldsymbol{\Phi}$ is the $L \times 1$ data array that is made up of the sampled wavefront values, \mathbf{c} is the $P \times 1$ array containing the Zernike coefficients and \mathbf{Z} is the $P \times L$ matrix containing the values of the Zernike polynomials in each sampling point. Expanding equation (5.7) we get;

$$\begin{pmatrix} Z_1(\rho_1, \theta_1) & Z_2(\rho_1, \theta_1) & \cdots & Z_P(\rho_1, \theta_1) \\ Z_1(\rho_2, \theta_2) & Z_2(\rho_2, \theta_2) & \cdots & Z_P(\rho_2, \theta_2) \\ \vdots & \vdots & \ddots & \vdots \\ Z_1(\rho_L, \theta_L) & Z_2(\rho_L, \theta_L) & \cdots & Z_P(\rho_L, \theta_L) \end{pmatrix} \begin{pmatrix} c_1 \\ c_2 \\ \vdots \\ c_L \end{pmatrix} = \begin{pmatrix} \Phi(\rho_1, \theta_1) \\ \Phi(\rho_2, \theta_2) \\ \vdots \\ \Phi(\rho_L, \theta_L) \end{pmatrix} \quad (5.8)$$

The resultant equation can be written in the form;

$$\mathbf{Z}^T \mathbf{Z} \mathbf{c} = \mathbf{Z}^T \boldsymbol{\Phi} \quad (5.9)$$

such that, the desired Zernike coefficients can be obtained by direct inversion;

$$\mathbf{c} = (\mathbf{Z}^T \mathbf{Z})^{-1} \mathbf{Z}^T \boldsymbol{\Phi} \quad (5.10)$$

Therefore, given the basis patterns of Zernike polynomials and the corresponding coefficients, we can use these to reconstruct a particular wavefront.

In this study, the MeerKAT holography primary beams are used to represent the wavefront and then fit Zernike polynomials to reconstruct the measured beams. In Figs. 5.3 and 5.4, we used Zernike coefficients to show the spectra plots of MeerKAT beams in both magnitude and phase respectively. The idea behind this is to understand the signal distribution over frequency components and to be able to interpolate for the missing channels due to high RFI in these measured beams. The magnitude spectral plots in Fig. 5.3 display the 6 strongest Zernike coefficients and the corresponding activated basis patterns used for the reconstruction over a range of frequencies [900, 1700] MHz. The diagonal parts of these plots represent the

gain terms (i.e. XX and YY) of the Jones matrix whilst the cross terms (i.e. XY and YX) are represented in the off-diagonal parts. The activated basis patterns used to construct the amplitude of the gain terms are 11, 22, 1, 4, 37, 56 (for both XX and YY) and that of XY and YX are 13, 23, 39, 29, 5, 17 and 13, 5, 30, 23, 16, 39 respectively. The bad channels due to high RFI are corrected by interpolating the good channels with Discrete Cosine Transform (DCT) defined in equation (5.11) to find the missing channels.

$$X_k = \sqrt{\frac{2}{N}} s(k) \sum_{n=0}^{N-1} x_n \cos \left[\frac{\pi}{N} (n + 0.5) k \right] \quad (5.11)$$

where X is the DCT output, x is the input, k is the index of the output coefficients being calculated from the range of $[0, N - 1]$ and s is a scaling function such that

$$s_k = \begin{cases} \frac{1}{\sqrt{2}} & \text{if } \zeta = 0 \\ 1 & \text{if otherwise} \end{cases} .$$

Similarly, in Fig. 5.4, we apply the same approach to produce the spectral plots for the phase. Here, the missing channels are reconstructed by taking the Sine and Cosine of the imaginary and real parts of the Jones terms accordingly. Note how the DCT and Sine/Cosine functions actually predicted the Zernike coefficients model.

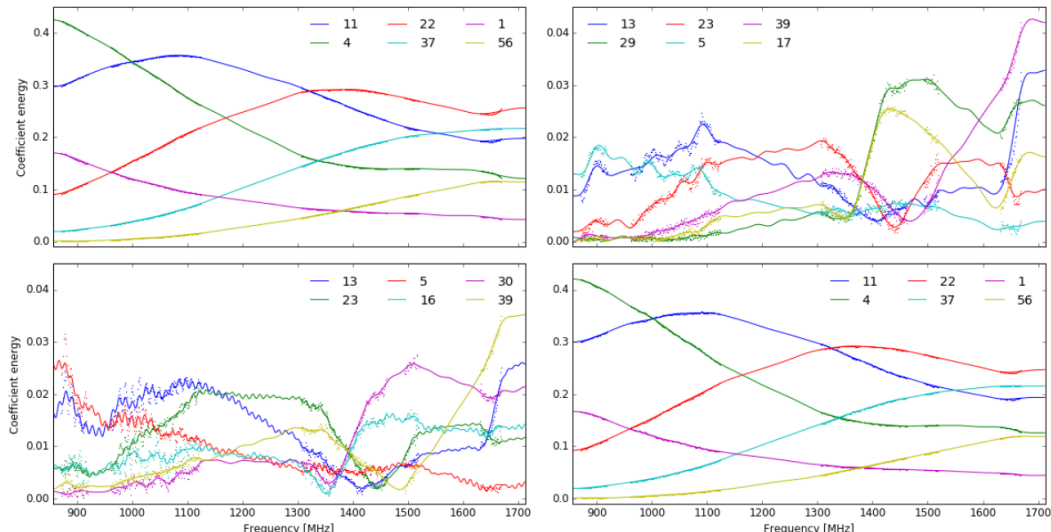


Figure 5.3: Spectral representation of the amplitude of MeerKAT primary beams for L band. The dotted lines are the Zernike plots with missing frequency channels due to high RFI whilst the solid lines are the DCT plots used to correct the bad channels for the respective Jones terms [XX (top-left), XY (top-right), YX (bottom-left), YY (bottom-right)].

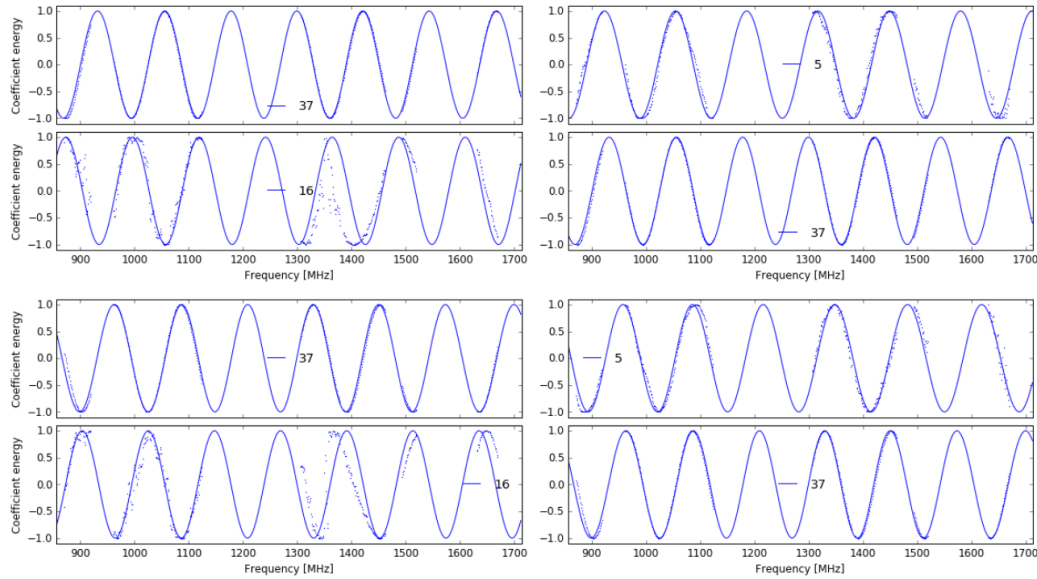


Figure 5.4: Spectral representation of the phase of MeerKAT primary beams for L band. The dotted lines are the Zernike plots with missing frequency channels due to high RFI whilst the solid lines are the Sine (top) and Cosine (bottom) plots used to correct the bad channels for the respective Jones terms [XX (top-left), XY (top-right), YX (bottom-left), YY (bottom-right)].

The next section extends the spectral plots to a complete reconstructed 2D image and then try to perturb the image with Zernike fits.

5.2.4 Spatial Representation

As mentioned in section 5.2.3, to reconstruct a 2D image from a Zernike fit, all we need to have are the coefficients and the respective basis functions. If we use less number of coefficients, there's the possibility that the modelled image will not be well fitted. In addition, if the number of coefficients are very high, there's the likelihood of over fitting the modelled image. In this section, we choose a realistic number by using the strongest number of coefficients with the corresponding basis functions to model the fitted MeerKAT beams. We can achieve this by varying in terms of increasing or decreasing the strongest number of coefficients to determine which of these are less perturbed.

Fig. 5.5 shows a reconstructed MeerKAT beam model at a frequency of 990 MHz. Note how the Zernike modelled beams (middle plots) have de-noised the original beams. These modelled beams are produced using 20 strongest coefficients for the gain terms (Jones XX and YY) and 5 strongest coefficients for the cross terms (Jones XY and YX). To test the goodness of fit of this model, we vary the number of Zernike coefficients and compare their residuals. The 1st 2 plots in Fig. 5.6 are the radial profile plots when we use 5 strongest coefficients for all the Jones terms and 10 strongest coefficients for all the Jones terms respectively. Note how the standard errors of these plots are higher than the 3rd plots which occur when we

use the coefficients of 20 and 5 for the gain and cross terms respectively. This is confirmed when we also look at the distribution of the histogram plots in Fig. 5.7. Using > 5 strongest coefficients to model the cross terms and < 20 strongest coefficients to model the gain terms will result in the perturbation of the beams.

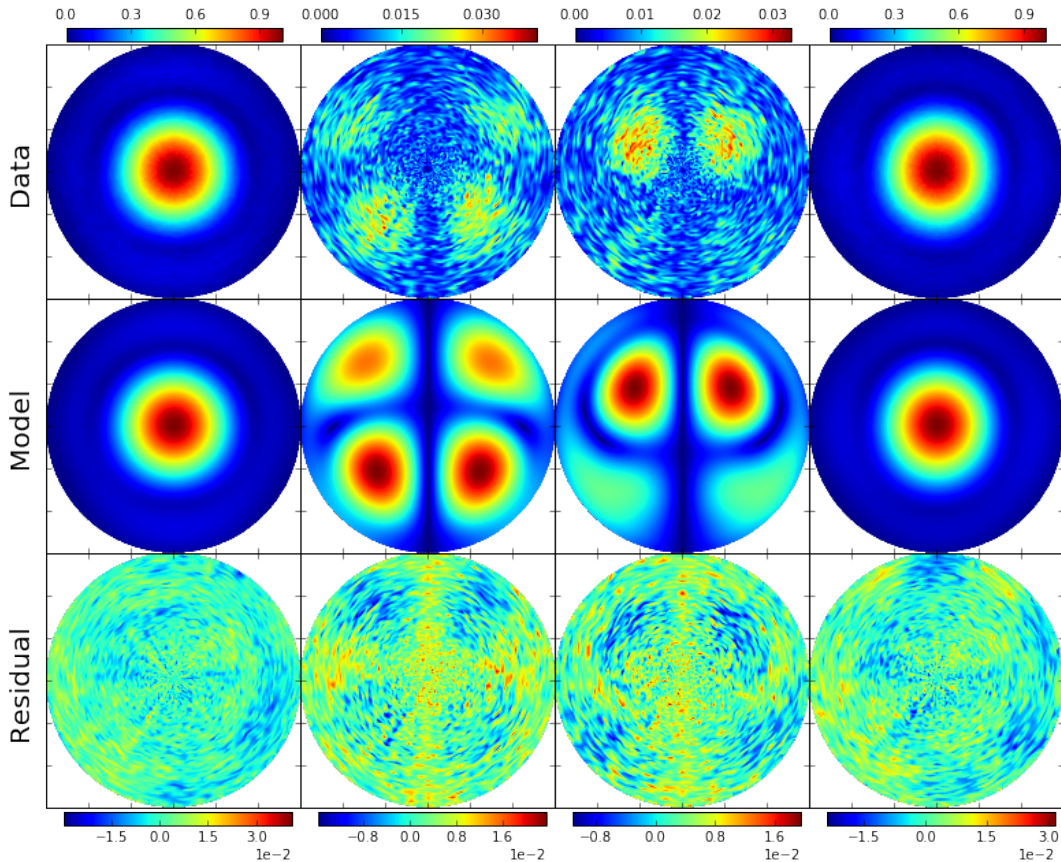


Figure 5.5: Zernike reconstructed MeerKAT beam model at 990 MHz, using 20 and 5 strongest coefficients to model the gain and cross components respectively.

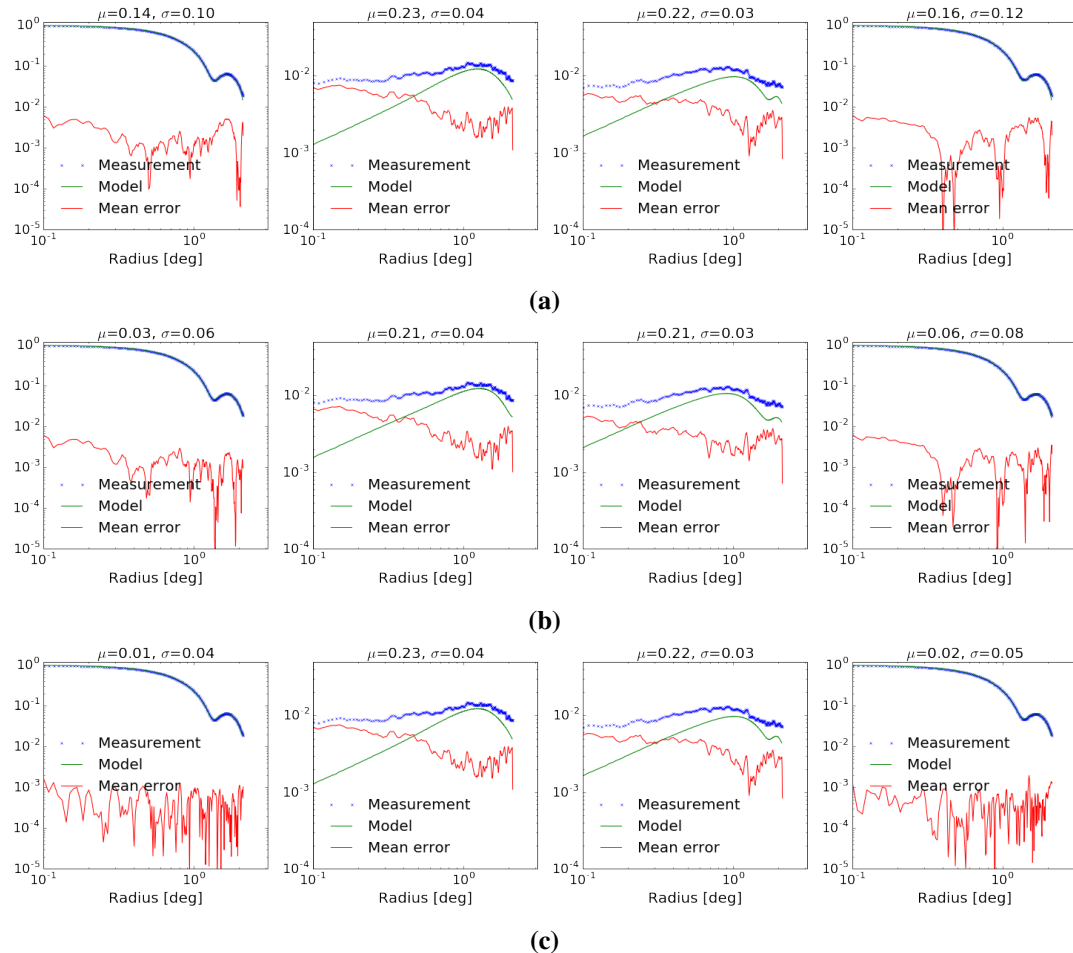


Figure 5.6: Radial profile of Fig. 5.5. (a) Using 5 strongest zernike coefficients for the Jones components. (b) Using 10 strongest zernike coefficients for the Jones components. (c) Using 20 strongest zernike coefficients for the gain components and 5 strongest zernike coefficients for the cross components.

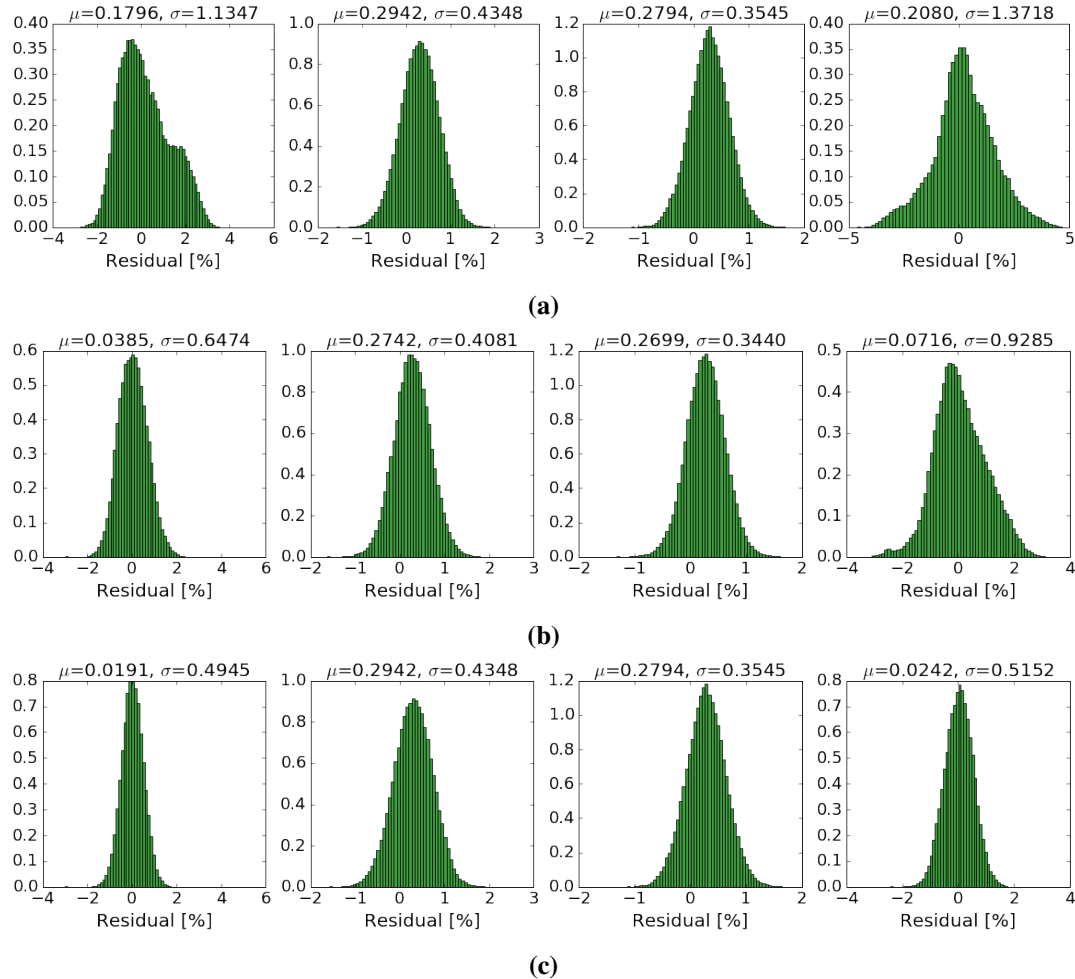


Figure 5.7: Histogram plots showing the residual distribution. (a) Plots obtained from using 5 strongest zernike coefficients for the Jones components. (b) Plots obtained from using 10 strongest zernike coefficients for the Jones components. (c) Plots obtained from using 20 strongest zernike coefficients for the gain components and 5 strongest zernike coefficients for the cross components.

We now discuss the results obtained when we simulate the foregrounds with the above modelled beams to compute the polarisation leakage when performing IM experiment.

5.3 Results and Discussion

The spectra plots reported in Fig. 5.8 justify the reason why the research focused on the selected Zernike coefficients to reconstruct the MeerKAT beams. The plots represent the standard deviation of the differences between predicted Zernike values and observed holography values at different number of Zernike coefficients. The gain plots (for XX and YY in Fig. 5.8) clearly show that the 20 strongest Zernike coefficients used to model the XX and YY beams are realistic since increasing the number of coefficients will not significantly improve the

reconstructed model. The same explanation goes to the cross term plots (for XY and YX in Fig. 5.8) when we used the 5 strongest Zernike coefficients to reconstruct.

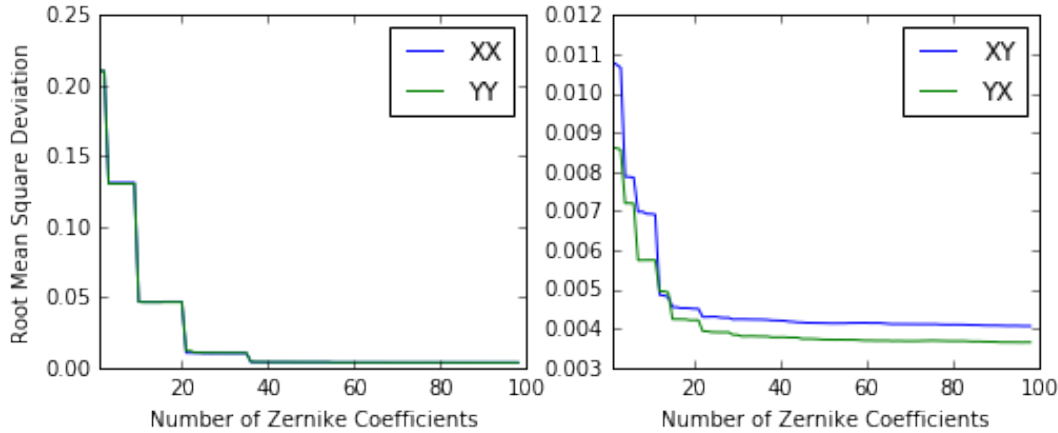


Figure 5.8: The expected value of the squared error loss between the holography beam and the predicted beam model with increase in the number of Zernike coefficients.

The convolved maps presented in Fig. 5.9 is a repetition of the simulation we discussed in Section 4.3.1. Here the reconstructed MeerKAT primary beams are transformed from the Jones terms into complete Mueller beams. These Mueller beams are then used to convolve the foregrounds maps in Fig. 3.4. The 1st row is the true measured maps when the modelled beams used are constructed with 20 and 5 strongest coefficients for the gain and cross terms respectively. The next 2 rows are the perturbed measured maps when we fully model the beams with 5 and 10 Zernike coefficients in a respective manner. The remaining rows are the error maps between the true and the perturbed measured maps. Note carefully how these scaled measured maps (both true and perturbed) are very similar but the actual differences are shown in the error maps.

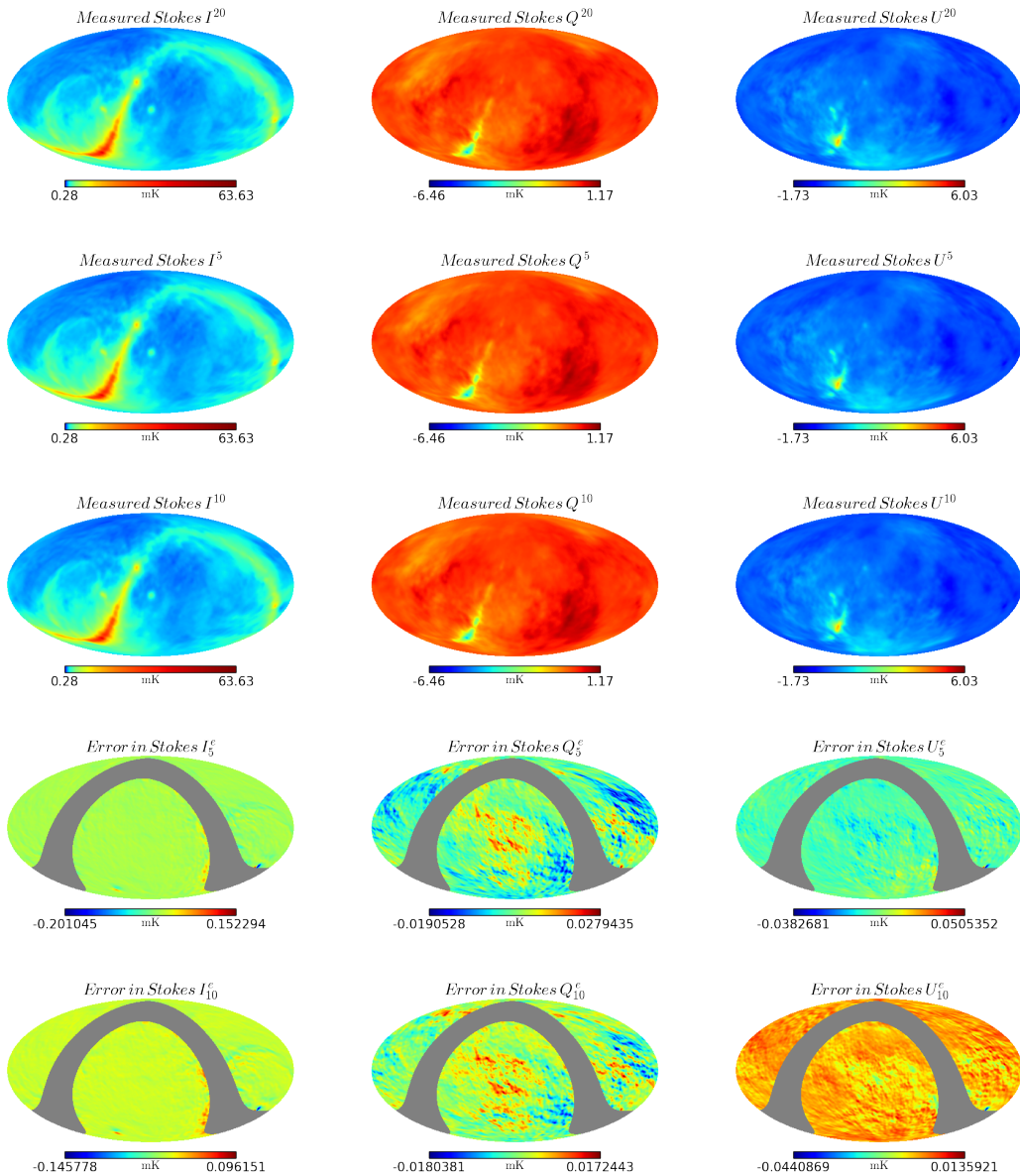


Figure 5.9: Measured Stokes I, Q and U convolved with reconstructed MeerKAT beam models with corresponding error maps.

The spectra plots displayed in Fig. 5.10 show how the HI signal power is estimated when we correct the errors in the reconstructed beams and vice versa. If the errors in the reconstructed beams are corrected in Stokes I as shown in the left plot, then the HI signal power is estimated at a multipole moment of $l \simeq 25$ and if the error is not corrected at all in Stokes I but the intrinsic polarisation leakage ($|Q + iU|_z$) in I is known, then the HI signal power is estimated at a multipole moment of $l \simeq 100$. This multipole moment is about 4 orders of magnitude greater at lower scales. However, if the intrinsic $|Q + iU|_z \rightarrow I$ is corrected, then the HI signal power is evaluated at a multipole moment of $l \simeq 50$. This multipole moment is about 2 orders of magnitude greater at lower scales.

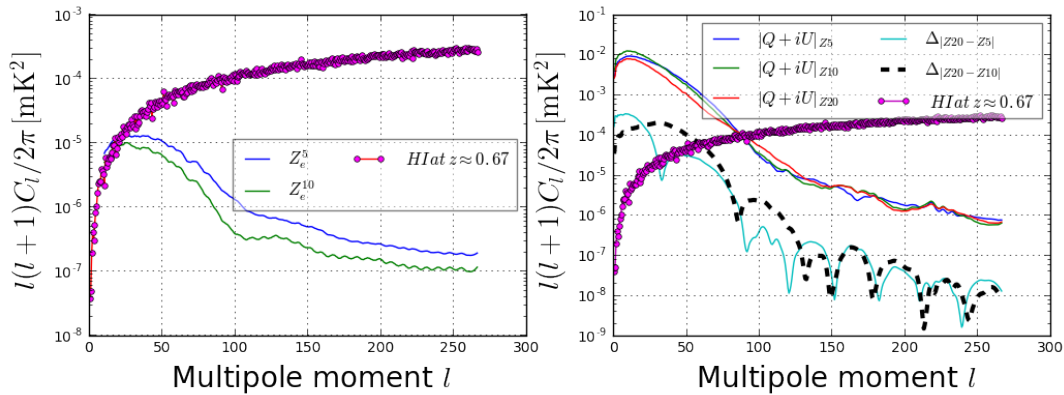


Figure 5.10: The distribution of angular power plots displaying the errors due to perturbed Zernike fits in Stokes I map (left plots) and the intrinsic leakage in I (right plots) affect the 21 cm signal (solid circular spectrum plot).

5.4 Conclusion

This chapter has clearly shown that Zernike polynomial is a very good fitting model for IM experiments. The fitting model was able to reconstruct the MeerKAT L-band holography measured beams. The reconstruction of the true modelled beam was done by using sufficiently enough strongest Zernike coefficients and the corresponding basis functions. In order to distort the true modelled beams, the study used more and less strongest Zernike coefficients with the respective basis functions to perturb the modelled beams. In addition, to measure the HI signal power spectrum, the study performed IM experiment by convolving these modelled beams with the foregrounds of the sky. The following are the key outcomes in this research:

- The true modelled beams were reconstructed with 20 strongest Zernike coefficients for the gain terms of the Jones matrix (XX and YY) and 5 strongest coefficients for the cross terms of the Jones matrix (XY and YX). The maximum standard error obtained from the reconstruction is $\simeq 0.05$.
- The corrupted modelled beams were generated with 5 strongest coefficients for all the Jones matrix terms (XX, XY, YX and YY). The second distortion was done with 10 strongest coefficients for all the Jones matrix terms (XX, XY, YX and YY). The maximum standard errors obtained are 0.12 (for using 5 strongest coefficients) and 0.08 (for using 10 strongest coefficients).
- The HI signal power is measured at a multipole moment of $l \simeq 25$ if we correct the beam errors in Stokes I and at a multipole moment of $l \simeq 100$ if we do not correct the beam errors in I .

In summary, with a good Zernike model of the primary beams, we can actually measure the amount of foregrounds that have leaked from intensity into polarisation.

Chapter 6

SKA1-mid Multiband Primary Beams: Effects of HI and CO Intensity Mapping

Overview

This chapter describes IXR is a measure of how numerically stable the true polarization can be recovered from measured antenna voltages... .

6.1 Introduction

6.1.1 SKA1-mid

The SKA1-mid instrument will be made up of a 150 km diameter array of reflector antennas (“dishes”). The interferometer will be a combination of 133 15 m SKA1 dishes and 64 13.5 m diameter dishes from the MeerKAT telescope. The radio telescopes will be systematised in a moderately dense core with a diameter of ~ 1 km, a further 2D array of randomly placed dishes out to ~ 3 km radius, thinning at the edges. Three spiral arms will widen to a radius of ~ 80 km from the centre. The reflector antennas will be offset-Gregorian optics design with clear-aperture capable of managing five low-noise front-end packages, each of which can be moved into the focal position. Except for the Band 1 receiver where the front-ends will be cyro-cooled. These reflector antennas will be able to operate up to 20 GHz, even though initially equipped to observe only up to 13.8 GHz for SKA1.

Primarily, the SKA1-mid will address observations of radio pulsars and observations of the 21 cm hyperfine line of neutral hydrogen from the local Universe, to moderate redshifts, as well

as high sensitivity observations of continuum emitting objects. It will also be well suited for conducting observations of various spectral lines in addition to the 21 cm hydrogen line, many classes of radio transients, magnetized plasmas both in the Galaxy and intergalactic space, and potentially proto-planetary disks. Although this instrument is not exclusively designed for IM experiments, it will be good to investigate its potential for this technique especially, for Bands 1, 2 and 5 receivers which will be the highest priority for the initial implementation of SKA1-mid, even though Bands 3 and 4 receivers will be provided as financial backing permits. For further details on the description and classification of SKA1 system refer to Chai et al. (2016) and Dewdney et al. (2015).

6.1.2 Line Intensity Mapping

The technique employed in IM experiment is to use the integrated emission from spectral lines in galaxies and /or diffuse IGM to track the growth and evolution of cosmic structure. This is essential to understand the spatial fluctuations in the line emission from many individually unresolved galaxies, rather than targeting galaxies one by one. Current dozens of researches on IM as stated in Chapter 1 promise new insights into the evolution of the Universe at low redshifts and into the Epoch of Re-ionization and Cosmic Dawn at high redshifts. The most generally spectral line discussed is the 21 cm neutral hydrogen line. However, other lines trace different physical processes, and some lines may be easier to study, either because they are brighter or they appear in a less difficult frequency band. Thus it is useful to study other lines in addition to the 21 cm line. Some other lines which have been proposed include the CII fine-structure line (Gong et al. 2012; Silva et al. 2015; Yue et al. 2015), Ly α line (Stark et al. 2017; Tapken et al. 2007; Zitrin et al. 2015) and the rotational CO lines (Lidz et al. 2011; Padmanabhan 2017; Vallini et al. 2017). Therefore, this chapter looks at IM of CO at high redshift in addition to HI at low redshift particularly, focusing on the observational effects of primary beam distortion of the SKA1-mid for band 1 (i.e. 350 – 1050 MHz), band 2 (i.e. 950 – 1760 MHz) and band 5a (i.e. 4.5 – 8.4 GHz). CO is a common tracer of molecular gas and star formation in nearby galaxies and also, the most dominant molecular species after H₂.

6.2 GRASP Beam Measurement

The GRASP software is a commercial package for the design and analysis of single and dual reflector antennas and also multi-reflector and multi-feed antennas. This section concentrates on the physical geometry and electromagnetic methods applied for the SKA1-mid analysis. A complete description of the GRASP package with mathematical expressions of the applied terms, explanations of the applied geometries and electromagnetic models as well as output data capabilities is given in the GRASP Technical Description, which may be retrieved from the Help Menu.

6.2.1 Model Specification

The simulation environment setup of the reflector and feed models is described in this section.

6.2.1.1 Reflector Antenna Models

Fig. 6.1 illustrates the dual reflector design of SKA1-mid. It consists of a regular or offset paraboloidal main reflector and a sub-reflector, with the feed horn placed at the principal focus. To design the dual reflector model shown in Fig. 6.1, the following parameters must be specified:

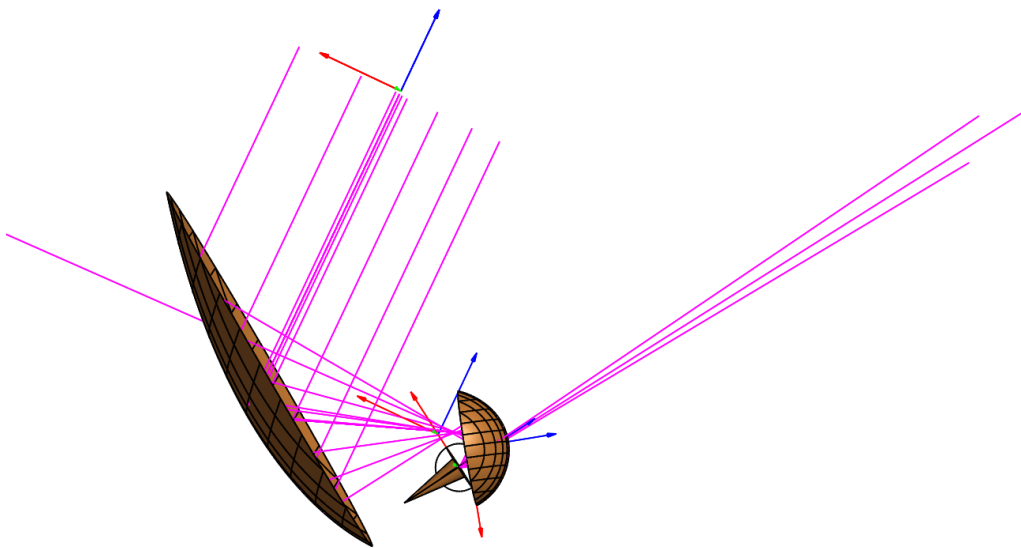


Figure 6.1: A geometrical dual reflector model of SKA1-mid oriented in the xz -direction and generating highly contoured beam.

- focal length of the reflector
- angle from the main reflector axis to the sub-reflector axis, measured positive in the anti-clockwise direction
- focal distance for the sub-reflector
- eccentricity for the sub-reflector
- angle from the sub-reflector axis to the feed axis, also measured positive in the anti-clockwise direction
- aperture diameter of the main reflector

- the wavelength of the operating frequency.

Either these parameters may be entered directly by the user or automated by means of the mouse. The automation will control the position of the feed and allow the user to obtain a wide range of designs in a flexible manner by altering the values of the parameters angle and the focal distance.

When these parameters are provided the design is constructed in the following way. The central ray from the feed, the direction of which is defined by the angles from the main reflector axis to the sub-reflector axis and from the sub-reflector axis to the feed axis, is reflected from the sub-reflector and hits the main reflector at a point which is selected as the centre for the circular main reflector aperture.

6.2.1.2 Feed Models

The feed system used in this chapter is an aperture illumination of the antenna system and this is possible in a receive situation. A general way to represent the illumination from a feed is through tabulated data from its beam pattern, which may come from measurements or calculations. The beam pattern data includes 2 or 3 polarization components depending whether the field is given in the far-field or in the near-field zones. The beam pattern of the feed used in the analysis is the measured far-field pattern, which consist of received fields on phi- and theta-plane.

6.2.1.3 Format of Input/Output Field Data

In GRASP 10.4.0, the class *spherical grid* projects both near- and far-field points in a 2D grid on a spherical surface. The 2D grid is described by the variables *X* and *Y* and has 5 forms of output coordinates as follows:

- *uv*: Here, $(X, Y) = (u, v)$, where *u* and *v* are the coordinates of the unit vector to the field point such that $\hat{r} = (u, v, \sqrt{1 - u^2 - v^2})$. *u* and *v* are unitless but are related to the spherical angles by $u = \sin \theta \cos \phi$, $v = \sin \theta \sin \phi$.
- $\theta\phi$: The θ and ϕ are angles in degrees and the regular spherical angles of the direction to the field point such that $(X, Y) = (\theta, \phi)$.
- *elevation over azimuth*: The coordinates $(X, Y) = (Az, El)$, where *Az* and *El* describe the direction to the field point by $\hat{r} = (\sin Az \cos El, \sin El, \cos Az \cos El)$. These coordinates are angles in degrees.
- *elevation and azimuth*: The coordinates $(X, Y) = (Az, El)$, where *Az* and *El* describe the direction to the field point by $Az = -\theta \cos \phi$, $El = \theta \sin \phi$. These coordinates are angles in degrees.

- *azimuth over elevation*: The coordinates $(X, Y) = (Az, El)$, where Az and El describe the direction to the field point by $\hat{r} = (\sin Az, \cos Az \sin El, \cos Az \cos El)$. These coordinates are also angles in degrees.

This research presented the 2D GRASP beam models shown in Figs. 6.5, 6.6 and 6.7 in the elevation-over-azimuth grid. For this output field data the direction to a field point can be pictured as a telescope mounted in an elevation-over-azimuth set-up at the origin of the x_0, y_0, z_0 -coordinate system. When (Az, El) are rotated, the telescope will phase at the field point given by (Az, El) and the grid will then have poles on the y_0 -axis.

The second class, Spherical Cut defines field points in cuts on a sphere where the field shall be calculated. Polar as well as conical cuts can be specified, both in the near-field and in the far-field region. Under this class, we use the parameter $theta_{range}$ to define the range of the polar angle θ and phi_{range} to define the range of the azimuthal angle ϕ and the number of points for both values. The more the number of cuts is, the finer the result becomes. However, this is also more computationally expensive. In this study, we perform a number of validation tests to determine the required number of cuts and the results are displayed in Figs. 6.2, 6.3 and 6.4. These spherical cut plots show the co- and cross polarisation far field patterns of SKA1-mid at various bands (i.e. 1, 2 and 5) and are presented in terms of discretization parameter, that is, the radial distance between the adjacent cuts over ϕ and θ .

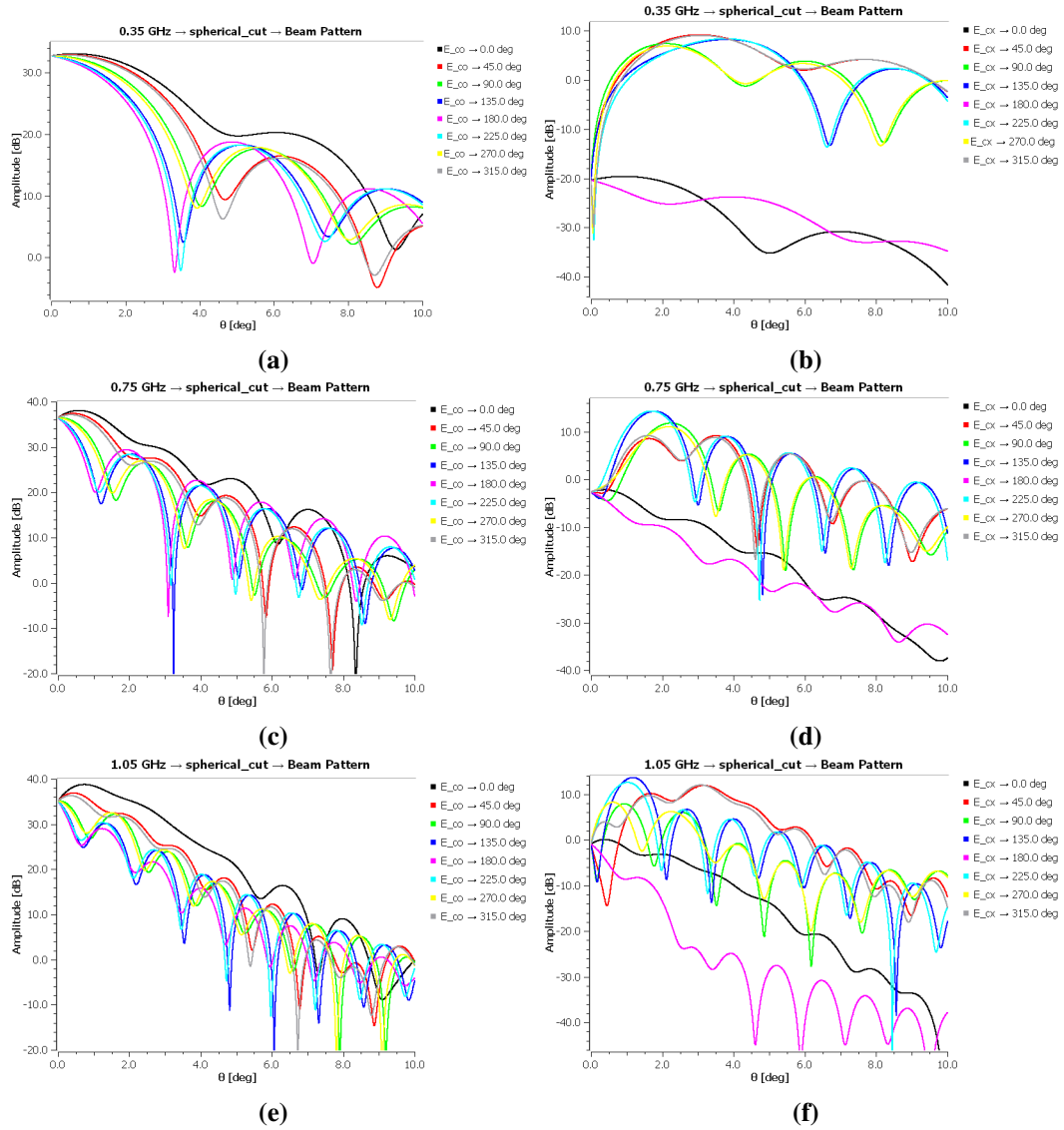


Figure 6.2: Far-field pattern cuts ($0^\circ \leq \phi \leq 315^\circ$) of the SKA1-mid showing the regions of the main, side lobes and cross polarisation levels for Band 1: Figs. 6.2a, 6.2c and 6.2e are the selected frequencies for the co-polar and that of the cross terms are Figs. 6.2b, 6.2d and 6.2f.

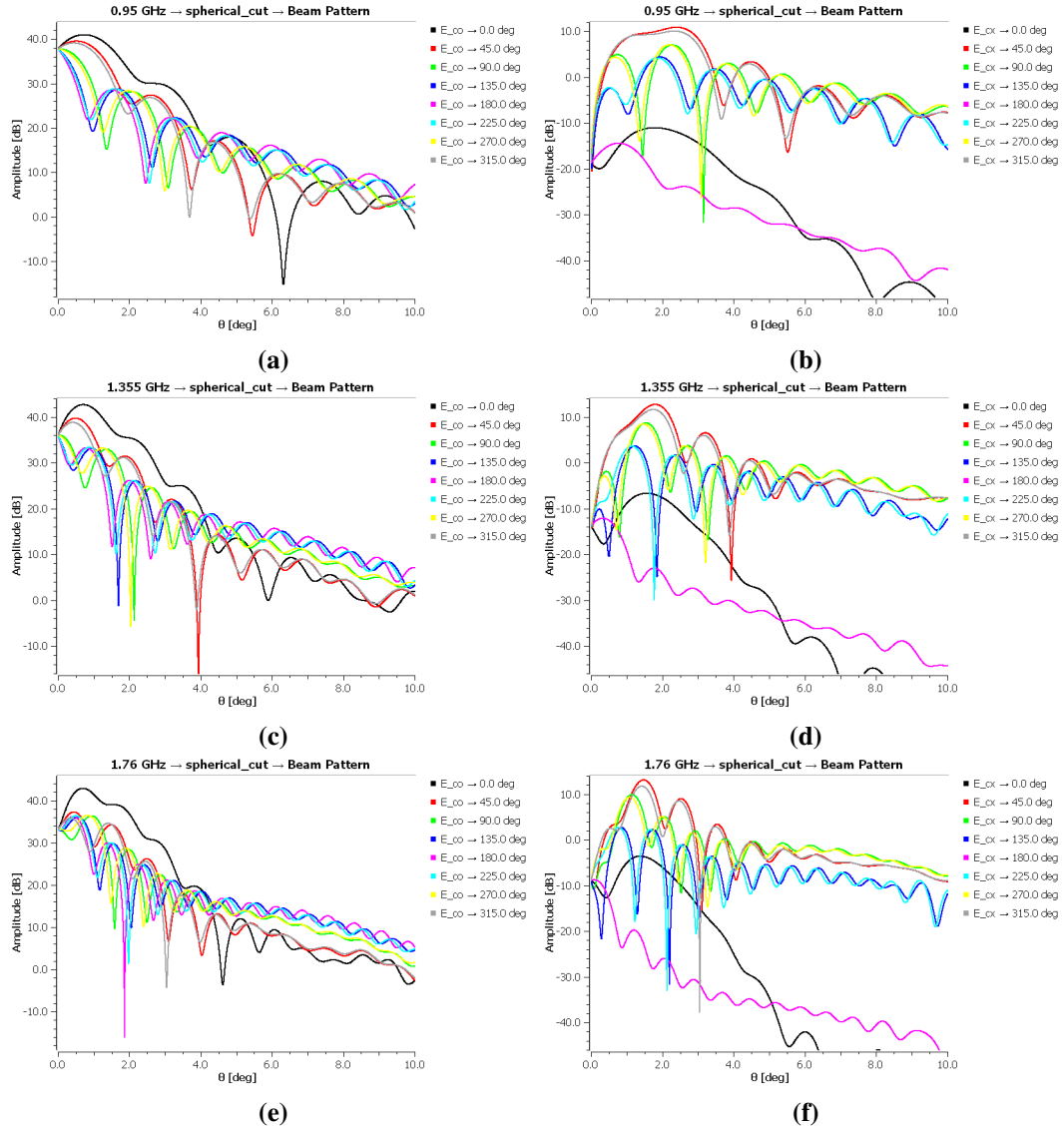


Figure 6.3: Far-field pattern cuts ($0^\circ \leq \phi \leq 315^\circ$) of the SKA1-mid showing the regions of the main, side lobes and cross polarisation levels for Band 2: Figs. 6.3a, 6.3c and 6.3e are the selected frequencies for the co-polar and that of the cross terms are Figs. 6.3b, 6.3d and 6.3f.

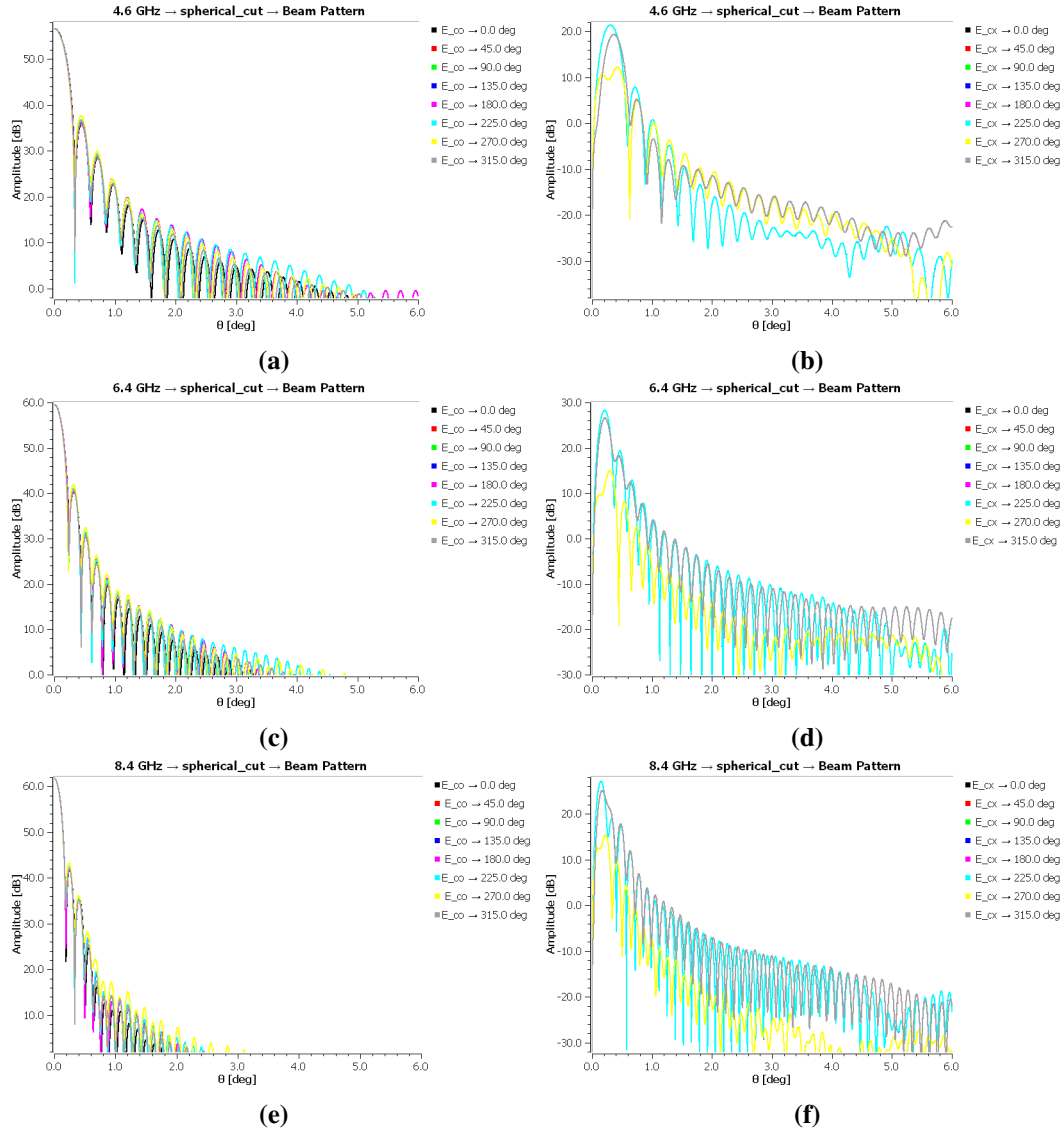


Figure 6.4: Far-field pattern cuts ($0^\circ \leq \phi \leq 315^\circ$) of the SKA1-mid showing the regions of the main, side lobes and cross polarization levels for Band 5: Figs. 6.4a, 6.4c and 6.4e are the selected frequencies for the co-polar and that of the cross terms are Figs. 6.4b, 6.4d and 6.4f.

The co- and cross-polarization level of amplitude (ρ) for Band 1 (refer to Fig. 6.2) at different spherical cuts are within the range of $(-20 \leq \rho \leq 40)$ dB and $(-40 \leq \rho \leq 10)$ dB respectively, that of Band 2 (refer to Fig. 6.3) are $(-10 \leq \rho \leq 40)$ dB and $(-40 \leq \rho \leq 10)$ dB respectively and then for Band 5 (refer to Fig. 6.4) we have $(0 \leq \rho \leq 60)$ dB and $(-20 \leq \rho \leq 30)$ dB respectively.

Section 6.2.2 briefly discusses the numerical techniques used to analysed the reflector antennas.

6.2.2 Numerical Analysis of Reflector Antennas

The numerical EM methods in GRASP which may be employed for the reflector analysis are:

- Physical Optics (PO)
- Physical Theory of Diffraction (PTD)
- Geometrical Optics (GO)
- Geometrical Theory of Diffraction (GTD)
- Spherical Wave Expansion (SWE)
- Plane Wave Expansion (PWE)
- Methods of Moments (MoM)

For our study we have employed a combined PO-PTD method. This method is applied to any number of reflector analyses in arbitrary manner, making it quite flexible to use because the induced currents obtained by a PO analysis on one reflector can be used as a source illuminating on a second reflector.

6.2.2.1 Physical Optics (PO)

Scattering problem is normally determined as a combination of a known incident field E_i and the field E_s from the scatterer with known geometry and electrical surface properties such that the total field E becomes;

$$E = E_i + E_s \quad (6.1)$$

The application of the principle of PO is such that, the local surface currents on the reflector are calculated as if a plane wave of the same direction, amplitude and phase was illuminating an infinite plane being the tangent plane to the surface at that point. When the reflector material is imperfectly conducting, it is appropriate to introduce both electric and magnetic surface currents. In this study, we have modeled the former case using the following steps to consider for the scattering analysis:

- (i) Compute the induced or equivalent surface currents (E_i). Here, the actual output of the surface currents can be obtained using the technique of MoM. However, for electrically large scatterers such as this work, the method is computationally expensive and therefore, the PO approximation of the induced currents can be used.
- (ii) Compute the field (E_s) radiated by these currents and scattered towards the direction of observation. This approach does not require any further approximations since the radiation integral of the surface currents can be computed by numerical integration with high accuracy.

- (iii) Sum the incident and the scattered field to obtain the total field E .

6.2.2.2 Physical Theory of Diffraction (PTD)

The PO currents approximate the induced currents on a scatterer derived from scattering by an infinite planar surface, that is, the unique behaviour of the currents close to an edge of the scatterer is not modelled by PO. In the PTD, the difference between the actual induced currents and the PO currents is approximated by considering the induced currents on an infinite perfectly conducting half plane illuminated by a plane wave. These PTD currents are therefore a correction to the PO currents such that the radiated PTD field is a correction which must be added to the PO field for obtaining the scattered field such that;

$$E_s \approx E_{PO} + E_{PTD} \quad (6.2)$$

6.3 Modelling EM Beams

Here, we try to reconstruct the GRASP beam models using Zernike fits and also, introduce errors in these GRASP beams for IM experiments.

6.3.1 Fitting 2D Zernike Polynomials on EM Beams

In this section, we employ the mathematical basis of Zernike polynomials discussed in chapter 5 to display both the spatial and spectral representations of the EM beams.

6.3.1.1 Spatial Representation

Figs. 6.5, 6.6 and 6.7 show the amplitude representation of the Zernike beam models for band 1, 2 and 5 respectively. Band 1 beams are reconstructed with 10 strongest Zernike coefficients and that of bands 2 and 5 can be reconstructed with 40 and 500 strongest Zernike coefficients accordingly. The high value of coefficients in band 5 is due to the increase in the number of side lobes in the beams, making IM at this band very difficult since we need at least 1000 Zernike coefficients with corresponding basis patterns to choose the strongest 500 coefficients from. After the reconstruction, the residual value obtained in the gain terms is ≈ 0.01 (for bands 1, 2 and 5), with that of the cross terms we have ≈ 0.0001 (for bands 1, 2 and 5).

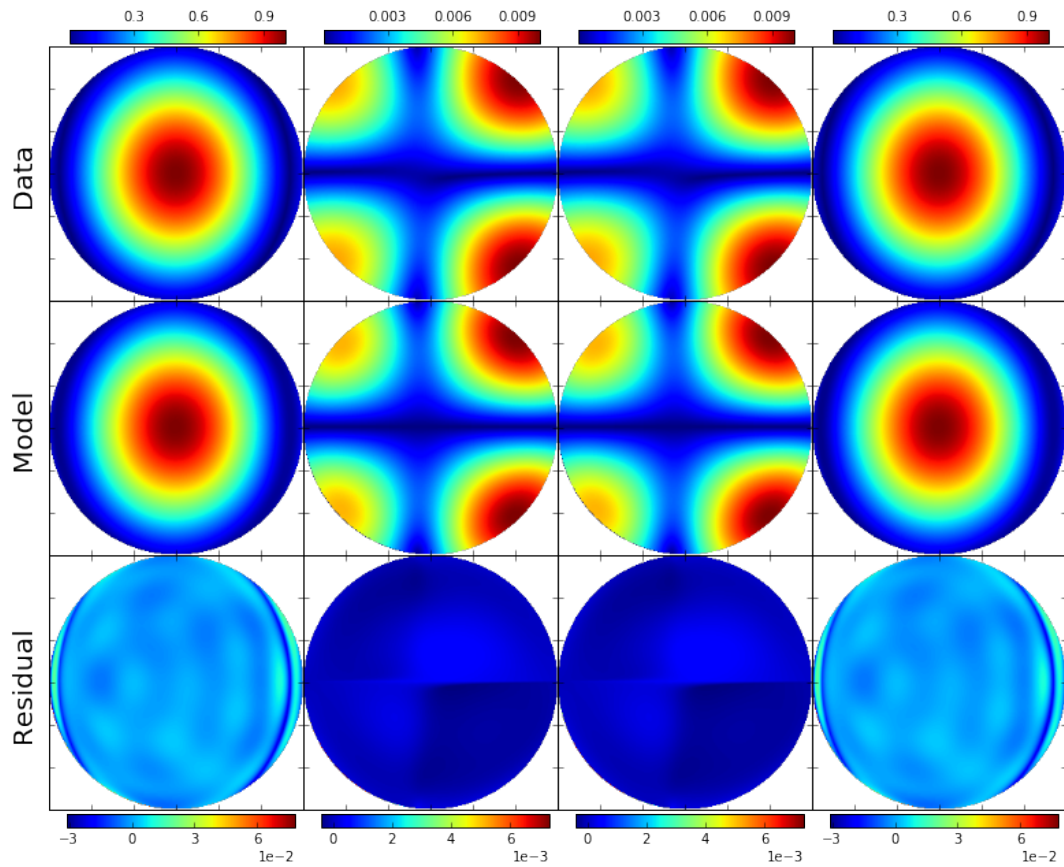


Figure 6.5: Zernike fit of band 1 EM beams at 450 MHz.

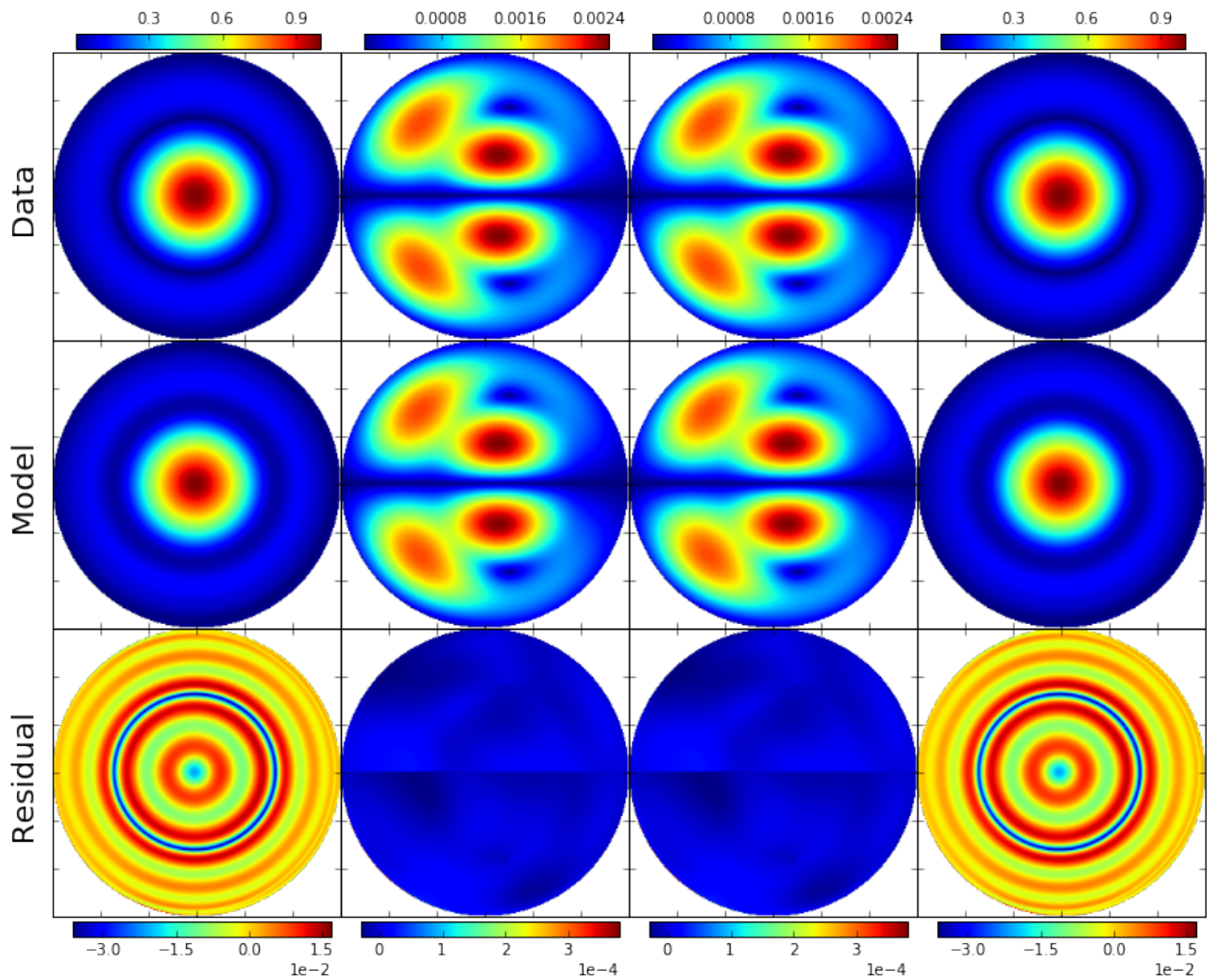


Figure 6.6: Zernike fit of band 2 EM beams at 990.5 MHz.

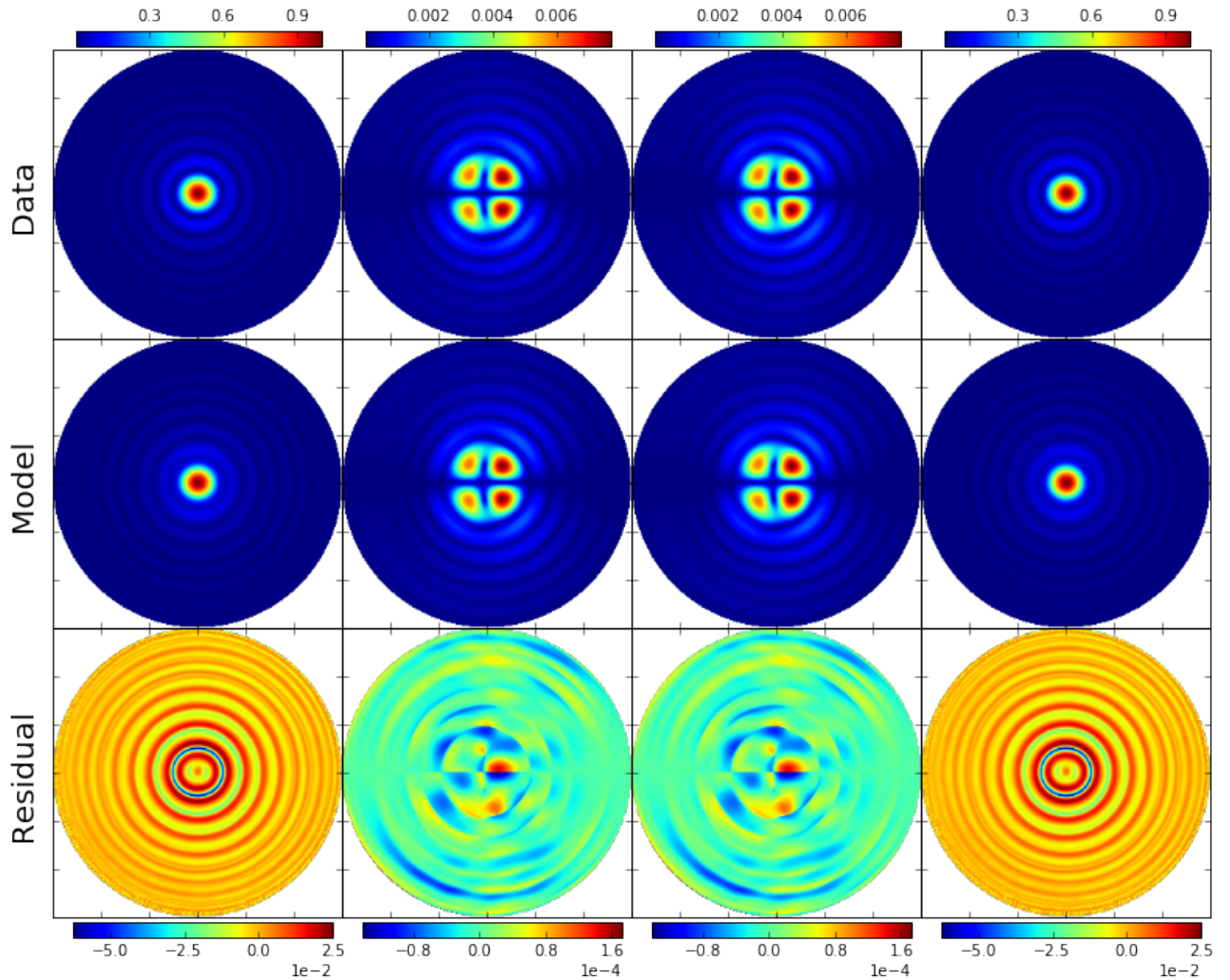


Figure 6.7: Zernike fit of band 5 EM beams at 4.6 GHz.

6.3.1.2 Spectral Representation

The spectra plots displayed in Figs. 6.8, 6.9 and 6.10 show that for lower wavelengths the ripple effect will be small compared to the higher ones since the ripple must be in the order of wavelength. These plots are produced from the strongest 6 Zernike coefficients for bands 1, 2 and 5.

We now present in the next section how the GRASP beams are corrupted.

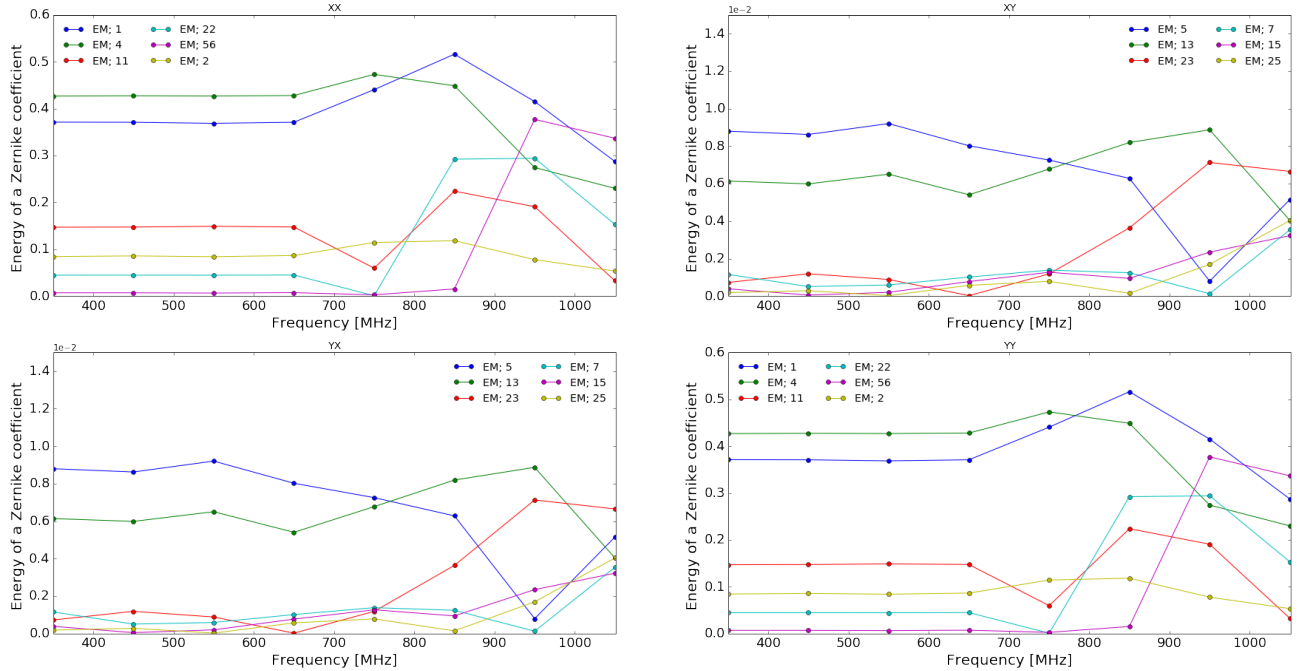


Figure 6.8: Spectral profile showing the various energy levels of Zernike coefficients for band 1 (350 – 1050 MHz).

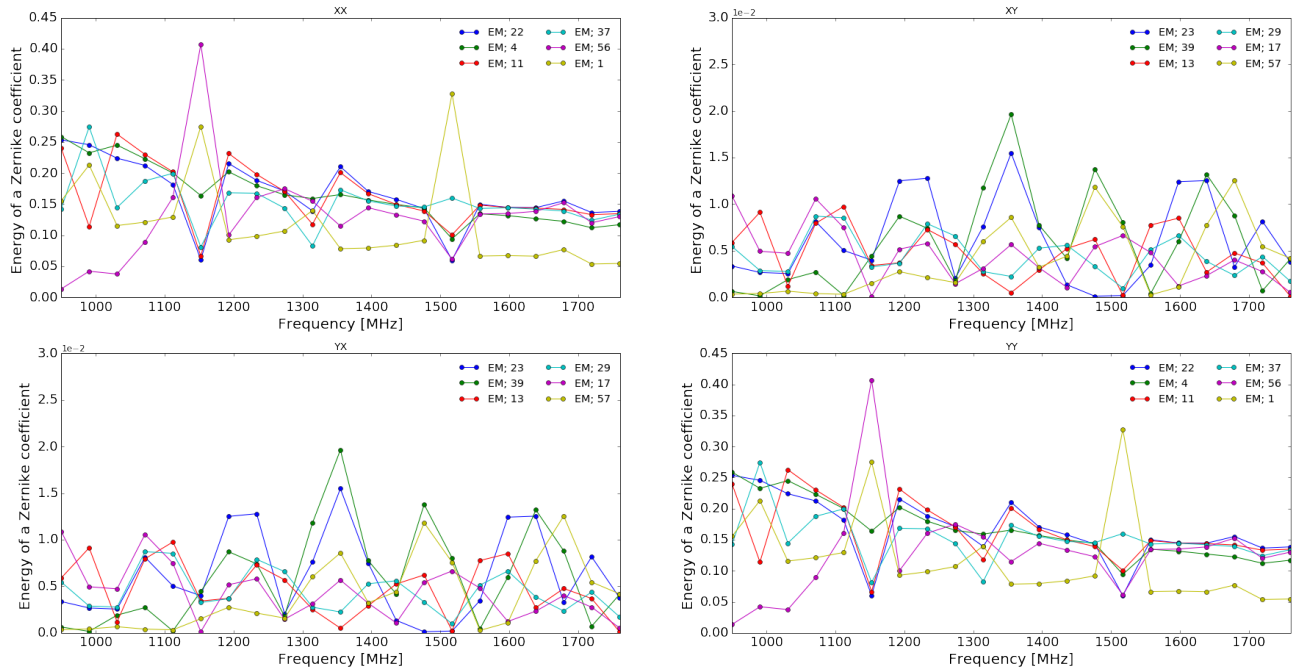


Figure 6.9: Spectral profile showing the various energy levels of Zernike coefficients for band 2 (950 – 1760 MHz).

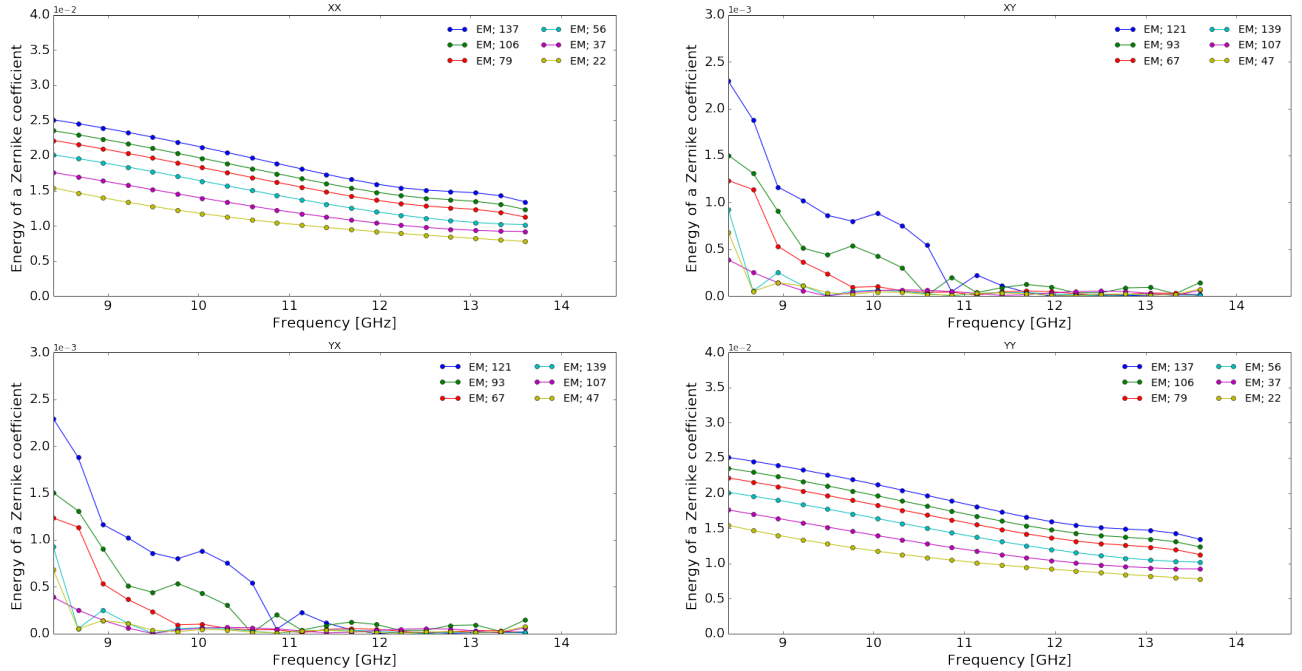


Figure 6.10: Spectral profile showing the various energy levels of Zernike coefficients for band 5 (8.4 – 13.6 GHz).

6.3.2 Model Beam Perturbation

Reflector imperfections can be considered by introducing thermal and mechanical distortions, gaps between reflector panels, supporting struts and scatterer material properties. In this work, we considered mechanical distortion whereby the phase of the antenna feed is displaced from the reference point along the horn by 2 mm. The effect of this distortion is represented in Figs. 6.11, 6.12 and 6.13 for bands 1, 2 and 5 respectively. Here, we note that there is $\approx 1\%$ distortion in both bands 1 and 2 EM beams and $\approx 10\%$ distortion in band 5 beams.

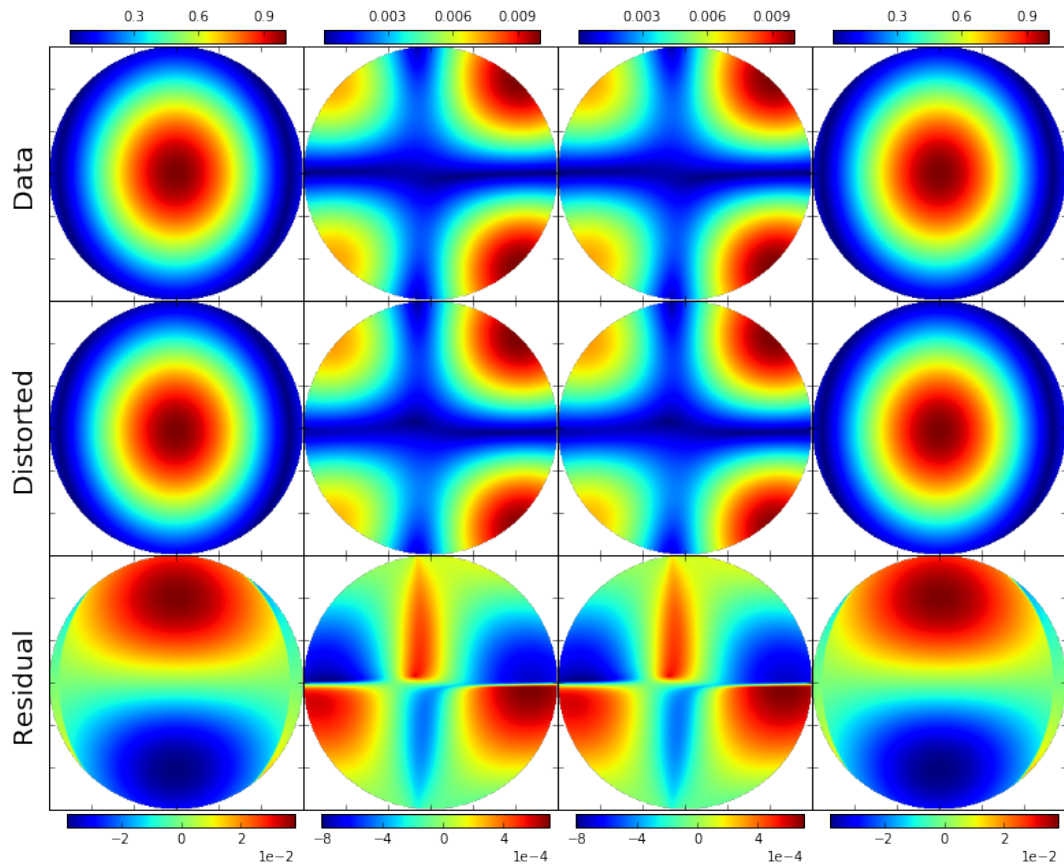


Figure 6.11: Perturbed beams for band 1 at 450 MHz.

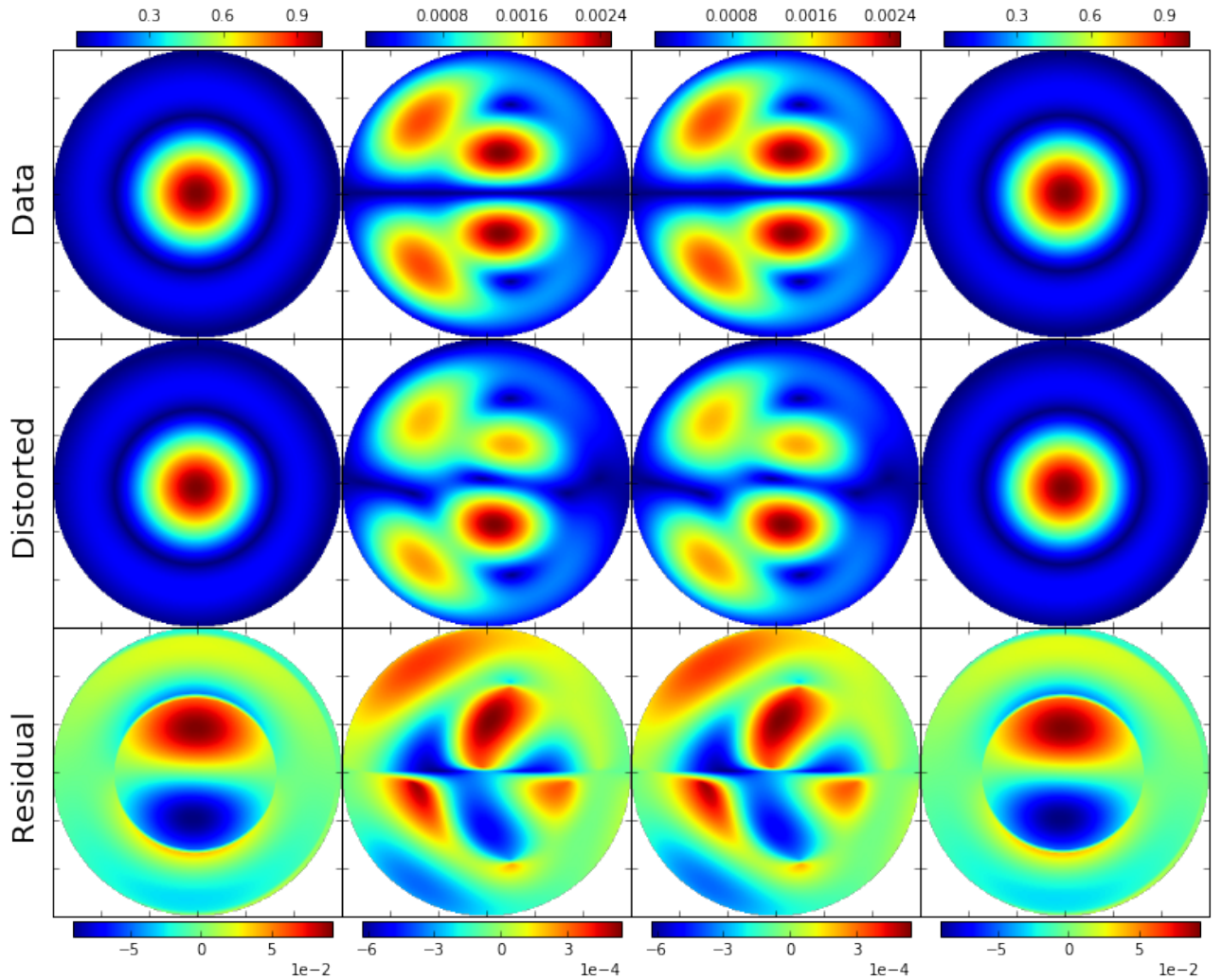


Figure 6.12: Perturbed beams for band 2 at 990.5 MHz.

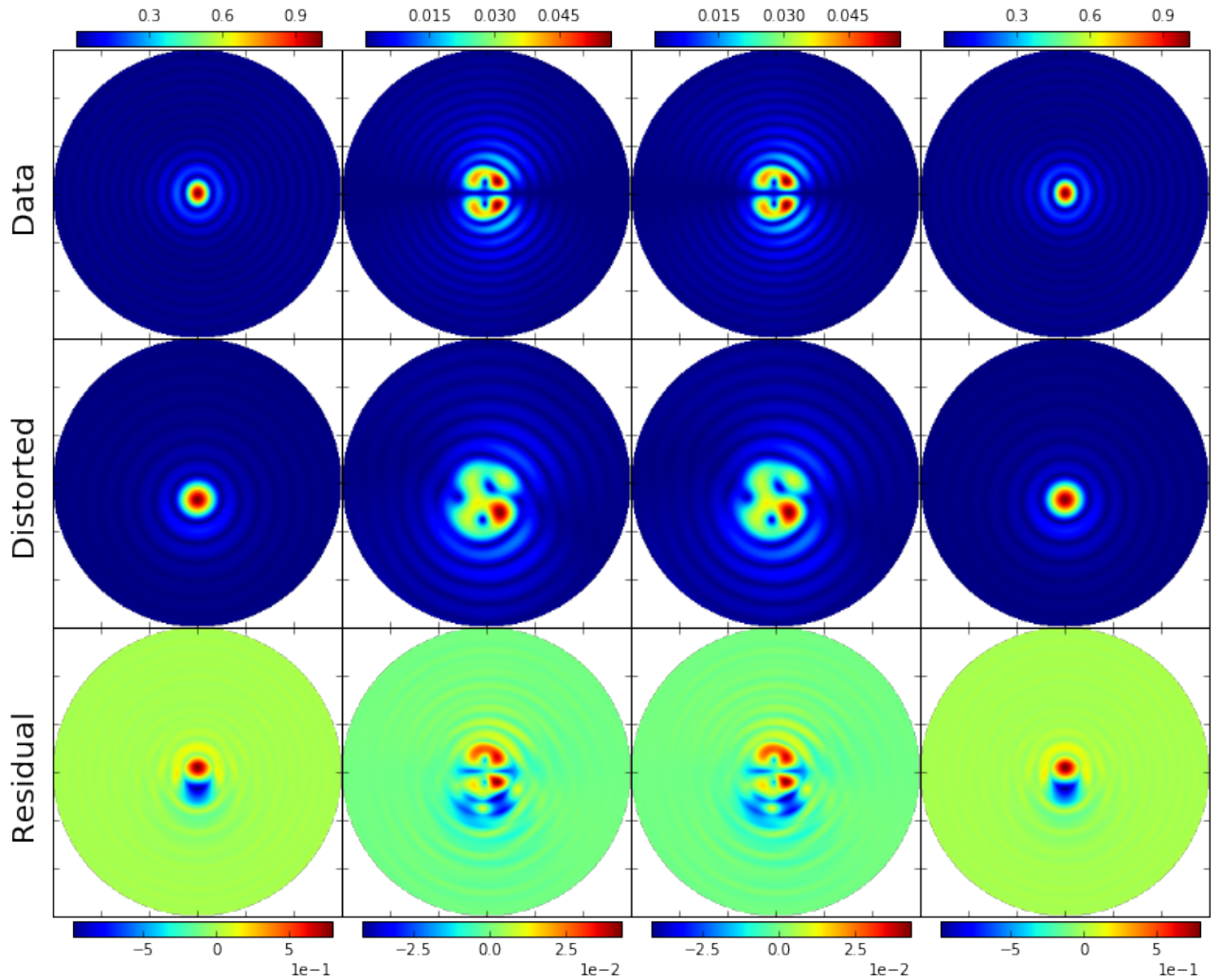


Figure 6.13: Perturbed beams for band 5 at 4.6 GHz.

6.3.3 Intrinsic Cross Polarisation (IXR)

A fundamental figure of merit (FoM) to understand the polarization performance of a polarimeter is the intrinsic cross-polarization ratio (IXR) introduced by Carozzi and Woan 2011. The term ‘intrinsic’ in IXR indicates that the parameter is independent of the choice of coordinate systems. IXR is related to the invertibility of a DD Jones matrix. The Jones matrices calculated by calibration are inverted and multiplied with the data to give the ‘corrected’ data, and hence the intrinsic invertibility of a Jones matrix put a fundamental limit to the extent to which a data can be corrected. For Stokes polarimeters, IXR can be easily converted to a Mueller IXR, which, in turn, is directly related to the fractional polarization leakage (fraction of Stokes I signal leaked into Stokes Q, U, V and vice versa) caused by the beam, mathematically:

$$IXR = 10 \log_{10} \left(\frac{\sqrt{M_{IQ}^2 + M_{IU}^2 + M_{IV}^2}}{|M_{II}|} \right) \quad (6.3)$$

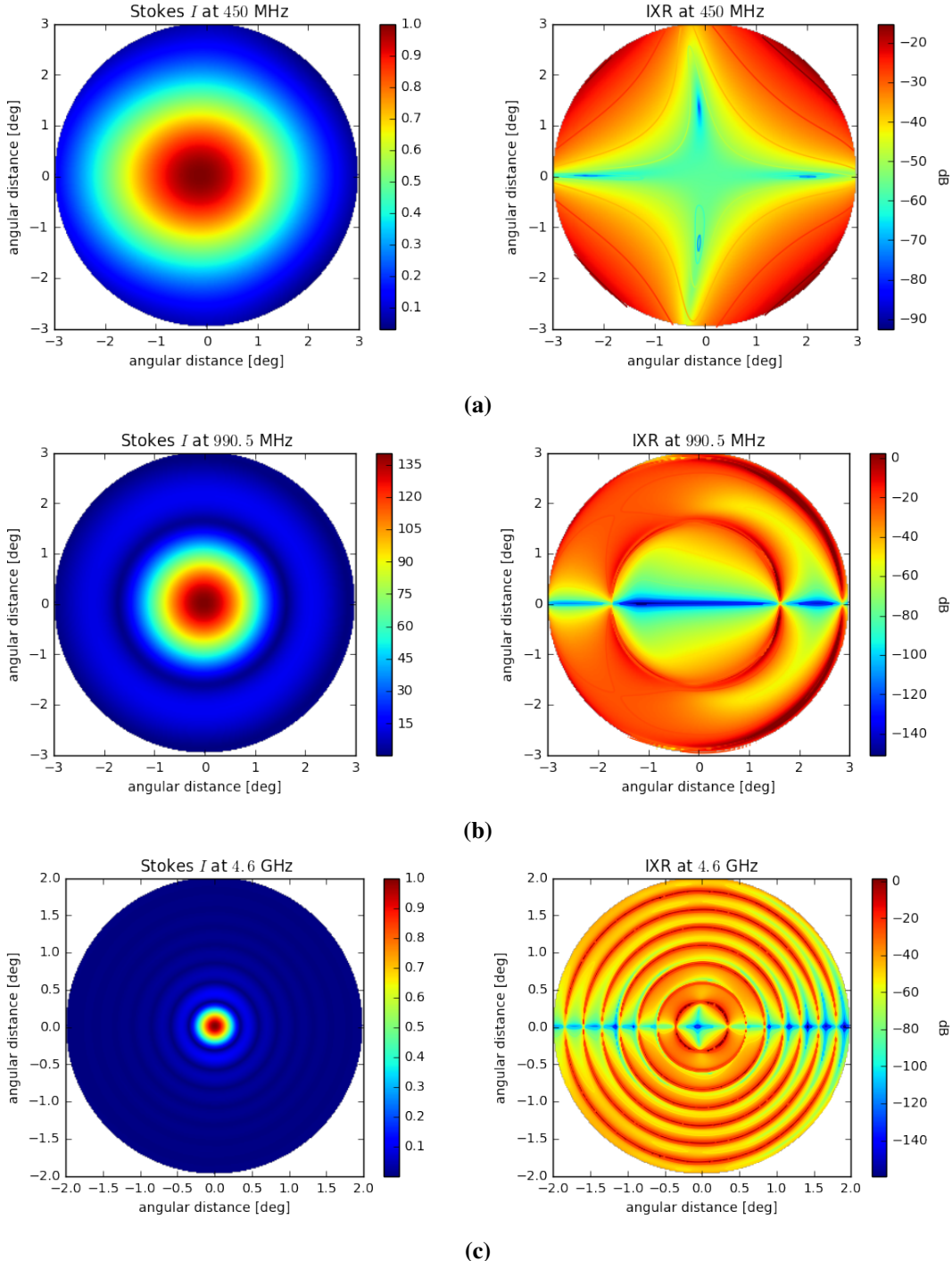


Figure 6.14: Representation of IXR and the corresponding Stokes I beams.

Figs. 6.14a, 6.14b, 6.14c show the plots for bands 1, 2 and 5 respectively.

Fig. 6.14 shows the IXRs (the right plots) and the corresponding Stokes I beams (the left

plots) for the various bands. The expected IXR for SKA1-mid is computed at -20 dB within HPBW. In addition, the rings in the IXR plots correspond to the beam nulls, where everything is allowed to cancel out almost entirely and also, note how the ring spacing scales with frequency.

6.4 MODELLING CO EMISSION

In this section we will outline our method for modelling the power spectrum of CO fluctuations. In order to understand the derivation of CO temperature refer to Breyssse, Kovetz, and Kamionkowski 2014. Here, we concentrate on the methods to adopt to estimate the angular spectrum distribution of CO emission.

6.4.1 The CO Power Spectrum

With the view to estimate the angular power spectrum of CO emission (C_l), we have to deduce the underlying 3D mass distribution to C_l . The brief description below shows the approach of Huterer, Knox, and Nichol 2001; Tegmark et al. 2002; Blake, Ferreira, and Borrill 2004; Padmanabhan et al. 2007; Thomas, Abdalla, and Lahav 2011. The angular power spectrum C_l is a projection of the spatial power spectrum of mass fluctuations at different red-shifts, $P(k, z)$, where k is a co-moving wavenumber. In linear perturbation theory, fluctuations with different k evolve independently, scaling with redshift according to the growth factor $D(z)$. Under this assumption we can simply scale the present-day matter power spectrum $P_0(k)$ back with redshift:

$$P(k, z) = P_0(k)D(z)^2 \quad (6.4)$$

where $D(z)^2 = (1 + z)^{-1}$. Assume linear theory holds, then the angular power spectrum C_l can be written in terms of the present-day matter power spectrum $P_0(k)$ as

$$C_l = \int P_0(k)W_l(k)dk \quad (6.5)$$

The kernel function $W_l(k)$ in equation (6.5) is defined as;

$$W_l(k) = \frac{2}{\pi} \left[\int_0^\infty j_l(u)f(u/k)du \right]^2 \quad (6.6)$$

The resulting spherical Bessel function $j_l(u)$ and the projection's weight $f(u/k)$ in equation (6.6) have been taken in by the kernel function. If we let $x = u/k$, then the function $f_z(x)$ which depends on the radial distribution of the sources becomes;

$$f_z(x) = p(z)D(z)b(z)\frac{dz}{dx} \quad (6.7)$$

In equation (6.7), x is the co-moving radial coordinate at redshift z , $p(z)$ is the redshift probability distribution of the sources such that, the normalised form is defined as $\int p(z)dz = 1$ and the linear bias factor $b(z)$ correlates the clustering of galaxies to clustering of the underlying mass such that $P_{gal}(k, z) = b(z)^2 P_{mass}(k, z)$.

At large l , we can approximate the spherical Bessel function in equation (6.6) such that $j_l(x) \approx (\pi/2l)^{1/2} \delta(x - l)$ to get;

$$W_l(k) \approx \frac{1}{l} f(l/k)^2 \quad (6.8)$$

Therefore, as l becomes large, the kernel function just translates along the k -axis. Combining equations (6.5) and (6.8) produce the approximation

$$C_l \approx \frac{1}{l} \int P_0(k) f(l/k)^2 dk \quad (6.9)$$

Translating equation (6.9) into an integral over radial co-ordinate we have;

$$C_l \approx \int P_0(l/x) x^{-2} f(x)^2 dx \quad (6.10)$$

Assume the spatial power spectrum is a power-law such that $P_0(k) \propto k^n$, then equation (6.10) predicts that $C_l \propto l^n$, regardless of the form of the radial distribution $p(z)$. For $n = 1$ gives $C_l \propto \frac{1}{l(l+1)}$ at low l . This is due to the fluctuations in gravitational potential and the probing fluctuations in mass.

In this research we use the CAMB¹ software package to compute the angular power spectrum (C_l) of the CO signal at $z = 5$. This package is able to set cosmological parameters in terms of physical densities and parameters used in Ade et al. 2016.

6.5 Results and Analysis

Repeating the full-sky simulation discussed in chapter 4, we perform IM experiments by convolving the foregrounds in Figs. 3.5, 3.6 and 3.7 with the GRASP, Zernike and distorted modelled beams for each band. Figs. 6.15 and 6.16 show the systematic error maps for band 1 when we compute the differences between the convolved foregrounds using fully polarised GRASP beams and distorted beams and the differences between the measured foregrounds using fully polarised GRASP beams and Zernike beams respectively. Similar explanations can be given to the error maps in Figs. 6.17, 6.18 and Figs. 6.19, 6.20 for using bands 2 and 5 fully polarised primary beams accordingly.

¹<http://camb.readthedocs.io/en/latest/>

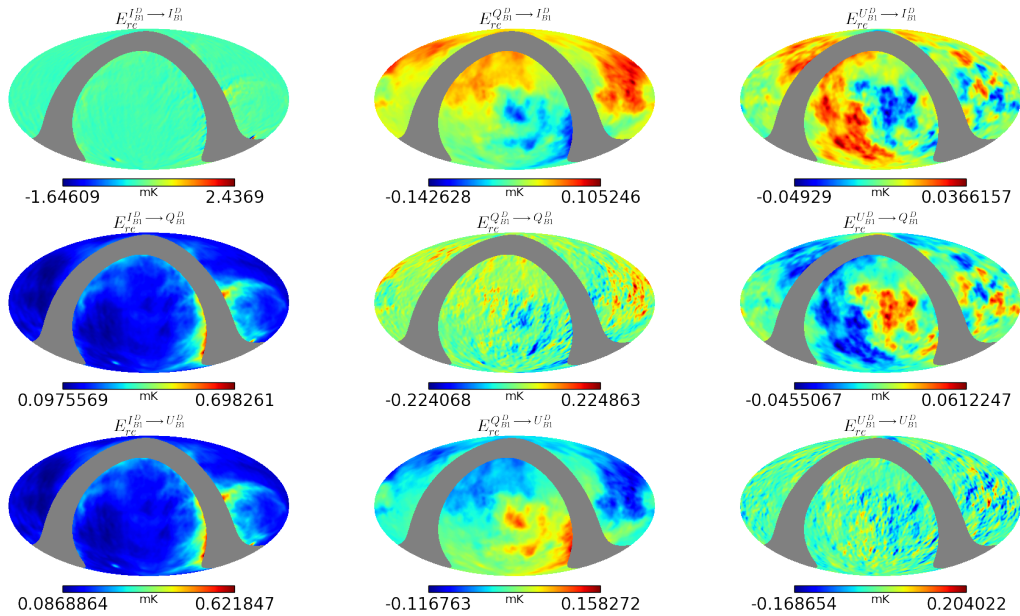


Figure 6.15: Systematic errors of measured maps due to feed displacement at 450 MHz.

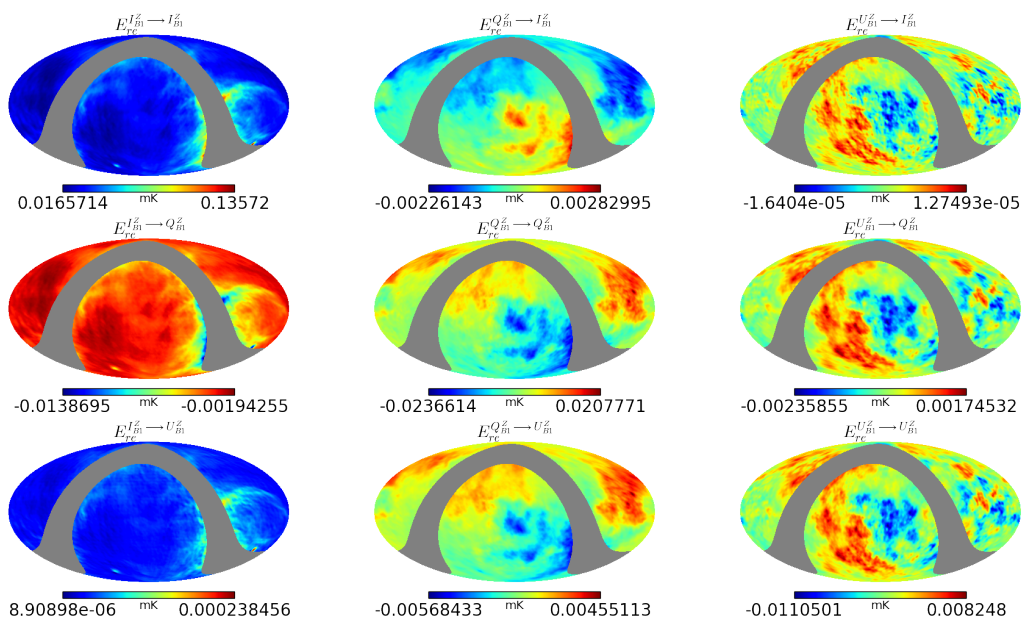


Figure 6.16: Systematic errors of measured maps using Zernike model beams at 450 MHz.

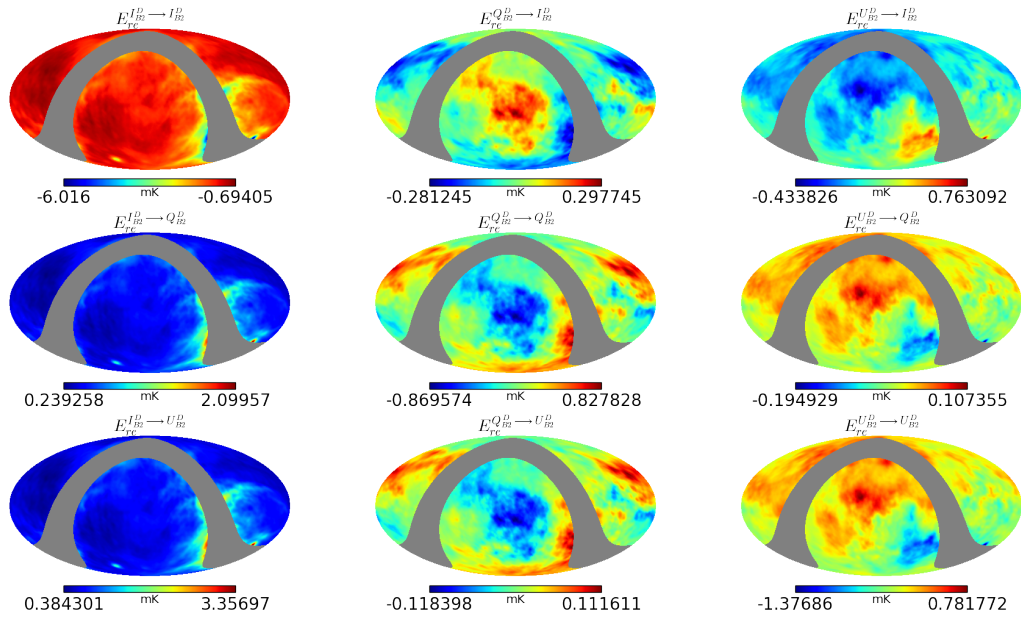


Figure 6.17: Systematic errors of measured maps due to feed displacement at 990.5 MHz.

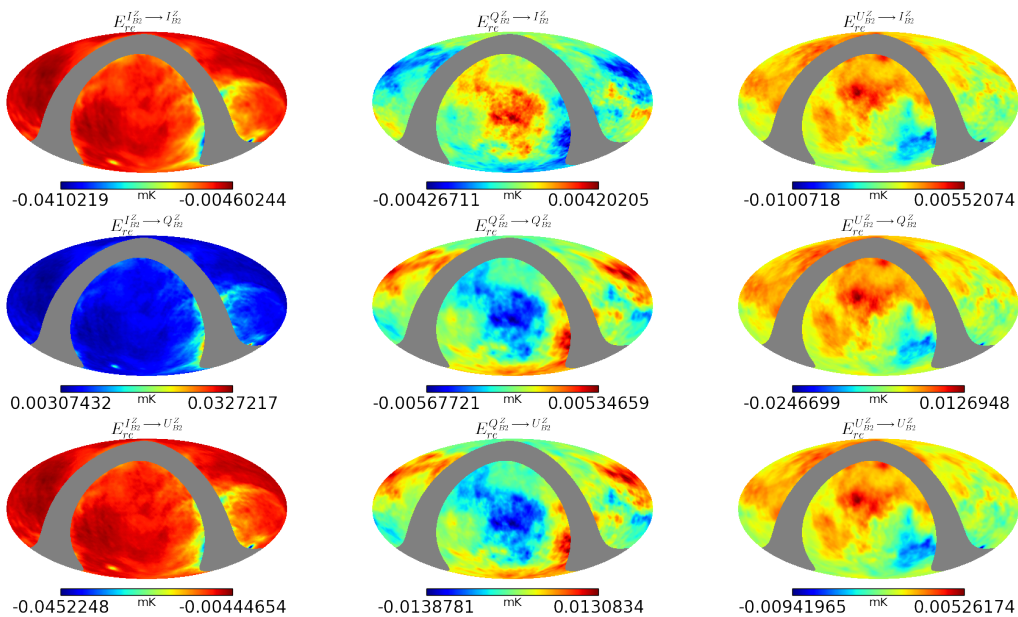


Figure 6.18: Systematic errors of measured maps using Zernike model beams at 990.5 MHz.

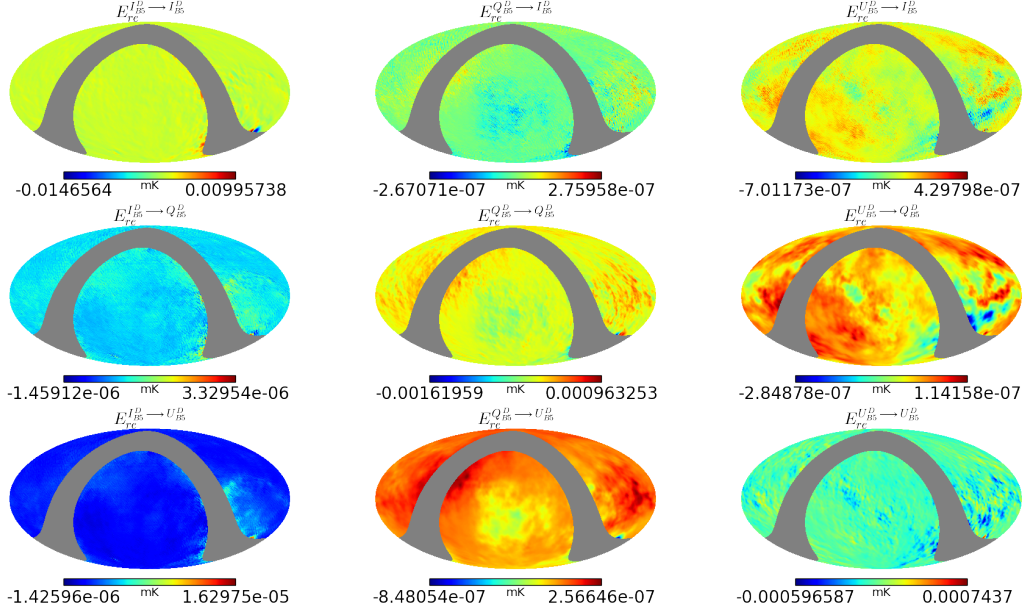


Figure 6.19: Systematic errors of measured maps due to feed displacement at 4.6 GHz.

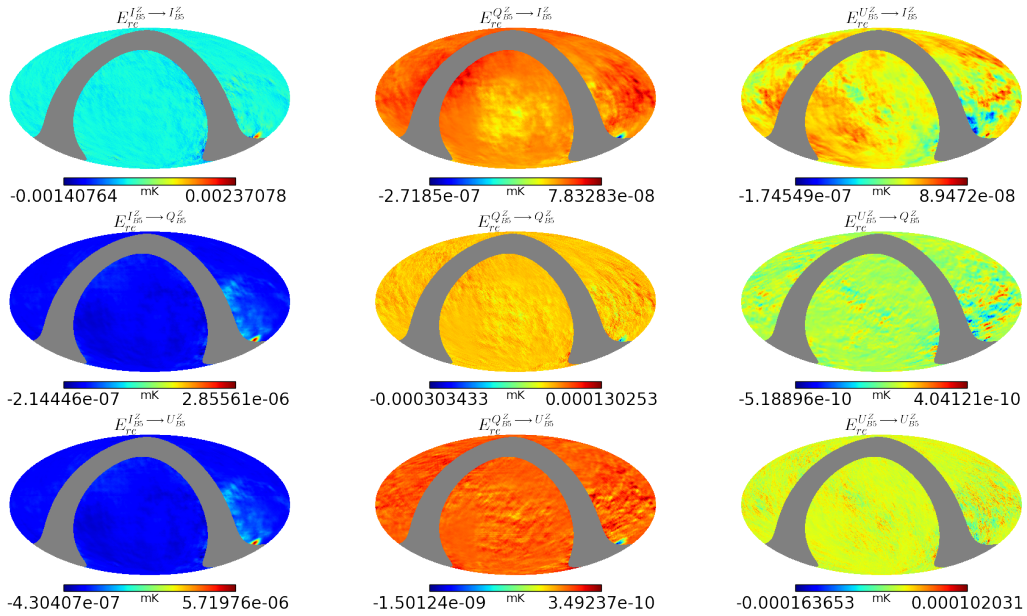


Figure 6.20: Systematic errors of measured maps using Zernike model beams at 4.6 GHz.

Fig. 6.21 shows the measured Stokes and the corresponding errors in Stokes I , Q and U when we convolve the full-sky polarisation maps with band 5 primary beams. The maps in the first row are produced when we use the GRASP beams to convolve the foregrounds. The second row is obtained for using perturbed beams produced from the GRASP package and the third row is as a result of using the Zernike beam models. The last two rows are the respective errors in Stokes I , Q and U for using distorted and reconstructed beam models. Generating

similar plots for the lower bands, we can transform these spatial distributions into spherical harmonics to determine the angular power spectrum.

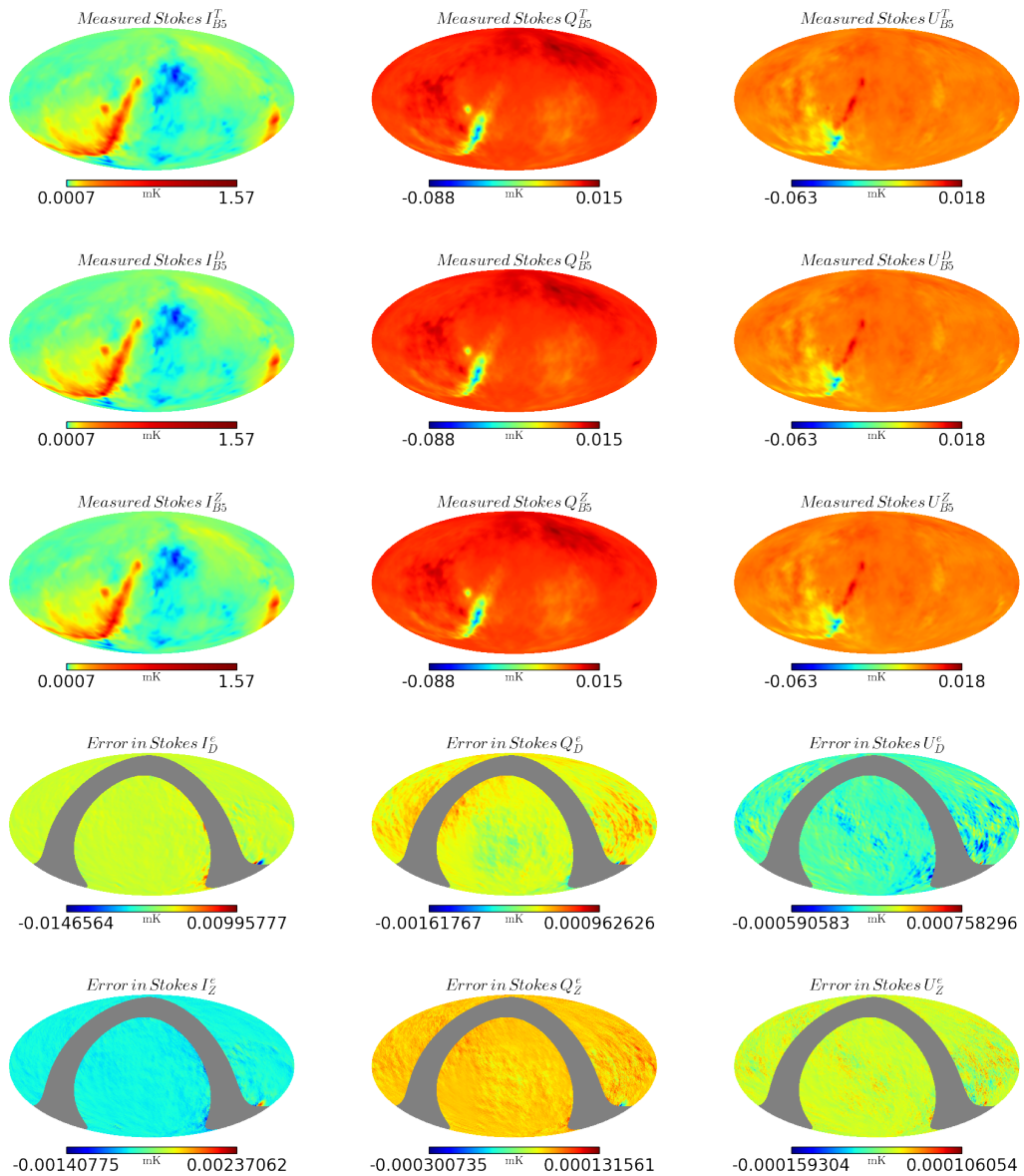


Figure 6.21: Convolved full-sky maps at 4.6 GHz with respective error in Stokes I , Q and U .

These power spectra as reported in Fig. 6.22 enable us to estimate both HI and CO signals at a specific moment. Since in IM we are mostly interested in the total intensity and the leakages from linear polarisation to total intensity, we measure the HI and CO signals in Stokes I . The left spectra plots in Figs. 6.22a, 6.22b, 6.22c show how we measure the signals when the errors in the primary beams of a particular band are corrected. For band 1, when the beam errors are corrected in Stokes I , we expect the HI signal at $z \approx 0.67$ to be measured at a multipole moment of $l \lesssim 50$ which is about 3 orders of magnitude greater at lower scales. At band 2, the HI signal is also measured at a multipole moment of $l \lesssim 50$ and about 4 orders of magnitude greater at lower scales. For the band 5, the CO signal at $z \approx 5$ is expected to be

measured at a multipole moment of $l \ll 50$ which is about 3 orders of magnitude lower at lower scales. The right spectra plots in Figs. 6.22a, 6.22b, 6.22c show how we measure the signals when the intrinsic linear polarisation leakage in Stokes I is known whilst the errors in the primary beams of a particular band are not corrected. The power spectrum of the HI signal for bands 1 and 2 can be estimated at a multipole moment of ≈ 50 and ≈ 100 respectively. For band 5, the estimated power spectrum of the CO signal is at a multipole moment of ≈ 50 . In addition, the spectra plots due to Zernike model of the beam for all bands clearly predicted both the HI and CO signals to be measured at a multipole moment of $l \lesssim 50$, making Zernike fitting a good reconstructed model for intensity mapping experiments.

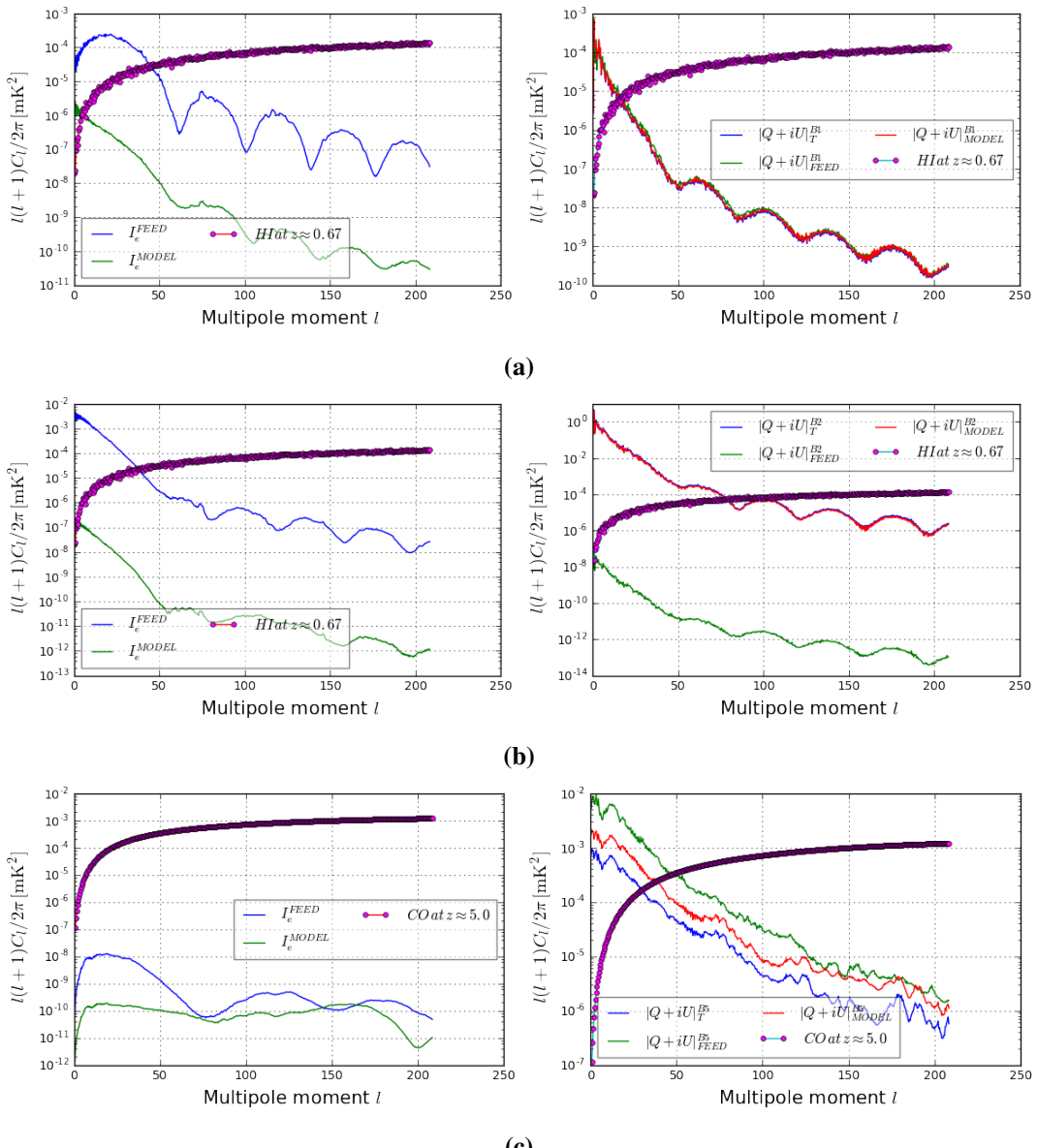


Figure 6.22: Comparing the distribution of angular power plots between corrected beam errors due to Zernike fits or feed displacement in Stokes I map (left plots) and intrinsic polarisation leakage in I (right plots) and how these affect both the 21 cm and CO signal (solid circular spectrum plot). (a) For band 1 at 450 MHz (b) For band 2 at 990.5 MHz (c) For band 5 at 4.6 GHz

6.6 Conclusion

This work showed how to simulate EM primary beams of SKA1-mid for bands 1, 2 and 5 using GRASP, a commercial software package. A Zernike fit was then used to reproduce these EM beams and then went on further to produce errors in the EM beams by displacing the coordinates of the GRASP feed model from its reference position. HI intensity mapping experiment was performed with the primary beams of bands 1 and 2 and then CO intensity mapping with band 5 in order to estimate the power spectrum of both HI and CO signals. The following are the key findings of the research:

- The co- and cross-polarization level of amplitude (ρ) for Band 1 (refer to Fig. 6.2) at different spherical cuts are within the range of $(-20 \leq \rho \leq 40)$ dB and $(-40 \leq \rho \leq 10)$ dB respectively, that of Band 2 (refer to Fig. 6.3) are $(-10 \leq \rho \leq 40)$ dB and $(-40 \leq \rho \leq 10)$ dB respectively and then for Band 5 (refer to Fig. 6.4) we have $(0 \leq \rho \leq 60)$ dB and $(-20 \leq \rho \leq 30)$ dB respectively.
- It is easier to reconstruct Zernike model of EM beams for bands 1 and 2 than band 5 (refer to Figs. 6.5, 6.6 and 6.7). This is because as many as 1000 Zernike coefficients are needed to reconstruct the side lobes of band 5 primary beams. Hence, making CO IM more difficult to perform as compared to HI IM.
- The spectra profiles reported in Figs. 6.8, 6.9 and 6.10 show that at lower wavelengths the ripple effect is much smaller compared to the higher ones. This is because we expect the ripple effect to be in the order of wavelength.
- The IXR of SKA1-mid is shown in Fig. 6.14 is calculated at -20 dB within HPBW.
- The angular power spectra plots in Figs. 6.22a, 6.22b, 6.22c show that when we correct for the errors in the beam in Stokes I , the power of the 21 cm signals can be determined at a multipole moment of $l \lesssim 50$ for bands 1 and 2 and that of the CO signal can be estimated at a multipole moment of $l \ll 50$ for band 5. But if the errors in the beam are not corrected for, then we expect both signals to be estimated at a multipole moments between $50 \leq l \leq 100$.

In summary, Zernike model is very good for HI and CO IM experiments, even though it is relatively difficult to construct primary beams for CO IM. In addition, although the SKA1-mid is not exclusively built for IM experiments, these simulations have clearly shown that it can be used to investigate HI and CO IM experiments.

Chapter 7

Conclusions

The key focus of this project is to develop IM techniques for mapping out primary beams of a radio telescope and then, introduce realistic errors to perturb these modelled beams. We then attempt a correction and calibration of these distorted modelled beams and ultimately, use the final data for intensity mapping experiments. Thus, we use these modelled beams to simulate the full-sky polarisation maps and then, determine the amount of foregrounds that have corrupted the total intensity due to polarisation leakage and errors in the primary beams which have not been accounted for. Therefore, the two critical things the study addresses are:

- (i) the contribution of polarisation leakage to the measured HI and CO power spectrum, given some more or less realistic primary beams and
- (ii) the uncertainty on the estimate of (i) introduced by unmodelled perturbations in the primary beam.

The following are some of the main findings of the research:

- The IXR computed for the SKA1-mid shows that, the angular separation for which the magnitude of the beam pattern decreases is approximately -20 dB from the peak of the main beam.
- Zernike fitting is a good model to reconstruct primary beams especially at bands 1 and 2 hence, a very useful tool for IM experiments .
- If a true model of the beam is assumed, then the fractional leakage of the intrinsic $|Q + iU|_T \rightarrow I$ is $\approx 1.0\%$, hence, making it possible to measure the power spectrum of both CO and 21 cm at a multipole moment of $l \lesssim 50$ which agrees with when we correct for the beam errors in Stokes I .
- Convolution is a very good technique for IM experiments since we can use this approach to measure total intensity of a signal.

In summary, with a good model of the primary beams we can actually estimate the amount of foregrounds that leak from intensity to polarisation.

Bibliography

- Abitbol, M. H., J. C. Hill, and B. R. Johnson (2016). “Foreground-induced biases in CMB polarimeter self-calibration”. In: *MNRAS* 457, pp. 1796–1803. doi: [10.1093/mnras/stw030](https://doi.org/10.1093/mnras/stw030). arXiv: [1512.06834](https://arxiv.org/abs/1512.06834).
- Abrantes, F. et al. (2009). “Proxy calibration to instrumental data set: Implications for pale-oceanographic reconstructions”. In: *Geochemistry, Geophysics, Geosystems* 10, Q09U07, Q09U07. doi: [10.1029/2009GC002604](https://doi.org/10.1029/2009GC002604). arXiv: [0806.2228](https://arxiv.org/abs/0806.2228).
- Acosta-Pulido, J. A. et al. (2015). “The Spanish Square Kilometre Array White Book”. In: *ArXiv e-prints*. arXiv: [1506.03474 \[astro-ph.IM\]](https://arxiv.org/abs/1506.03474).
- Ade, P. A. R. et al. (2016). “Planck 2015 results. XIII. Cosmological parameters”. In: *Astron. Astrophys.* 594, A13. doi: [10.1051/0004-6361/201525830](https://doi.org/10.1051/0004-6361/201525830). arXiv: [1502.01589 \[astro-ph.CO\]](https://arxiv.org/abs/1502.01589).
- Adriani, O. et al. (2011). “Cosmic-Ray Electron Flux Measured by the PAMELA Experiment between 1 and 625 GeV”. In: *Physical Review Letters* 106.20, 201101, p. 201101. doi: [10.1103/PhysRevLett.106.201101](https://doi.org/10.1103/PhysRevLett.106.201101). arXiv: [1103.2880 \[astro-ph.HE\]](https://arxiv.org/abs/1103.2880).
- Alonso, D., P. G. Ferreira, and M. G. Santos (2014). “Fast simulations for intensity mapping experiments”. In: *MNRAS* 444, pp. 3183–3197. doi: [10.1093/mnras/stu1666](https://doi.org/10.1093/mnras/stu1666). arXiv: [1405.1751](https://arxiv.org/abs/1405.1751).
- Alonso, D. et al. (2015). “Blind foreground subtraction for intensity mapping experiments”. In: *mnras* 447, pp. 400–416. doi: [10.1093/mnras/stu2474](https://doi.org/10.1093/mnras/stu2474). arXiv: [1409.8667](https://arxiv.org/abs/1409.8667).
- Anderson, L. B. et al. (2012). “Heterotic line bundle standard models”. In: *Journal of High Energy Physics* 6, 113, p. 113. doi: [10.1007/JHEP06\(2012\)113](https://doi.org/10.1007/JHEP06(2012)113). arXiv: [1202.1757 \[hep-th\]](https://arxiv.org/abs/1202.1757).
- Armstrong, R. P., K. Zarb Adami, and M. E. Jones (2009). “A Wideband, Four-Element, All-Digital Beamforming System for Dense Aperture Arrays in Radio Astronomy”. In: *ArXiv e-prints*. arXiv: [0910.2865 \[astro-ph.IM\]](https://arxiv.org/abs/0910.2865).
- Asad, K. M. B. et al. (2015). “Polarization leakage in epoch of reionization windows – I. Low Frequency Array observations of the 3C196 field”. In: *Monthly Notices of the Royal Astronomical Society* 451.4, pp. 3709–3727. doi: [10.1093/mnras/stv1107](https://doi.org/10.1093/mnras/stv1107). eprint: [/oup/backfile/content_public/journal/mnras/451/4/10.1093/mnras/stv1107/2/stv1107.pdf](https://oup/backfile/content_public/journal/mnras/451/4/10.1093/mnras/stv1107/2/stv1107.pdf). URL: [+http://dx.doi.org/10.1093/mnras/stv1107](http://dx.doi.org/10.1093/mnras/stv1107).
- Balanis, C. A. (2005). *Antenna Theory Analysis and Design*. Hoboken, New Jersey: John Wiley & Sons, Inc.

- Bandura, K. et al. (2014). “Canadian Hydrogen Intensity Mapping Experiment (CHIME) pathfinder”. In: *Ground-based and Airborne Telescopes V*. Vol. 9145. procspie, p. 914522. doi: [10.1117/12.2054950](https://doi.org/10.1117/12.2054950). arXiv: [1406.2288 \[astro-ph.IM\]](https://arxiv.org/abs/1406.2288).
- Bass, M. et al. (2009). *Handbook of Optics: Geometrical and Physical Optics, Polarized Light, Components and Instruments*. New York, US: McGraw Hill Professional.
- Battye, R. A. et al. (2012). “BINGO: a single dish approach to 21cm intensity mapping”. In: *ArXiv e-prints*. arXiv: [1209.1041 \[astro-ph.CO\]](https://arxiv.org/abs/1209.1041).
- Beardsley, A. P. et al. (2016). “An Efficient Feedback Calibration Algorithm for Direct Imaging Radio Telescopes”. In: *ArXiv e-prints*. arXiv: [1603.02126 \[astro-ph.IM\]](https://arxiv.org/abs/1603.02126).
- Bell, M. R. and T. A. Enßlin (2012). “Faraday synthesis. The synergy of aperture and rotation measure synthesis”. In: *A&A* 540, A80, A80. doi: [10.1051/0004-6361/201118672](https://doi.org/10.1051/0004-6361/201118672). arXiv: [1112.4175 \[astro-ph.IM\]](https://arxiv.org/abs/1112.4175).
- Ben-David, C. and A. Leshem (2008). “Parametric High Resolution Techniques for Radio Astronomical Imaging”. In: *IEEE Journal of Selected Topics in Signal Processing* 2, pp. 670–684. doi: [10.1109/JSTSP.2008.2005318](https://doi.org/10.1109/JSTSP.2008.2005318). arXiv: [0807.4852](https://arxiv.org/abs/0807.4852).
- Beutler, F. et al. (2011). “The 6dF Galaxy Survey: baryon acoustic oscillations and the local Hubble constant”. In: *MNRAS* 416, pp. 3017–3032. doi: [10.1111/j.1365-2966.2011.19250.x](https://doi.org/10.1111/j.1365-2966.2011.19250.x). arXiv: [1106.3366](https://arxiv.org/abs/1106.3366).
- Bhatnagar, S. et al. (2008). “Correcting direction-dependent gains in the deconvolution of radio interferometric images”. In: *A&A* 487, pp. 419–429. doi: [10.1051/0004-6361:20079284](https://doi.org/10.1051/0004-6361:20079284). arXiv: [0805.0834](https://arxiv.org/abs/0805.0834).
- Blake, C. et al. (2011). “The WiggleZ Dark Energy Survey: mapping the distance-redshift relation with baryon acoustic oscillations”. In: *MNRAS* 418, pp. 1707–1724. doi: [10.1111/j.1365-2966.2011.19592.x](https://doi.org/10.1111/j.1365-2966.2011.19592.x). arXiv: [1108.2635](https://arxiv.org/abs/1108.2635).
- Blake, Chris, Pedro G. Ferreira, and Julian Borrill (2004). “The Angular power spectrum of NVSS radio galaxies”. In: *Mon. Not. Roy. Astron. Soc.* 351, p. 923. doi: [10.1111/j.1365-2966.2004.07831.x](https://doi.org/10.1111/j.1365-2966.2004.07831.x). arXiv: [astro-ph/0404085 \[astro-ph\]](https://arxiv.org/abs/astro-ph/0404085).
- Bolonkin, Alexander (2017). *Femtotechnologies and Innovative Projects*. Lulu. com.
- Born, M. and E. Wolf (1965). *Principles of Optics*. New York: Pergamon Press.
- Born, M. and E. Wolf (1980). *Principles of Optics Electromagnetic Theory of Propagation, Interference and Diffraction of Light*.
- Brentjens, M. A. and A. G. de Bruyn (2005). “Faraday rotation measure synthesis”. In: *A&A* 441, pp. 1217–1228. doi: [10.1051/0004-6361:20052990](https://doi.org/10.1051/0004-6361:20052990). eprint: [astro-ph/0507349](https://arxiv.org/abs/astro-ph/0507349).
- Breysse, Patrick C., Ely D. Kovetz, and Marc Kamionkowski (2014). “Carbon Monoxide Intensity Mapping at Moderate Redshifts”. In: *Mon. Not. Roy. Astron. Soc.* 443.4, pp. 3506–3512. doi: [10.1093/mnras/stu1312](https://doi.org/10.1093/mnras/stu1312). arXiv: [1405.0489 \[astro-ph.CO\]](https://arxiv.org/abs/1405.0489).
- Brisken, W. (2003). *A program for Cassegrain antenna modelling*. A Cassegrain antenna simulator. <http://packages.ubuntu.com/lucid/cassbeam>.
- Burke, Bernard F and Francis Graham-Smith (2009). *An introduction to radio astronomy*. Cambridge University Press.
- Burn, B. J. (1966). “On the depolarization of discrete radio sources by Faraday dispersion”. In: *MNRAS* 133, p. 67. doi: [10.1093/mnras/133.1.67](https://doi.org/10.1093/mnras/133.1.67).

- Camera, Stefano et al. (2014). “Cosmology on the largest scales with intensity mapping”. In: *Journal of Physics: Conference Series*. Vol. 566. 1. IOP Publishing, p. 012004.
- Campbell, Charles E (2003). “A new method for describing the aberrations of the eye using Zernike polynomials”. In: *Optometry & Vision Science* 80.1, pp. 79–83.
- Camps, A. et al. (1998). “Extension of the Clean Technique to the Microwave Imaging of Continuous Thermal Sources by Means of Aperture Synthesis Radiometers”. In: *Progress In Electromagnetics Research Symposium* 18.
- Carozzi, TD and G Woan (2011). “A fundamental figure of merit for radio polarimeters”. In: *IEEE Transactions on Antennas and Propagation* 59.6, pp. 2058–2065.
- Chai, Xiaoming et al. (2016). “Experiments on the dish verification antenna china for the SKA”. In: *Experimental Astronomy* 42.3, pp. 301–317.
- Chang, T.-C. et al. (2008). “Baryon Acoustic Oscillation Intensity Mapping of Dark Energy”. In: *Phys. Rev. Lett.* 100.091303.
- Charman, WN (2005). “Wavefront technology: past, present and future”. In: *Contact Lens and Anterior Eye* 28.2, pp. 75–92.
- Chen, X. (2012). “The Tianlai Project: a 21CM Cosmology Experiment”. In: *International Journal of Modern Physics Conference Series*. Vol. 12. International Journal of Modern Physics Conference Series, pp. 256–263. doi: [10.1142/S2010194512006459](https://doi.org/10.1142/S2010194512006459). arXiv: [1212.6278 \[astro-ph.IM\]](https://arxiv.org/abs/1212.6278).
- Ciardi, B. and P. Madau (2003). “Probing beyond the Epoch of Hydrogen Reionization with 21 Centimeter Radiation”. In: *Astrophysical Journal* 596, pp. 1–8. doi: [10.1086/377634](https://doi.org/10.1086/377634). eprint: [astro-ph/0303249](https://arxiv.org/abs/astro-ph/0303249).
- Clemente, C. et al. (2017). “Automatic Target Recognition of Military Vehicles With Krawtchouk Moments”. In: *IEEE Transactions on Aerospace Electronic Systems* 53, pp. 493–500. doi: [10.1109/TAES.2017.2649160](https://doi.org/10.1109/TAES.2017.2649160).
- Cole, S. et al. (2005). “The 2dF Galaxy Redshift Survey: power-spectrum analysis of the final data set and cosmological implications”. In: *MNRAS* 362, pp. 505–534. doi: [10.1111/j.1365-2966.2005.09318.x](https://doi.org/10.1111/j.1365-2966.2005.09318.x). eprint: [astro-ph/0501174](https://arxiv.org/abs/astro-ph/0501174).
- Colless, M. et al. (2003). “The 2dF Galaxy Redshift Survey: Final Data Release”. In: *ArXiv Astrophysics e-prints*. eprint: [astro-ph/0306581](https://arxiv.org/abs/astro-ph/0306581).
- Contreras, C. et al. (2013). “The WiggleZ Dark Energy Survey: measuring the cosmic growth rate with the two-point galaxy correlation function”. In: *MNRAS* 430, pp. 924–933. doi: [10.1093/mnras/sts608](https://doi.org/10.1093/mnras/sts608). arXiv: [1302.5178 \[astro-ph.CO\]](https://arxiv.org/abs/1302.5178).
- Coughlan, C. and D. Gabuzda (2012). “MEM and CLEAN Imaging of VLBA Polarisation Observations of Compact Active Galactic Nuclei”. In: *Journal of Physics Conference Series* 355.1, 012020, p. 012020. doi: [10.1088/1742-6596/355/1/012020](https://doi.org/10.1088/1742-6596/355/1/012020). arXiv: [1107.3481](https://arxiv.org/abs/1107.3481).
- Coughlan, C. P. and D. C. Gabzuda (2013). “MEM imaging of multi-wavelength VLBA polarisation observations of Active Galactic Nuclei”. In: *ArXiv e-prints*. arXiv: [1307.6757 \[astro-ph.GA\]](https://arxiv.org/abs/1307.6757).

- D'Angelo, G. and S. Rampone (2016). "Feature Extraction and Soft Computing Methods for Aerospace Structure Defect Classification". In: *ArXiv e-prints*. arXiv: [1611.04782 \[cs.CV\]](#).
- de Oliveira-Costa, A. et al. (2008). "A model of diffuse Galactic radio emission from 10 MHz to 100 GHz". In: *MNRAS* 388, pp. 247–260. doi: [10.1111/j.1365-2966.2008.13376.x](#). arXiv: [0802.1525](#).
- Decker, F. J. (1994). *Beam Distributions Beyond RMS*. 6th Workshop on Beam Instrumentation. Standford Linear Accelerator Center, University of Stanford.
- Desai, S. et al. (2016). "Detection and Removal of Artifacts in Astronomical Images". In: *ArXiv e-prints*. arXiv: [1601.07182 \[astro-ph.IM\]](#).
- Dewdney, Peter et al. (2015). "SKA1 system baseline V2 description". In: *SKA document SKA-TEL-SKO-0000308*.
- Duev, D. A. et al. (2015). "RadioAstron as a target and as an instrument: Enhancing the Space VLBI mission's scientific output". In: *A&A* 573, A99, A99. doi: [10.1051/0004-6361/201424940](#). arXiv: [1411.4576 \[astro-ph.IM\]](#).
- Duffy, A. R. et al. (2012). "Modelling neutral hydrogen in galaxies using cosmological hydrodynamical simulations". In: *MNRAS* 420, pp. 2799–2818. doi: [10.1111/j.1365-2966.2011.19894.x](#). arXiv: [1107.3720 \[astro-ph.CO\]](#).
- Dulwich, F. et al. (2009). "OSKAR: Simulating Digital Beamforming for the SKA Aperture Array". In: *Wide Field Astronomy & Technology for the Square Kilometre Array*, p. 31.
- Emerson, D. (2002). "Why Single Dish". In: *ASP Conference Series*. 278.
- Ferreira, C. et al. (2015). "Orthogonal systems of Zernike type in polygons and polygonal facets". In: *ArXiv e-prints*. arXiv: [1506.07396 \[astro-ph.IM\]](#).
- Foster, G. (2015). *Required Instrumentation Information for Interferometrists and Radio Astronomers*. Research Report. RATT, Department of Physics and Electronics, Rhodes University.
- Fu, C. and J. Wu (2005). "Wavelet Interpolation Algorithm for Synthetic Aperture Radiometer". In: *Progress In Electromagnetics Research Symposium* 1.5, pp. 510–514.
- Furlanetto, Steven, S. Peng Oh, and Frank Briggs (2006). "Cosmology at Low Frequencies: The 21 cm Transition and the High-Redshift Universe". In: *Phys. Rept.* 433, pp. 181–301. doi: [10.1016/j.physrep.2006.08.002](#). arXiv: [astro-ph/0608032 \[astro-ph\]](#).
- Garrett, M. A. (2012). "Radio Astronomy Transformed: Aperture Arrays - Past, Present Future". In: *From Antikythera to the Square Kilometre Array: Lessons from the Ancients*, p. 41. arXiv: [1211.6455 \[astro-ph.IM\]](#).
- Gaylard, M. (2012). *Radio Astronomy with a Single-Dish Radio Telescope*. Tech. rep. Hartebeesthoek Radio Astronomy Observatory.
- Geil, P. M., B. M. Gaensler, and J. S. B. Wyithe (2011). "Polarized foreground removal at low radio frequencies using rotation measure synthesis: uncovering the signature of hydrogen reionization". In: *MNRAS* 418, pp. 516–535. doi: [10.1111/j.1365-2966.2011.19509.x](#). arXiv: [1011.2321](#).

- Ghosh, Abhik et al. (2011). “Improved foreground removal in GMRT 610 MHz observations towards redshifted 21-cm tomography”. In: *Mon. Not. Roy. Astron. Soc.* 418, p. 2584. doi: [10.1111/j.1365-2966.2011.19649.x](https://doi.org/10.1111/j.1365-2966.2011.19649.x). arXiv: [1108.3707 \[astro-ph.CO\]](https://arxiv.org/abs/1108.3707).
- Giardino, G. et al. (2002). “Towards a model of full-sky galactic synchrotron intensity and linear polarisation: a re-analysis of the parkes data”. In: *Astron. Astrophys.* 387, p. 82. doi: [10.1051/0004-6361:20020285](https://doi.org/10.1051/0004-6361:20020285). arXiv: [astro-ph/0202520 \[astro-ph\]](https://arxiv.org/abs/astro-ph/0202520).
- Goldstein, D. (2003). *Polarized Light: Revised and Expanded*. New York: Marcel Dekker, Inc.
- Gong, Y. et al. (2012). “Intensity Mapping of the [C II] Fine Structure Line during the Epoch of Reionization”. In: *ApJ* 745, 49, p. 49. doi: [10.1088/0004-637X/745/1/49](https://doi.org/10.1088/0004-637X/745/1/49). arXiv: [1107.3553](https://arxiv.org/abs/1107.3553).
- Górski, K. M. et al. (2005). “HEALPix: A Framework for High-Resolution Discretization and Fast Analysis of Data Distributed on the Sphere”. In: *ApJ* 622, pp. 759–771. doi: [10.1086/427976](https://doi.org/10.1086/427976). eprint: [astro-ph/0409513](https://arxiv.org/abs/astro-ph/0409513).
- Goswami, G. and J. Prasad (2013). “Maximum entropy deconvolution of primordial power spectrum”. In: 88.2, 023522, p. 023522. doi: [10.1103/PhysRevD.88.023522](https://doi.org/10.1103/PhysRevD.88.023522). arXiv: [1303.4747 \[astro-ph.CO\]](https://arxiv.org/abs/1303.4747).
- Gu, J. et al. (2013). “The Application of Continuous Wavelet Transform Based Foreground Subtraction Method in 21 cm Sky Surveys”. In: *ApJ* 773, 38, p. 38. doi: [10.1088/0004-637X/773/1/38](https://doi.org/10.1088/0004-637X/773/1/38). arXiv: [1306.5378](https://arxiv.org/abs/1306.5378).
- Hamaker, J. P., J. D. Bregman, and R. J. Sault (1996). “Understanding radio polarimetry. I. Mathematical foundations.” In: 117, pp. 137–147.
- Haslam, C.G.T. et al. (1982). “A 408 MHz all-sky continuum survey. II. The atlas of contour maps”. In: *A & AS* 47.
- Huterer, Dragan, Lloyd Knox, and Robert C. Nichol (2001). “The Angular power spectrum of EDSGC galaxies”. In: *Astrophys. J.* 555, p. 547. doi: [10.1086/323328](https://doi.org/10.1086/323328). arXiv: [astro-ph/0011069 \[astro-ph\]](https://arxiv.org/abs/astro-ph/0011069).
- Jelić, V. et al. (2008). “Foreground simulations for the LOFAR-epoch of reionization experiment”. In: *MNRAS* 389, pp. 1319–1335. doi: [10.1111/j.1365-2966.2008.13634.x](https://doi.org/10.1111/j.1365-2966.2008.13634.x). arXiv: [0804.1130](https://arxiv.org/abs/0804.1130).
- Jelić, V. et al. (2010). “Realistic simulations of the Galactic polarized foreground: consequences for 21-cm reionization detection experiments”. In: *mnras* 409, pp. 1647–1659. doi: [10.1111/j.1365-2966.2010.17407.x](https://doi.org/10.1111/j.1365-2966.2010.17407.x). arXiv: [1007.4135](https://arxiv.org/abs/1007.4135).
- Joardar, S. et al. (2010). “Radio Astronomy and Super-synthesis: A Survey”. In: *Progress In Electromagnetics Research B* 22.
- Jones, R. C. (1942). “A new calculus for the treatment of optical systems. IV”. In: *Journal of the Optical Society of America (1917-1983)* 32, p. 486.
- (1948). “New calculus for the treatment of optical systems. VII. Properties of the N-matrices”. In: *Journal of the Optical Society of America (1917-1983)* 38, p. 671.
- Junklewitz, H. et al. (2016). “RESOLVE: A new algorithm for aperture synthesis imaging of extended emission in radio astronomy”. In: *aap* 586, A76, A76. doi: [10.1051/0004-6361/201323094](https://doi.org/10.1051/0004-6361/201323094). arXiv: [1311.5282 \[astro-ph.IM\]](https://arxiv.org/abs/1311.5282).

- Kiyotomo, I. (2014). “CMB foreground: A concise review”. In: *Prog. Theor. Exp. Phys.* 06.B109. URL: <https://inspirehep.net/record/1301472/files/06B109.full.pdf>.
- Knee, Lewis BG and Christopher M Brunt (2001). “A massive cloud of cold atomic hydrogen in the outer Galaxy”. In: *Nature* 412.6844, pp. 308–310.
- Krachmalnicoff, N. et al. (2016). “Characterization of foreground emission on degree angular scales for CMB B-mode observations . Thermal dust and synchrotron signal from Planck and WMAP data”. In: *A&A* 588, A65, A65. doi: [10.1051/0004-6361/201527678](https://doi.org/10.1051/0004-6361/201527678). arXiv: [1511.00532](https://arxiv.org/abs/1511.00532).
- Kraus, J. D. (1966). *Radio Astronomy*. New York: McGraw-Hill, Inc.
- Lakshminarayanan, Vasudevan and Andre Fleck (2011). “Zernike polynomials: a guide”. In: *Journal of Modern Optics* 58.7, pp. 545–561.
- Landeck, Carl F et al. (2017). *Apparatus for manufacturing a hydrogen 21 line precision measuring device*. US Patent 9,687,939.
- Leshem, A. and A.-J. van der Veen (2000). “Radio astronomical imaging in the presence of strong radio interference”. In: *ArXiv Astrophysics e-prints*. eprint: [astro-ph/0008239](https://arxiv.org/abs/astro-ph/0008239).
- Levanda, R. and A. Leshem (2010a). “Adaptive selective sidelobe canceller beamformer with applications in radio astronomy”. In: *ArXiv e-prints*. arXiv: [1008.5066 \[astro-ph.IM\]](https://arxiv.org/abs/1008.5066). – (2010b). “Synthetic aperture radio telescopes”. In: *IEEE Signal Processing Magazine* 27, pp. 14–29. doi: [10.1109/MSP.2009.934719](https://doi.org/10.1109/MSP.2009.934719). arXiv: [1009.0460 \[astro-ph.IM\]](https://arxiv.org/abs/1009.0460).
- Lidz, Adam et al. (2011). “Intensity Mapping with Carbon Monoxide Emission Lines and the Redshifted 21 cm Line”. In: *Astrophys. J.* 741, p. 70. doi: [10.1088/0004-637X/741/2/70](https://doi.org/10.1088/0004-637X/741/2/70). arXiv: [1104.4800 \[astro-ph.CO\]](https://arxiv.org/abs/1104.4800).
- Loeb, A. and J. S. B. Wyithe (2008). “Possibility of Precise Measurement of the Cosmological Power Spectrum with a Dedicated Survey of 21cm Emission after Reionization”. In: *Physical Review Letters* 100.16, 161301, p. 161301. doi: [10.1103/PhysRevLett.100.161301](https://doi.org/10.1103/PhysRevLett.100.161301). arXiv: [0801.1677](https://arxiv.org/abs/0801.1677).
- López, Ericson et al. (2017). “The HI Distribution Observed toward a Halo Region of the Milky Way”. In: *Galaxies* 5.3, p. 45.
- Machin, K. E., M. Ryle, and D. D. Vonberg (1952). “The Design of an Equipment for Measuring Small Radio Frequency Noise Powers”. In: *roc. IEEE* 99.
- Madau, P., A. Meiksin, and M. J. Rees (1997). “21 Centimeter Tomography of the Intergalactic Medium at High Redshift”. In: *Astrophysical Journal* 475, pp. 429–444. eprint: [astro-ph/9608010](https://arxiv.org/abs/astro-ph/9608010).
- Masui, K. W. et al. (2013). “Measurement of 21 cm Brightness Fluctuations at $z \sim 0.8$ in Cross-correlation”. In: *ApJL* 763, L20, p. L20. doi: [10.1088/2041-8205/763/1/L20](https://doi.org/10.1088/2041-8205/763/1/L20). arXiv: [1208.0331 \[astro-ph.CO\]](https://arxiv.org/abs/1208.0331).
- Miller, F. D. (1998). *Basics of Radio Astronomy for the Goldstone-Apple Valley Radio Telescope*. Pasadena, California: California Institute of Technology.
- Mitchell, D. A. and J. G. Robertson (2005). “Reference antenna techniques for canceling radio frequency interference due to moving sources”. In: *Radio Science* 40, RS5S11, RS5S11. doi: [10.1029/2004RS003152](https://doi.org/10.1029/2004RS003152). arXiv: [1003.5997 \[astro-ph.IM\]](https://arxiv.org/abs/1003.5997).

- Miville-Deschénes, M.-A. et al. (2008). “Separation of anomalous and synchrotron emissions using WMAP polarization data”. In: *aap* 490, pp. 1093–1102. doi: [10.1051/0004-6361:200809484](https://doi.org/10.1051/0004-6361:200809484). arXiv: [0802.3345](https://arxiv.org/abs/0802.3345).
- Mort, B. et al. (2017). “Analysing the impact of far-out sidelobes on the imaging performance of the SKA-LOW telescope”. In: *MNRAS* 465, pp. 3680–3692. doi: [10.1093/mnras/stw2814](https://doi.org/10.1093/mnras/stw2814). arXiv: [1602.01805 \[astro-ph.IM\]](https://arxiv.org/abs/1602.01805).
- Mort, Benjamin J et al. (2010). “OSKAR: Simulating digital beamforming for the SKA aperture array”. In: *Phased Array Systems and Technology (ARRAY), 2010 IEEE International Symposium on*. IEEE, pp. 690–694.
- Mukundan, R., S. H. Ong, and P. A. Lee (2001). “Image analysis by Tchebichef moments”. In: *IEEE Transactions on Image Processing* 10, pp. 1357–1364. doi: [10.1109/83.941859](https://doi.org/10.1109/83.941859).
- Murphy, Eric J. (2011). “Identifying Variations to the IMF at High- z Through Deep Radio Surveys”. In: *ASP Conf. Ser.* 440, p. 361. arXiv: [1009.1666 \[astro-ph.CO\]](https://arxiv.org/abs/1009.1666).
- Nan, R. et al. (2011). “The Five-Hundred Aperture Spherical Radio Telescope (fast) Project”. In: *International Journal of Modern Physics D* 20, pp. 989–1024. doi: [10.1142/S0218271811019335](https://doi.org/10.1142/S0218271811019335). arXiv: [1105.3794 \[astro-ph.IM\]](https://arxiv.org/abs/1105.3794).
- Navarro, M. V. (2014). “Diffuse Radio Foregrounds: All-Sky Polarisation and Anomalous Microwave Emission”. MA thesis. University of Manchester.
- Newburgh, L. B. et al. (2014). “Calibrating CHIME: a new radio interferometer to probe dark energy”. In: *Ground-based and Airborne Telescopes V*. Vol. 9145. procspie, p. 91454V. doi: [10.1117/12.2056962](https://doi.org/10.1117/12.2056962). arXiv: [1406.2267 \[astro-ph.IM\]](https://arxiv.org/abs/1406.2267).
- Noll, R. J. (1976). “Zernike polynomials and atmospheric turbulence”. In: *Journal of the Optical Society of America (1917-1983)* 66, pp. 207–211.
- Padmanabhan, Hamsa (2017). “Constraining the CO intensity mapping power spectrum at intermediate redshifts”. In: *arXiv preprint arXiv:1706.01471*.
- Padmanabhan, Nikhil et al. (2007). “The Clustering of Luminous Red Galaxies in the Sloan Digital Sky Survey Imaging Data”. In: *Mon. Not. Roy. Astron. Soc.* 378, pp. 852–872. doi: [10.1111/j.1365-2966.2007.11593.x](https://doi.org/10.1111/j.1365-2966.2007.11593.x). arXiv: [astro-ph/0605302 \[astro-ph\]](https://arxiv.org/abs/astro-ph/0605302).
- Percival, W. J. et al. (2010). “Baryon acoustic oscillations in the Sloan Digital Sky Survey Data Release 7 galaxy sample”. In: *MNRAS* 401, pp. 2148–2168. doi: [10.1111/j.1365-2966.2009.15812.x](https://doi.org/10.1111/j.1365-2966.2009.15812.x). arXiv: [0907.1660 \[astro-ph.CO\]](https://arxiv.org/abs/0907.1660).
- Perley R., Sowinski K. and et al. (2015). *Optimizing VLA Antenna Performance*. EVLA Memo XXX.
- Peterson, J. B. et al. (2009). “21-cm Intensity Mapping”. In: *astro2010: The Astronomy and Astrophysics Decadal Survey*. Vol. 2010. ArXiv Astrophysics e-prints, p. 234. arXiv: [0902.3091 \[astro-ph.IM\]](https://arxiv.org/abs/0902.3091).
- Pogany, T. K. and S. Nadarajah (2009). *On the characteristic function of the generalized normal distribution*. Research Report 18. Probability and Statistics Group School of Mathematics, The University of Manchester.
- Rau, U. et al. (2009). “Advances in Calibration and Imaging Techniques in Radio Interferometry”. In: *Proc. IEEE* 97.

- Roy, J., B. Bhattacharyya, and Y. Gupta (2012). “A multi-pixel beamformer using an interferometric array and its application to the localization of newly discovered pulsars”. In: *MNRAS* 427, pp. L90–L94. doi: [10.1111/j.1745-3933.2012.01351.x](https://doi.org/10.1111/j.1745-3933.2012.01351.x). arXiv: [1209.3858 \[astro-ph.IM\]](https://arxiv.org/abs/1209.3858).
- Sadeh, I., L. L. Feng, and O. Lahav (2015). “Gravitational Redshift of Galaxies in Clusters from the Sloan Digital Sky Survey and the Baryon Oscillation Spectroscopic Survey”. In: *Physical Review Letters* 114.7, 071103, p. 071103. doi: [10.1103/PhysRevLett.114.071103](https://doi.org/10.1103/PhysRevLett.114.071103). arXiv: [1410.5262](https://arxiv.org/abs/1410.5262).
- Saha, R., P. Jain, and T. Souradeep (2006). “A Blind Estimation of the Angular Power Spectrum of CMB Anisotropy from WMAP”. In: *ApJL* 645, pp. L89–L92. doi: [10.1086/506321](https://doi.org/10.1086/506321). eprint: [astro-ph/0508383](https://arxiv.org/abs/astro-ph/0508383).
- Santiago, B. X. et al. (1995). “The Optical Redshift Survey: Sample Selection and the Galaxy Distribution”. In: *ApJ* 446, p. 457. doi: [10.1086/175805](https://doi.org/10.1086/175805). eprint: [astro-ph/9406049](https://arxiv.org/abs/astro-ph/9406049).
- (1996). “The Optical Redshift Survey. II. Derivation of the Luminosity and Diameter Functions and of the Density Field”. In: *ApJ* 461, p. 38. doi: [10.1086/177036](https://doi.org/10.1086/177036). eprint: [astro-ph/9511005](https://arxiv.org/abs/astro-ph/9511005).
- Santos, M. G. et al. (2015). “Cosmology with a SKA HI intensity mapping survey”. In: *ArXiv e-prints*. arXiv: [1501.03989](https://arxiv.org/abs/1501.03989).
- Schramm, D. N. and P. Galeotti (1997). *Generation of Cosmological Large-Scale Structure*. Netherlands: Kluwer Academic.
- Shaw, J. R. et al. (2015). “Coaxing cosmic 21 cm fluctuations from the polarized sky using m-mode analysis”. In: *prd* 91.8, 083514, p. 083514. doi: [10.1103/PhysRevD.91.083514](https://doi.org/10.1103/PhysRevD.91.083514). arXiv: [1401.2095](https://arxiv.org/abs/1401.2095).
- Shu, H. et al. (2010). “Fast Computation of Tchebichef Moments for Binary and Grayscale Images”. In: *IEEE Transactions on Image Processing* 19, pp. 3171–3180. doi: [10.1109/TIP.2010.2052276](https://doi.org/10.1109/TIP.2010.2052276).
- Shurcliff, W. (1962). *Polarized Light*. Cambridge, MA: Harvard University Press.
- Silva, M. et al. (2015). “Prospects for Detecting C II Emission during the Epoch of Reionization”. In: *ApJ* 806, 209, p. 209. doi: [10.1088/0004-637X/806/2/209](https://doi.org/10.1088/0004-637X/806/2/209). arXiv: [1410.4808](https://arxiv.org/abs/1410.4808).
- Sinclair, D. et al. (2014). “Effect of gain and phase errors on SKA1-low imaging quality from 50-600 MHz”. In: *ArXiv e-prints*. arXiv: [1408.3998 \[astro-ph.IM\]](https://arxiv.org/abs/1408.3998).
- Smirnov, O. M. (2011). “Revisiting the radio interferometer measurement equation. I. A full-sky Jones formalism”. In: *A&A* 527, A106, A106. doi: [10.1051/0004-6361/201016082](https://doi.org/10.1051/0004-6361/201016082). arXiv: [1101.1764 \[astro-ph.IM\]](https://arxiv.org/abs/1101.1764).
- Smoot, G. F. and I. Debono (2017). “21 cm intensity mapping with the Five hundred metre Aperture Spherical Telescope”. In: *A&A* 597, A136, A136. doi: [10.1051/0004-6361/201526794](https://doi.org/10.1051/0004-6361/201526794). arXiv: [1407.3583](https://arxiv.org/abs/1407.3583).
- Souradeep, T., R. Saha, and P. Jain (2006). “Angular power spectrum of CMB anisotropy from WMAP”. In: 50, pp. 854–860. doi: [10.1016/j.newar.2006.09.009](https://doi.org/10.1016/j.newar.2006.09.009). eprint: [astro-ph/0608199](https://arxiv.org/abs/astro-ph/0608199).

- Stark, D. P. et al. (2017). “Ly α and C III] emission in z = 7-9 Galaxies: accelerated reionization around luminous star-forming systems?” In: *MNRAS* 464, pp. 469–479. doi: [10.1093/mnras/stw2233](https://doi.org/10.1093/mnras/stw2233). arXiv: [1606.01304](https://arxiv.org/abs/1606.01304).
- Tapken, Christian et al. (2007). “Lyman-alpha emission in high-redshift galaxies”. In: *Astron. Astrophys.* [Astron. Astrophys. 467, 63(2007)]. doi: [10.1051/0004-6361:20065825](https://doi.org/10.1051/0004-6361:20065825). arXiv: [astro-ph/0702414 \[ASTRO-PH\]](https://arxiv.org/abs/astro-ph/0702414).
- Teague, M. R. (1980). “Image analysis via the general theory of moments”. In: *Journal of the Optical Society of America (1917-1983)* 70, pp. 920–930.
- Tegmark, Max et al. (2002). “The Angular power spectrum of galaxies from Early SDSS Data”. In: *Astrophys. J.* 571, pp. 191–205. doi: [10.1086/339894](https://doi.org/10.1086/339894). arXiv: [astro-ph/0107418 \[astro-ph\]](https://arxiv.org/abs/astro-ph/0107418).
- The Polarbear Collaboration: P. A. R. Ade et al. (2014). “A Measurement of the Cosmic Microwave Background B-mode Polarization Power Spectrum at Sub-degree Scales with POLARBEAR”. In: *apj* 794, 171, p. 171. doi: [10.1088/0004-637X/794/2/171](https://doi.org/10.1088/0004-637X/794/2/171). arXiv: [1403.2369](https://arxiv.org/abs/1403.2369).
- Thomas, Shaun A., Filipe B. Abdalla, and Ofer Lahav (2011). “The Angular Power Spectra of Photometric SDSS LRGs”. In: *Mon. Not. Roy. Astron. Soc.* 412, p. 1669. doi: [10.1111/j.1365-2966.2010.18004.x](https://doi.org/10.1111/j.1365-2966.2010.18004.x). arXiv: [1011.2448 \[astro-ph.CO\]](https://arxiv.org/abs/1011.2448).
- Thompson, A. R. and R. N Bracewell (1974). “Interpolation and Fourier Transformation of Fringe Visibilities”. In: *Astro. J.* 79.
- Thompson, A. R., J.M Moran, and G.W Swenson (2001). *Interferometry and Synthesis in Radio Astronomy, 2nd edition*. John Wiley & Sons Inc.
- Thuong, Le-Tien et al. (2015). “Zernike Moment-Based Approach for Detecting Duplicated Image Regions by a Modified Method to Reduce Geometrical and Numerical Errors”. In: *Computational Science and Its Applications - ICCSA 2015 - 15th International Conference, Banff, AB, Canada, June 22-25, 2015, Proceedings, Part IV*, pp. 458–475. doi: [10.1007/978-3-319-21410-8_36](https://doi.org/10.1007/978-3-319-21410-8_36). URL: https://doi.org/10.1007/978-3-319-21410-8_36.
- Tucci, M. et al. (2002). “Polarization Angular Spectra of Galactic Synchrotron Emission on Arcminute Scales”. In: *apj* 579, pp. 607–615. doi: [10.1086/342793](https://doi.org/10.1086/342793). eprint: [astro-ph/0207237](https://arxiv.org/abs/astro-ph/0207237).
- Vallini, Livia et al. (2017). “CO line emission from galaxies in the Epoch of Reionization”. In: *Monthly Notices of the Royal Astronomical Society* 473.1, pp. 271–285.
- van Haarlem, M. P. et al. (2013). “LOFAR: The LOw-Frequency ARray”. In: *A&A* 556, A2, A2. doi: [10.1051/0004-6361/201220873](https://doi.org/10.1051/0004-6361/201220873). arXiv: [1305.3550 \[astro-ph.IM\]](https://arxiv.org/abs/1305.3550).
- Webb, S. (1999). *Measuring the Universe: The Cosmological Distance Ladder*. Chichester, UK: Springer-Praxis Publishing Ltd.
- White, M. (1998). “Remark on the estimation of angular power spectra in the presence of foregrounds”. In: 57, pp. 5273–5275. doi: [10.1103/PhysRevD.57.5273](https://doi.org/10.1103/PhysRevD.57.5273). eprint: [astro-ph/9802211](https://arxiv.org/abs/astro-ph/9802211).

- Wijnholds, S. et al. (2010). “Calibration challenges for future radio telescopes”. In: *IEEE Signal Processing Magazine* 27, pp. 30–42. doi: [10.1109/MSP.2009.934853](https://doi.org/10.1109/MSP.2009.934853). arXiv: [1004.0156 \[astro-ph.IM\]](https://arxiv.org/abs/1004.0156).
- Wijnholds, S. J. and A.-J. van der Veen (2008). “Fundamental Imaging Limits of Radio Telescope Arrays”. In: *IEEE Journal of Selected Topics in Signal Processing* 2, pp. 613–623. doi: [10.1109/JSTSP.2008.2004216](https://doi.org/10.1109/JSTSP.2008.2004216). arXiv: [1003.2307 \[astro-ph.IM\]](https://arxiv.org/abs/1003.2307).
- Wolz, L. et al. (2014). “The effect of foreground subtraction on cosmological measurements from intensity mapping”. In: 441, pp. 3271–3283. doi: [10.1093/mnras/stu792](https://doi.org/10.1093/mnras/stu792). arXiv: [1310.8144](https://arxiv.org/abs/1310.8144).
- Wolz, L. et al. (2015). “Foreground Subtraction in Intensity Mapping with the SKA”. In: *Advancing Astrophysics with the Square Kilometre Array (AASKA14)*, 35, p. 35. arXiv: [1501.03823](https://arxiv.org/abs/1501.03823).
- Wood, R. W. (1988). *Physical Optics*. Washington, D.C: Optical Society of America.
- Woodburn, L. et al. (2015). “Conversion of a New Zealand 30-Metre Telecommunications Antenna into a Radio Telescope”. In: 32, e017, e017. doi: [10.1017/pasa.2015.13](https://doi.org/10.1017/pasa.2015.13). arXiv: [1407.3346 \[astro-ph.IM\]](https://arxiv.org/abs/1407.3346).
- Wright, Andrew (2004). “Single-dish Radio Astronomy”. In:
- Wu, J. et al. (2017). “MomentsNet: a simple learning-free method for binary image recognition”. In: *ArXiv e-prints*. arXiv: [1702.06767 \[cs.CV\]](https://arxiv.org/abs/1702.06767).
- Wyant, James C and Katherine Creath (1992). “Basic wavefront aberration theory for optical metrology”. In: *Applied optics and optical engineering* 11.part 2, pp. 28–39.
- Yap, P.-T., R. Paramesran, and S.-H. Ong (2003). “Image analysis by krawtchouk moments”. In: *IEEE Transactions on Image Processing* 12, pp. 1367–1377. doi: [10.1109/TIP.2003.818019](https://doi.org/10.1109/TIP.2003.818019).
- Yap, Pew-Thian and Paramesran Raveendran (2005). “An Efficient Method for the Computation of Legendre Moments.” In: *IEEE Trans. Pattern Anal. Mach. Intell.* 27.12, 1996–2002. URL: <http://dblp.uni-trier.de/db/journals/pami/pami27.html#YapP05>.
- Yatawatta, S. (2008). “Subspace Techniques for Radio-Astronomical Data Enhancement”. In: *ArXiv e-prints*. arXiv: [0809.0208](https://arxiv.org/abs/0809.0208).
- Yatawatta, S. et al. (2013). “Initial deep LOFAR observations of epoch of reionization windows. I. The north celestial pole”. In: *A&A* 550, A136, A136. doi: [10.1051/0004-6361/201220874](https://doi.org/10.1051/0004-6361/201220874). arXiv: [1301.1630 \[astro-ph.IM\]](https://arxiv.org/abs/1301.1630).
- Yue, B. et al. (2015). “Intensity mapping of [C II] emission from early galaxies”. In: *MNRAS* 450, pp. 3829–3839. doi: [10.1093/mnras/stv933](https://doi.org/10.1093/mnras/stv933). arXiv: [1504.06530](https://arxiv.org/abs/1504.06530).
- Zhang, C., J. Wu, and W. Sun (2007). “Applications of Pseudo-Polar FFT in Synthetic Aperture Radiometer Imaging”. In: *Progress In Electromagnetics Research Symposium* 3.
- Zhang, D. and G. Lu (2004). “Review of shape representation and description techniques”. In: *Pattern Recognition* 37.
- Zhang, H. et al. (2010). “Blurred Image Recognition by Legendre Moment Invariants”. In: *IEEE Transactions on Image Processing* 19, pp. 596–611. doi: [10.1109/TIP.2009.2036702](https://doi.org/10.1109/TIP.2009.2036702).

- Zitrin, A. et al. (2015). “Lyman α Emission from a Luminous $z = 8.68$ Galaxy: Implications for Galaxies as Tracers of Cosmic Reionization”. In: *ApJL* 810, L12, p. L12. doi: [10.1088/2041-8205/810/1/L12](https://doi.org/10.1088/2041-8205/810/1/L12). arXiv: [1507.02679](https://arxiv.org/abs/1507.02679).

Appendix A

Appendix A

OSKAR BEAMPATTERN AND FOREGROUND SIMULATIONS

A.1 Ray Tracing Technique

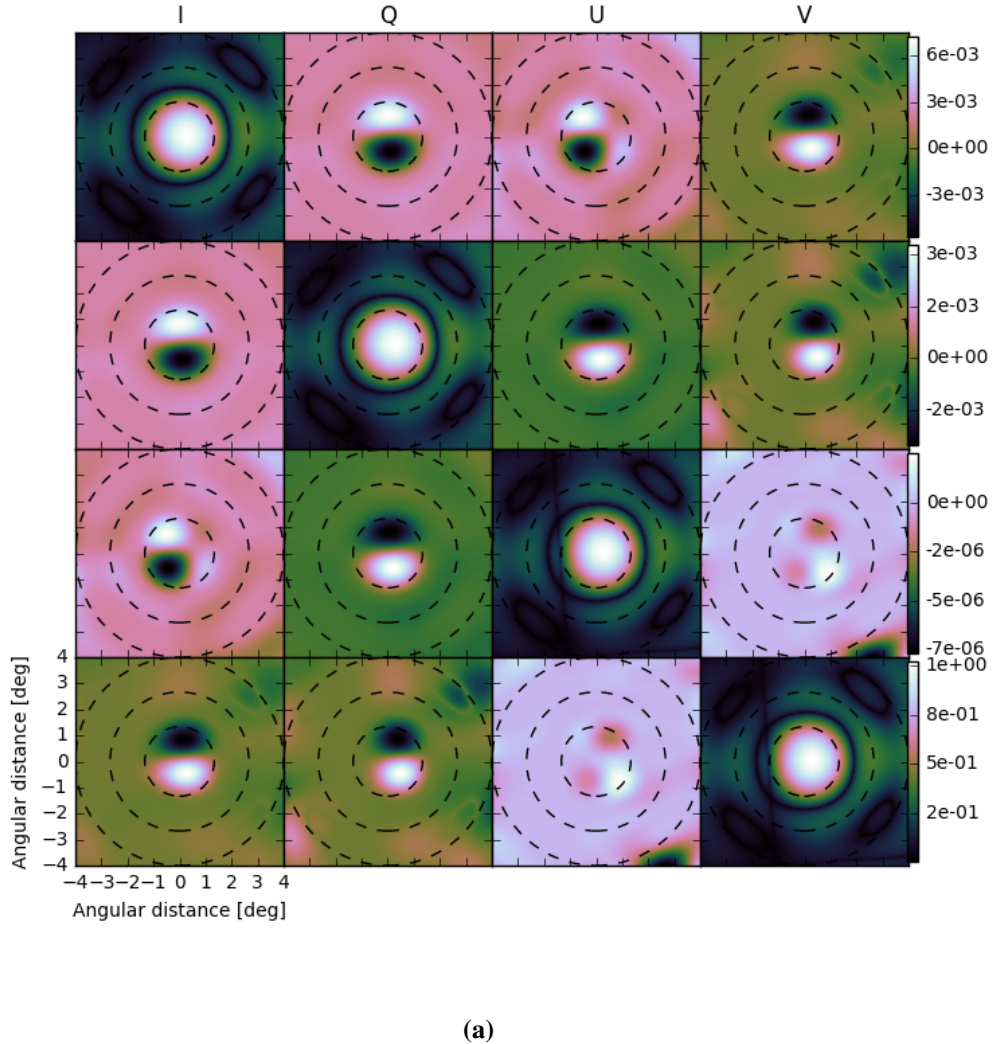
This method of producing antenna response patterns in the geometric optics approximation was developed for the JVLA and Expanded Very Large Array (EVLA¹) of antennas by Brisken 2003 (cassbeam Software for cassegrain antenna modelling, National Radio Astronomy Observatory (NRAO²)). It is used to obtain the electric field on an evenly distributed grid points on the aperture plane through a complicated process. Some iterations are needed, since the ray may not propagate along the line of sight \hat{z} from the primary to the aperture plane. Initially, the (x, y) component of the grid point to be determined is taken as the reference point on the primary. The respective z value and the surface normal are then calculated for that point on the primary. The virtual ray is then reflected off the sub-reflector. Here, the sub-reflector is never stored as a raster surface rather, recalculated each time it is needed and this is by far more efficient than searching a tabulated surface for an intersection point. The sub-reflector displacement and rotation are then considered. A ray is then projected from the feed to this point on the sub-reflector. The procedure is now reversed such that a guess for the appropriate sub-reflector point is made. A ray is traced from the feed to this point on the sub-reflector, then reflects towards the primary and finally reflects to the aperture plane. The (x', y') value of the intersection of the ray with the aperture plane is compared with the initial (x, y) . An offset is applied to the initial value and the iteration continues. About 3 to 7 iterations are good enough for convergence. The final ray is defined once points on both the aperture plane and the primary are known. 3 rays are shot out from a small triangular region of the aperture plane and are used to calculate the flux through the point of interest on the aperture plane. This value includes the taper of the feed, the dilution of the beam due to expansion and the effects of all the surface shapings. The magnitude of the ray is then used to obtain the phase of the field on the aperture such that, the 2 circular polarisation vectors are propagated from the feed. Finally, the electric field decomposed into a linear polarisation basis for each outgoing circular polarisation calculated on the aperture plane grid.

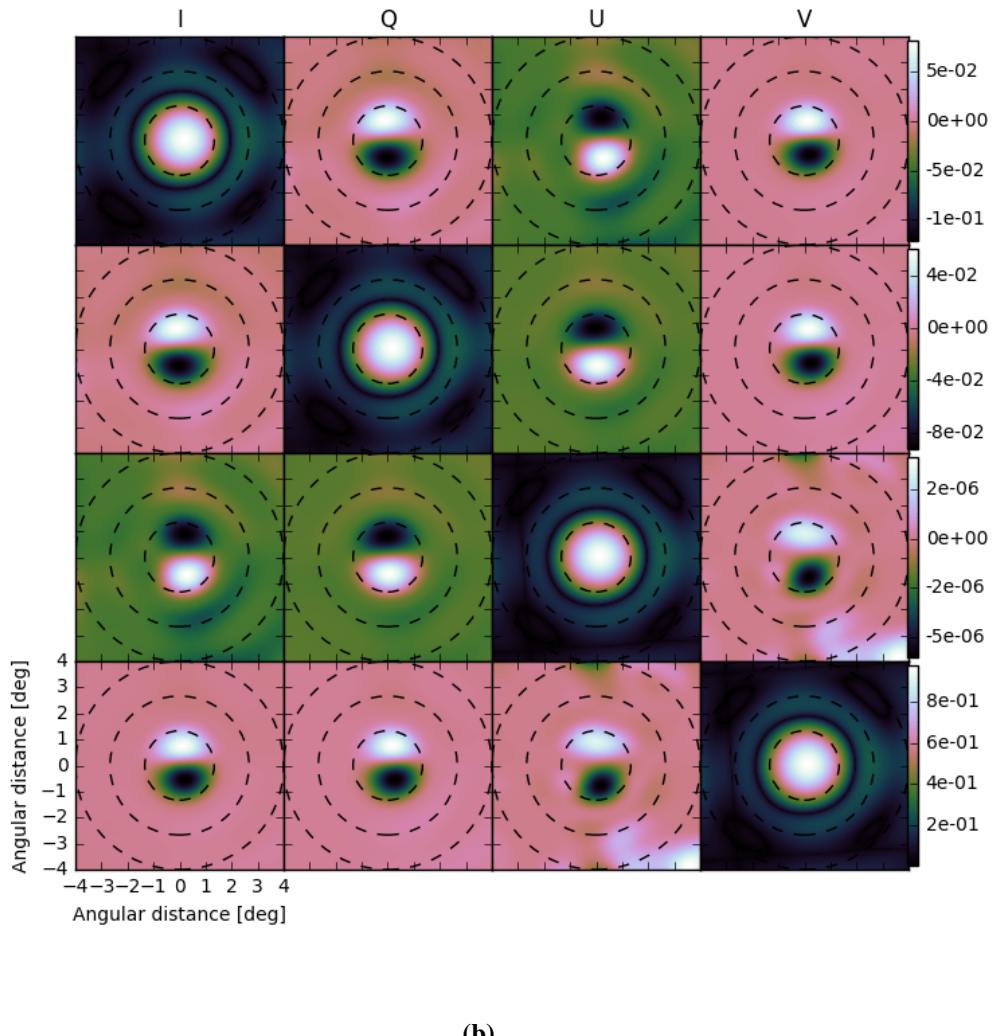
¹<http://www.aoc.nrao.edu/evla/>

²<https://public.nrao.edu/>

A.2 Modelled and measured beams

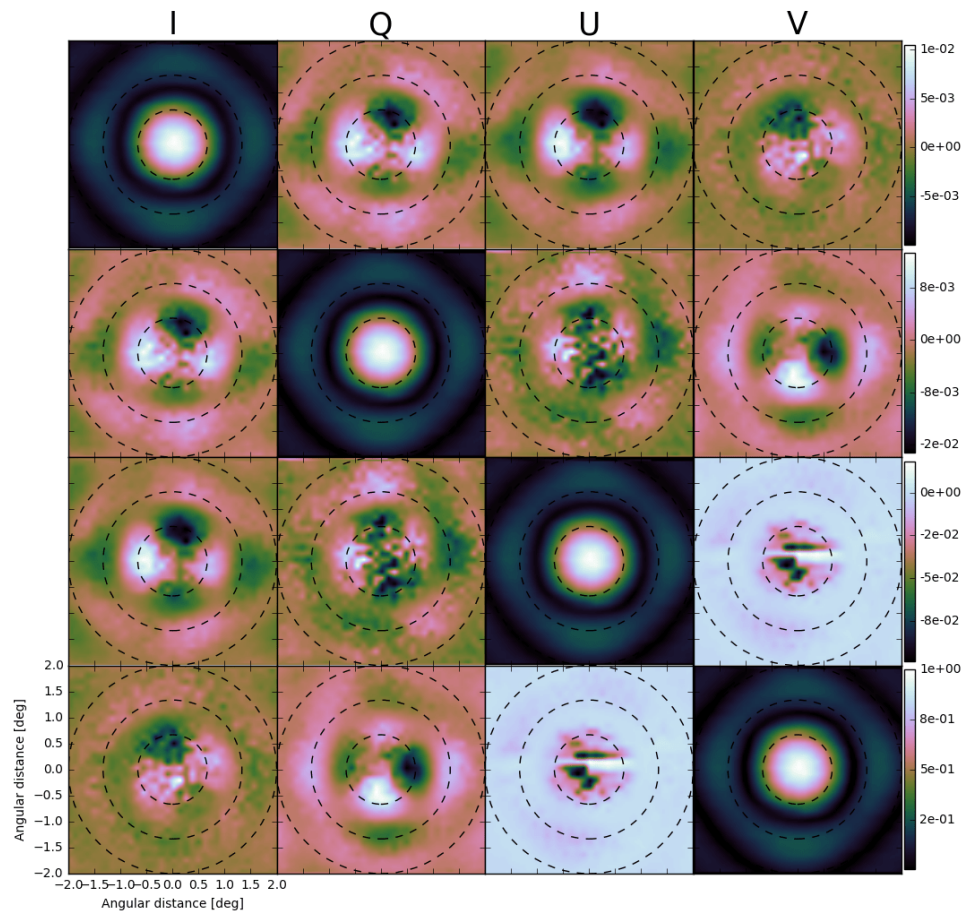
The Mueller matrix representations in Fig. A.1 show the different perturbation methods (i.e. gain, phase and orientation of dipole errors) used to corrupt the OSKAR beam model. These perturbed beams are then compared with the errors produced from “real” measured beams of the JVLA in Fig. A.2.





(b)

Figure A.1: Fully polarised distorted primary beams of KAT-7. (a) Due to gain and phase errors. (b) Due to dipole orientation errors.



(a)

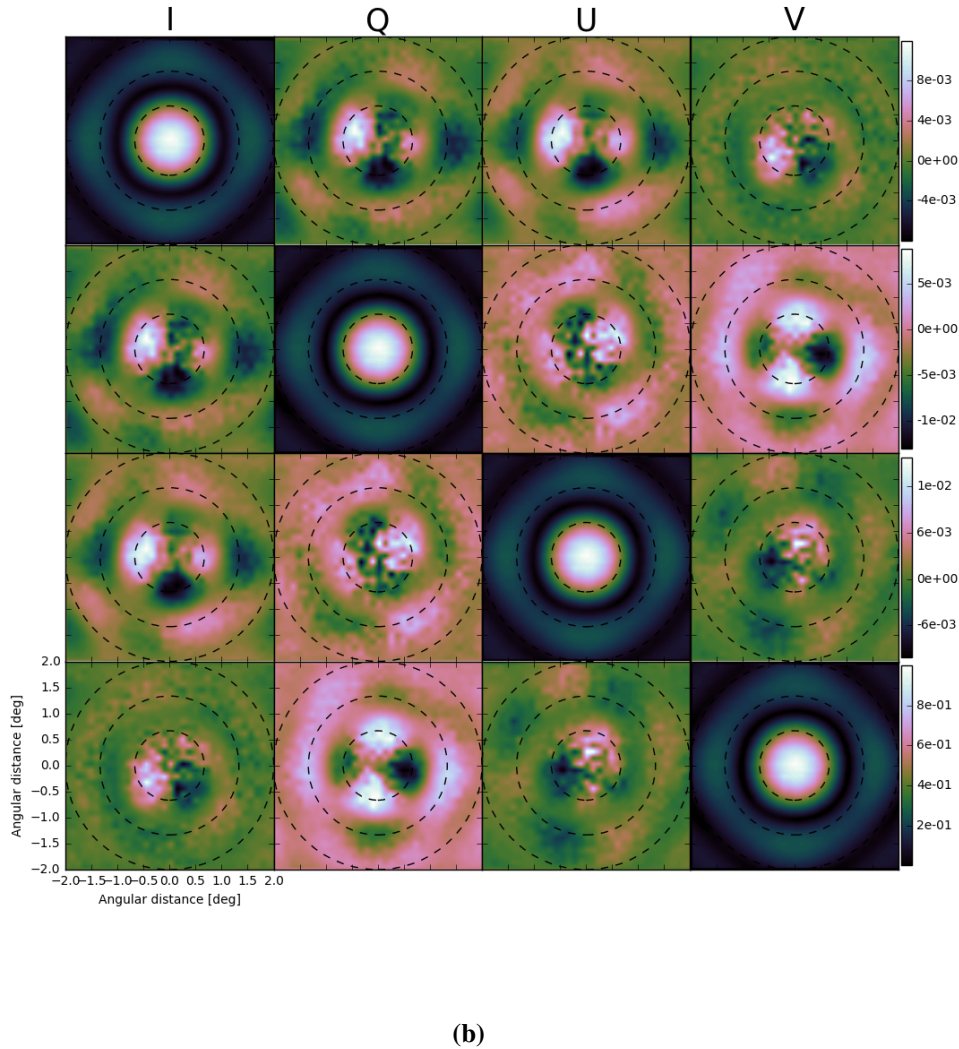


Figure A.2: 1 GHz holography measured Mueller beams of JVLA. (a) Antenna 5. (b) Antenna 6.

A.3 Measured Full-sky maps

Figs. A.3 and A.4 display the complete corrupted convolved maps generated from simulating the foregrounds in Fig. 3.3 with the perturbed model beams (due to gain and phase and dipole orientation errors respectively).

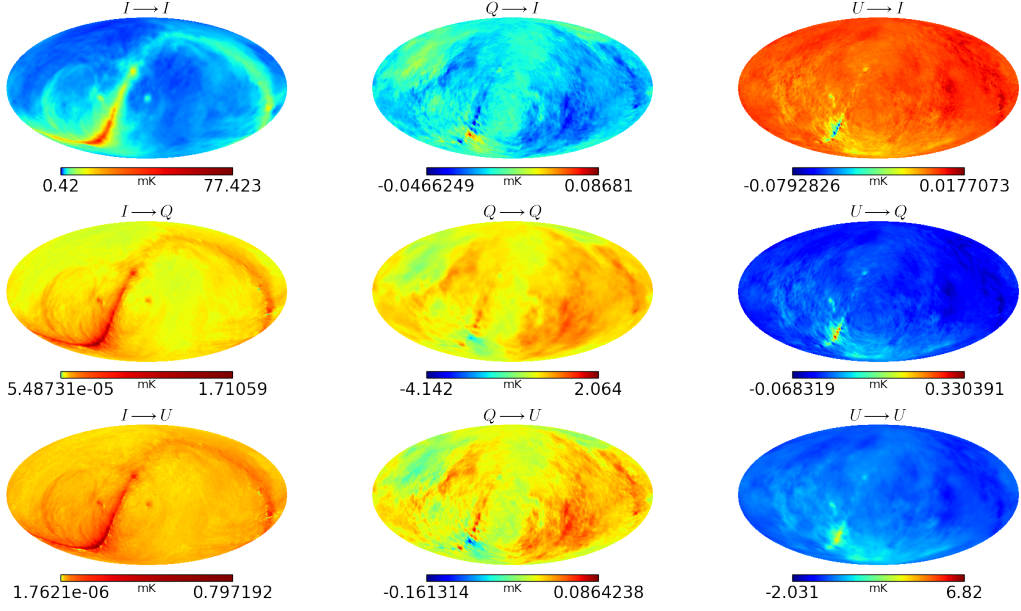


Figure A.3: Convolved full-sky polarisation maps using the corrupted primary beams in Fig. A.1a. Here also, we used the m_{II} beam in Fig. A.1a to convolve Stokes I in Fig. 3.3 and produce the convolved map $I \rightarrow I$, then we used m_{QI} beam to convolve Stokes Q to obtain the convolved map $Q \rightarrow I$, also, using the m_{UI} beam to convolve Stokes U we produce the convolved map $U \rightarrow I$. The same approach is repeated to obtain (in row 2) $I \rightarrow Q, Q \rightarrow Q, Q \rightarrow U$ and (in row 3) $I \rightarrow U, Q \rightarrow U, U \rightarrow U$ by using the corresponding beams m_{IQ}, m_{QQ}, m_{UQ} and m_{IU}, m_{QU}, m_{UU} .

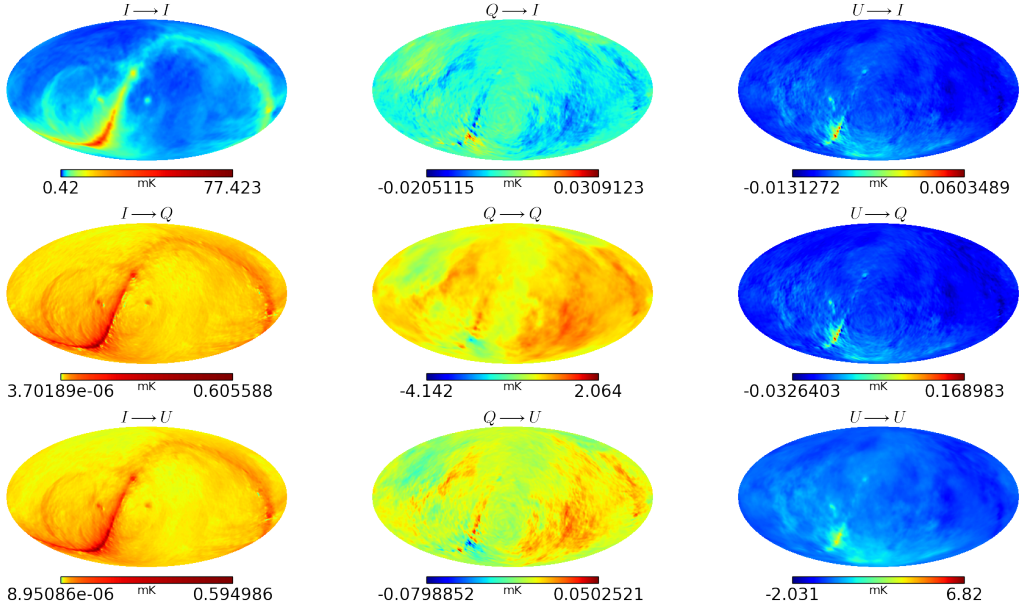


Figure A.4: Convolved full-sky polarisation maps using the corrupted primary beams in Fig. A.1b.

Fig. A.5 represents the full-sky convolved maps simulated with the holography measured beams of JVLA in Fig. A.2.

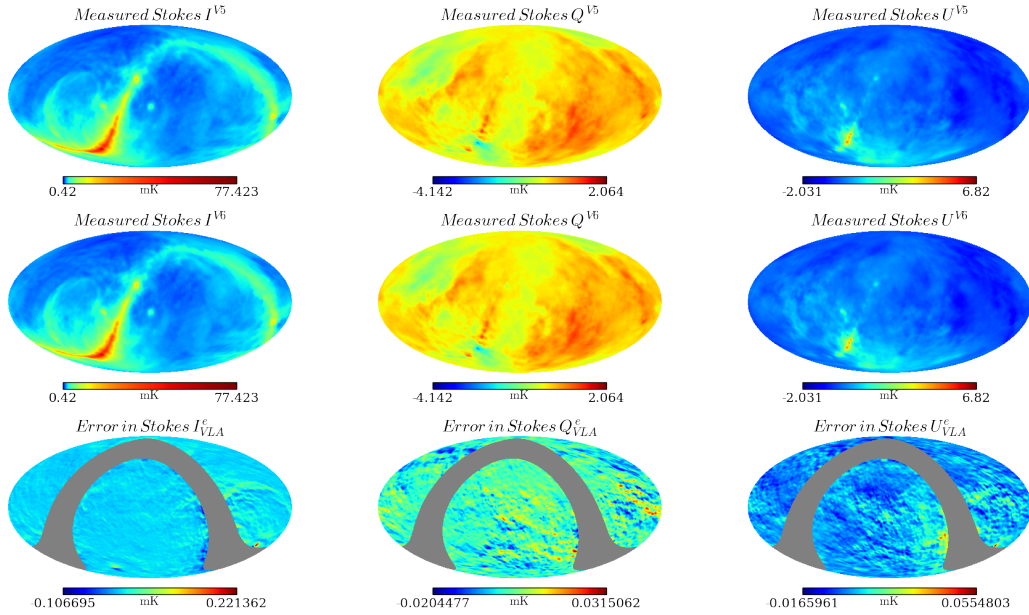


Figure A.5: Measured Stokes I , Q and U for holography measured beams of JVLA with corresponding errors terms.

A.4 Error Estimation in the Power Spectrum

Table A.1 displays the errors recorded in the angular power spectrum estimation when modelled beams are assumed, whilst the foregrounds are actually convolved with real measured beams. These errors are tabulated from the absolute differences of the standard errors reported in Fig. 4.6.

Table A.1: Error introduced in the power spectrum estimation

	1.3							
	I		Q		U		$TOTAL$	
	<i>GP [%]</i>	<i>XY [%]</i>	<i>GP [%]</i>	<i>XY [%]</i>	<i>GP [%]</i>	<i>XY [%]</i>	<i>GP [%]</i>	<i>XY [%]</i>
I	0.0640	0.0640	0.0151	0.0137	0.0050	0.0045	0.0841	0.0822
Q	0.0010	0.0008	0.0221	0.0224	0.0007	0.0055	0.0238	0.0287
U	0.0007	0.0007	0.0194	0.0341	0.0354	0.0362	0.0555	0.0710